

Study of Local Environment and Nuclear Interactions in
Magnesium and Sulfur Containing Materials by
 ^{25}Mg and ^{33}S Solid-State Nuclear Magnetic Resonance
Spectroscopy and First-Principles Calculations

By

Peter J. Pallister

B.Sc. – Chemistry: Nanotechnology, Carleton University, 2008

A thesis submitted to the Faculty of Graduate Studies and Research
in partial fulfillment of the requirements for the degree of

Master of Science

in

Chemistry

Carleton University
Ottawa, Ontario

© 2010, Peter J. Pallister



Library and Archives
Canada

Published Heritage
Branch

395 Wellington Street
Ottawa ON K1A 0N4
Canada

Bibliothèque et
Archives Canada

Direction du
Patrimoine de l'édition

395, rue Wellington
Ottawa ON K1A 0N4
Canada

Your file *Votre référence*
ISBN: 978-0-494-71594-9
Our file *Notre référence*
ISBN: 978-0-494-71594-9

NOTICE:

The author has granted a non-exclusive license allowing Library and Archives Canada to reproduce, publish, archive, preserve, conserve, communicate to the public by telecommunication or on the Internet, loan, distribute and sell theses worldwide, for commercial or non-commercial purposes, in microform, paper, electronic and/or any other formats.

The author retains copyright ownership and moral rights in this thesis. Neither the thesis nor substantial extracts from it may be printed or otherwise reproduced without the author's permission.

AVIS:

L'auteur a accordé une licence non exclusive permettant à la Bibliothèque et Archives Canada de reproduire, publier, archiver, sauvegarder, conserver, transmettre au public par télécommunication ou par l'Internet, prêter, distribuer et vendre des thèses partout dans le monde, à des fins commerciales ou autres, sur support microforme, papier, électronique et/ou autres formats.

L'auteur conserve la propriété du droit d'auteur et des droits moraux qui protègent cette thèse. Ni la thèse ni des extraits substantiels de celle-ci ne doivent être imprimés ou autrement reproduits sans son autorisation.

In compliance with the Canadian Privacy Act some supporting forms may have been removed from this thesis.

While these forms may be included in the document page count, their removal does not represent any loss of content from the thesis.

Conformément à la loi canadienne sur la protection de la vie privée, quelques formulaires secondaires ont été enlevés de cette thèse.

Bien que ces formulaires aient inclus dans la pagination, il n'y aura aucun contenu manquant.


Canada

Abstract

Given their inherent low detection sensitivity, ^{25}Mg and ^{33}S remain relatively understudied nuclei in solid-state nuclear magnetic resonance spectroscopy. With the use of an ultrahigh magnetic field of 21.1 T, magic-angle spinning, and the combination of various signal-enhancing techniques, the study of ^{25}Mg and ^{33}S SS-NMR has been made increasingly feasible. In this work, a series of magnesium-containing compounds with known crystal structure has been studied at natural abundance with the use of ^{25}Mg SS-NMR. As well, a number of model anhydrous sulfate materials have been studied at natural abundance via ^{33}S SS-NMR. First principles calculations implementing plane wave basis sets and pseudopotentials have been carried out on all compounds studied. Correlations between calculated NMR parameters and experimental results have given insight into the structural parameters. This work demonstrates that the chemical shift range of Mg in diamagnetic compounds may approach 200 ppm, although most commonly observed shifts are within the range of -15 to 25 ppm. The quadrupolar effects are shown to dominate ^{25}Mg spectra in non-cubic environments and chemical shift anisotropy could only be detected in a handful of cases. For ^{33}S in anhydrous sulfates, however, both the quadrupolar and shielding anisotropy interactions are shown to have an effect. With the use of calculation and experimental results, structural assessments were performed on existing anhydrous sulfate structures.

Acknowledgments

First and foremost I would like to thank my supervisor, Dr. John Ripmeester, for giving me the opportunity to continue my scientific pursuit by way of an M.Sc. in the Materials Structure and Function Group at NRC's Steacie Institute. The chance to work in such an interesting and powerful field has been quite rewarding.

I also need to thank everyone working at M-40 during my time there for their tremendous assistance in virtually everything. From oscilloscopes to rocket cars; exploding samples and pulse programming to making life decisions, Luke, Jamie, Eric and Andreas, thank you very much for the great work environment.

I certainly would not have been able to perform my experiments if I did not have access to the world-class National Ultrahigh Field NMR Facility for Solids here at M-40. The work done here and Victor's devotion to the facility and its users has produced some groundbreaking developments in the area of SS-NMR and has put Canada on the map as one of the leaders in NMR spectroscopy. Thank you Victor for your dedication and invaluable advice.

Of course, I need to especially thank Dr. Igor Moudrakovski, my boss and mentor over the past 2 years. Igor's unbelievable patience, vast knowledge and neverending guidance has educated me not only in the area of NMR, but has also furthered my understanding of what it really means to be a scientist. I would not be the scientist I am today without your help, thank you.

Lastly, I should mention that I would not even exist if it weren't for my parents. Their constant love and support has allowed me to pursue my love for science. And Julie, if it weren't for your love I would not be able to tie my shoes in the morning, let alone finish a Masters degree in Chemistry.

Table of Contents

Abstract	i
Acknowledgments	ii
List of Figures	v
List of Tables	viii
List of Symbols and Abbreviations	ix
List of Appendix Data	x
1. Introduction	1
1.1 Chemical Systems Under Review	1
<i>1.1.1 Mg-containing Materials</i>	2
<i>1.1.2 S-containing Materials</i>	6
1.2 Solid-State NMR	9
<i>1.2.1 General Considerations</i>	9
<i>1.2.2 Nuclear Shielding</i>	15
<i>1.2.3 Quadrupolar Interaction</i>	19
<i>1.2.4 Experimental Techniques</i>	28
1.3 Quantum Mechanical Computation of Spectral Parameters	34
2. Experimental Details	38
2.1 Materials	38
2.2 Solid-State NMR Spectroscopy	40
2.3 Spectral Simulations	42
2.4 Quantum Chemical Calculations	42

3. ^{25}Mg in Mg-Containing Materials	44
3.1 Structural Details of Systems Studied.....	44
3.2 Determination of ^{25}Mg NMR Parameters.....	46
3.3 Structural Correlation of the Shielding Interaction	51
3.4 Structural Correlation of the Quadrupolar Interaction	53
3.5 Mg in O-coordinating Environments.....	56
3.6 Mg in Non-O-coordinating Environments.....	71
4. ^{33}S in Anhydrous Sulfates.....	80
4.1 Structural Details of Systems Studied.....	80
4.2 Determination of ^{33}S NMR Parameters	83
4.3 Structural Correlation of the Shielding Interaction	89
4.4 Structural Correlation of the Quadrupolar Interaction	102
4.5 Structural Assessment via Solid State NMR and	
First Principles Calculations.....	107
5. Conclusions and Future Work.....	113
6. References.....	116
7. Appendix.....	129
Appendix A - Additional ^{25}Mg SS-NMR Spectra.....	129
Appendix B - Structural Details of All Compounds (.cif files)	135

List of Figures

<i>Figure 1</i> – Nuclear Zeeman splitting for the ^1H , ^{14}N , and ^{27}Al nuclear ground states.	9
<i>Figure 2</i> – Experimental CSA interaction-dominated SS-NMR powder pattern for ^{29}Si in Co-doped forsterite (Mg_2SiO_4).	18
<i>Figure 3</i> – Schematic of the charge distribution in a nucleus. The quadrupole moment is non-zero for nuclei with ground state spin $> 1/2$	20
<i>Figure 4</i> – A model linear molecule AB_2 , shown on left, would generate an electric field gradient like that seen on the right	20
<i>Figure 5</i> – Energy splitting diagram for a typical $I = 5/2$ nucleus showing the degree to which the quadrupolar interaction affects the energy of each transition	24
<i>Figure 6</i> – Typical central transition powder patterns for a quadrupolar interaction for different values of η_Q . The static lineshape is shown on the left, where the right shows a typical MAS central transition lineshape dominated by the 2 nd order quadrupolar interaction. Note also that conventionally the frequency axis is reported as decreasing to right, opposite of what is shown here	26
<i>Figure 7</i> – Effect of the quadrupolar coupling constant, C_Q , on the central transition MAS powder pattern for a typical quadrupolar interaction-dominated system	27
<i>Figure 8</i> – Visible singularities of the central transition of a quadrupolar interaction dominated system under MAS ($C_Q = 2$ MHz, $\eta_Q = 0.3$, $I = 3/2$).	27
<i>Figure 9</i> – Solid-State ^{13}C NMR spectra (at $B_0 = 11.7\text{T}$) of a labeled glycine powder sample. MAS spinning speed is shown in each spectrum and e) shows the static CSA powder pattern. As spinning speed is increased the anisotropy is averaged to only the isotropic peak (a)).	30
<i>Figure 10</i> – Schematic diagrams of the various signal-enhancing techniques useful for observing the central transition of half-integer spin quadrupolar nuclei. a) shows the QCPMG technique, where before the π pulse train is a typical quadrupolar or Hahn echo. b) shows the amplitude modulated DFS pulse, c) shows the short phase-inverted pulse train of RAPT, and d) shows the HS or sechinv pulse. b), c) and d) pulses can be placed in front of the first $\pi/2$ of a) to give signal enhancement. e) shows the WURST-QCPMG pulse sequence used for ultra-wideline spectra.	33

<i>Figure 11</i> – Correlation between ^{25}Mg experimentally determined chemical shift and calculated absolute shielding as determined by CASTEP for all 28 Mg compounds studied. Line of best fit is shown. The inset shows enlarged portion of correlation where most compounds are found.	52
<i>Figure 12</i> - Correlation between ^{25}Mg experimentally determined quadrupolar coupling constant, C_Q , and the calculated quadrupolar coupling constant, C_Q^{calc} , as determined by CASTEP for all 29 Mg compounds studied. Line of best fit is shown as the solid line. The dashed line shows a perfect 1:1 correlation.	56
<i>Figure 13</i> – ^{25}Mg SS-NMR spectra of brucite ($\text{Mg}(\text{OH})_2$).....	59
<i>Figure 14</i> – ^{25}Mg SS-NMR spectra $\text{MgSO}_4 \cdot 6\text{H}_2\text{O}$, $\text{Mg}(\text{NH}_4)_2(\text{SO}_4)_2 \cdot 6\text{H}_2\text{O}$ and $\text{MgSO}_4 \cdot 7\text{H}_2\text{O}$	61
<i>Figure 15</i> – ^{25}Mg SS-NMR spectra of $\text{Mg}_3(\text{PO}_4)_2 \cdot 8\text{H}_2\text{O}$ and $\text{MgHPO}_4 \cdot 3\text{H}_2\text{O}$	63
<i>Figure 16</i> – ^{25}Mg SS-NMR spectra of MgMoO_4 and $\beta\text{-MgSO}_4$	66
<i>Figure 17</i> – ^{25}Mg SS-NMR spectra of natural magnesite (MgCO_3)	66
<i>Figure 18</i> – ^{25}Mg SS-NMR spectra Spinel (MgAl_2O_4) and Geikielite (MgTiO_3).....	67
<i>Figure 19</i> – ^{25}Mg SS-NMR spectra of natural forsterite (Mg_2SiO_4)	68
<i>Figure 20</i> – ^{25}Mg SS-NMR spectra of $\text{Mg}(\text{AcAc})_2 \cdot 2\text{H}_2\text{O}$, $\text{Mg}(\text{OAc})_2 \cdot 4\text{H}_2\text{O}$ and $\text{Mg}(\text{HCOO})_2 \cdot 2\text{H}_2\text{O}$	71
<i>Figure 21</i> – ^{25}Mg SS-NMR spectra of MgH_2 and MgCl_2	73
<i>Figure 22</i> – ^{25}Mg SS-NMR spectra of Mg_3N_2	78
<i>Figure 23</i> – ^{25}Mg SS-NMR spectrum of Mg-phthalocyanine	79
<i>Figure 24</i> – ^{33}S SS-NMR spectra of SrSO_4	85
<i>Figure 25</i> – ^{33}S SS-NMR spectra of ZnSO_4	88
<i>Figure 26</i> – ^{33}S SS-NMR spectra of Na_2SO_4 and K_2SO_4	90
<i>Figure 27</i> – ^{33}S SS-NMR spectra of Rb_2SO_4 and Cs_2SO_4	91
<i>Figure 28</i> – ^{33}S SS-NMR spectra of $\text{Al}_2(\text{SO}_4)_3$	93
<i>Figure 29</i> – ^{33}S SS-NMR spectra of $\text{Ga}_2(\text{SO}_4)_3$	94
<i>Figure 30</i> – ^{33}S SS-NMR spectra of $\text{In}_2(\text{SO}_4)_3$	95
<i>Figure 31</i> – ^{33}S SS-NMR spectra of $\alpha\text{-MgSO}_4$	97
<i>Figure 32</i> – ^{33}S SS-NMR spectra of $\beta\text{-MgSO}_4$	97
<i>Figure 33</i> – ^{33}S SS-NMR spectra of Li_2SO_4	98

<i>Figure 34</i> – ^{33}S SS-NMR spectra of $(\text{NH}_4)_2\text{SO}_4$	99
<i>Figure 35</i> - Correlation between ^{33}S experimentally determined chemical shift and calculated absolute shielding as determined by CASTEP for all sulfates compounds studied. Line of best fit is shown merely to reflect the excellent agreement and almost 1:1 correlation. See Figure 36 for full shielding-shift correlation. The red points represent calculations for structures that produced the largest disagreement with experiment. (see Table 7).....	101
<i>Figure 36</i> – Full shielding correlation between ^{33}S experimentally determined chemical shift and calculated absolute shielding as determined by CASTEP for all sulfate and sulfide compounds. Line of best fit is shown.	102
<i>Figure 37</i> – ^{33}S SS-NMR spectra of CaSO_4	104
<i>Figure 38</i> – ^{33}S SS-NMR spectra of BaSO_4	105
<i>Figure 39</i> - Correlation between ^{33}S experimentally determined quadrupolar coupling constant, C_Q , and the calculated quadrupolar coupling constant, C_Q^{calc} , as determined by CASTEP for all sulfate compounds studied. Line of best fit is shown.....	107

List of Tables

<i>Table 1</i> – Mg-containing compounds studied in this work.....	5
<i>Table 2</i> – Reported crystal structures for sulfates studied in this work.	8
<i>Table 3</i> – Structural details of magnesium compounds studied.	45
<i>Table 4</i> – Experimental and calculated ^{25}Mg NMR parameters for all compounds studied.....	49
<i>Table 5</i> – Experimental and calculated ^{25}Mg CSA parameters for Mg compounds studied with an observable interaction.	53
<i>Table 6</i> – Structural details of sulfate compounds studied.	81
<i>Table 7</i> – Experimental and calculated ^{33}S NMR parameters for all compounds studied.....	86
<i>Table 8</i> – Experimental and calculated ^{33}S NMR parameters for sulfides used in shielding correlation (Figure 36). ^{33, 35}	100

List of Symbols and Abbreviations

CPMG – Carr Purcell Meiboom Gill

CSA – Chemical Shielding Anisotropy

DFS – Double Frequency Sweep

DFT – Density Functional Theory

EFG – Electric Field Gradient

HS – Hyperbolic Secant

MAS – Magic Angle Spinning

NMR – Nuclear Magnetic Resonance

PAS – Principal Axis System

PXRD – Powder X-ray Diffraction

QCPMG – Quadrupolar Carr Purcell Meiboom Gill

RAPT – Rotor Assisted Population Transfer

r.f. – Radio Frequency

SCXRD – Single-Crystal X-ray Diffraction

SS-NMR – Solid State Nuclear Magnetic Resonance

WURST – Wideline Uniform-Rate Smooth Truncation

List of Appendix Data

<i>Figure A1</i> – Static Bloch Decay ^{25}Mg NMR spectrum of MgO	129
<i>Figure A2</i> – 5kHz MAS Bloch Decay ^{25}Mg NMR spectrum of $\text{MgCl}_2 \cdot 6\text{H}_2\text{O}$	129
<i>Figure A3</i> – a) 5kHz MAS Bloch Decay ^{25}Mg NMR spectra (experimental and simulated) of $\text{Mg}(\text{NO}_3)_2 \cdot 6\text{H}_2\text{O}$. b) Static Hahn Echo ^{25}Mg NMR spectra (experimental and simulated) of $\text{Mg}(\text{NO}_3)_2 \cdot 6\text{H}_2\text{O}$	130
<i>Figure A4</i> – 5kHz MAS Bloch Decay ^{25}Mg NMR spectra (experimental and simulated) of MgWO_4	130
<i>Figure A5</i> – ^{25}Mg SS-NMR spectra of $\text{Mg}(\text{VO}_3)_2$. a) Simulation of the single crystallographically unique site in $\text{Mg}(\text{VO}_3)_2$. b) Static full Hahn Echo. c) Static QCPMG. d) Static full Hahn Echo obtained in 3 pieces with varying central excitation frequencies (O1) to observe edge singularities.	131
<i>Figure A6</i> – 5kHz MAS Bloch Decay ^{25}Mg NMR spectra (experimental and simulated) of $\alpha\text{-Mg}_2\text{V}_2\text{O}_7$	131
<i>Figure A7</i> – $\text{Mg}_3(\text{VO}_4)_2$. a) 18kHz MAS QCPMG ^{25}Mg spectra (experimental and simulated) of $\text{Mg}_3(\text{VO}_4)_2$ zoomed in on the low intensity site with the larger C_Q . b) 10kHz MAS Bloch decay ^{25}Mg spectra (experimental and simulated) of $\text{Mg}_3(\text{VO}_4)_2$ showing the site with the smaller C_Q . The second site is too broad and weak to be seen at 10kHz MAS Bloch Decay. * MgO ; † MgO spinning sideband.....	132
<i>Figure A8</i> – $\alpha\text{-MgSO}_4$. a) 16kHz MAS QCPMG, Hahn echo and simulated ^{25}Mg NMR spectra of $\alpha\text{-MgSO}_4$. b) Static QCPMG, Hahn echo and simulated ^{25}Mg NMR spectra of $\alpha\text{-MgSO}_4$	133
<i>Figure A9</i> – 5kHz MAS Bloch Decay ^{25}Mg NMR spectrum of MgS . * MgO	133
<i>Figure A10</i> – Static Bloch Decay ^{25}Mg NMR spectrum of Mg_2Si	134

1. Introduction

As new and interesting materials are being developed, the importance of accurate physico-chemical characterization is in increasing demand. The development of novel solid-state materials is of particular interest and the study of the fundamental properties of these materials is crucial to the understanding and potential improvement of these materials. Before studying complex systems with numerous magnetic or electronic interactions, it is often beneficial to study the contributing interactions separately using well characterized or model systems. In this work a powerful and fast-growing spectroscopic technique of solid-state nuclear magnetic resonance (SS-NMR) spectroscopy was used to probe the local environment and nuclear interactions in some model chemical systems to determine the efficacy of characterization of crystalline solids using this technique. This work aims to explore the possibilities and limitations of multinuclear high field solid state nuclear magnetic resonance in conjunction with quantum mechanical computations in an effort to explore the fundamental properties of solids.

1.1 Chemical Systems Under Review

The systems under review in this work, while seemingly uncomplicated chemically, have poorly defined or unknown fine structural details. The use of solid-state nuclear magnetic resonance (SS-NMR) is a powerful technique for characterizing structure and interactions in solids. In many cases SS-NMR can be complimentary to

Neutron Powder and X-Ray (Powder and Single-Crystal) Diffraction (PXRD and SCXRD, respectively) studies in providing a detailed structural analysis.¹ Diffraction techniques are particularly sensitive to long-range order interactions, whereas, SS-NMR is typically sensitive to short-range order interactions. This sensitivity allows for the determination of fine structural details in solids. Ultimately, understanding the fine structure of a material allows the possibility of chemical modification or tailoring to a specific requirement or purpose.

With recent advancements in the area of SS-NMR, such as the use of Ultra-high magnetic fields, various signal enhancement techniques, and advances in computational methods, such as Density Functional Theory (DFT) methods, new opportunities are arising in exploring previously non-accessible nuclei and chemical systems of increased complexity. This work is a systematic attempt at a computationally-assisted multi-nuclear ultra-high field SS-NMR study of several classes of inorganic materials to determine the efficacy and limitations of this approach in structural studies.

1.1.1 Mg-containing Materials

Magnesium is a prominent element in the fields of geology, biology, as well as chemistry. It is the ninth most abundant element in our solar system and the seventh most abundant element in the earth's crust and therefore a major component of many minerals.^{2, 3} Magnesium is also a vital element to many plant and animal biological processes.⁴⁻⁶ The omnipresent character of magnesium in nature necessitates the

development of a fundamental understanding of the chemistry of this interesting alkaline earth metal.

^{25}Mg SS-NMR should naturally provide a broad range of information on local structure and bonding environments in magnesium-containing compounds. ^{25}Mg SS-NMR, however, has seen relatively few applications, mainly due to the relative NMR-related difficulties of the ^{25}Mg nucleus. The only magnetically active isotope of magnesium, ^{25}Mg , has a relatively low natural abundance of 10% and is a quadrupolar nucleus with a spin, I , of $5/2$ and relatively large quadrupole moment of 19.94 fm^2 .⁷ The nucleus also has quite a small magnetogyric ratio, γ , of $-1.639 \cdot 10^7 \text{ rad} \cdot \text{s}^{-1} \cdot \text{T}^{-1}$ which results in correspondingly low Larmor resonance frequency. This combination of reduced natural abundance, low Larmor frequency, and quadrupolar effects can make ^{25}Mg SS-NMR a remarkable challenge. Given the experimental difficulties associated with ^{25}Mg SS-NMR, reported studies are far from abundant.

One of the earliest accounts was obtained by Derighetti *et al.* in the study of the natural mineral forsterite, or magnesium orthosilicate (Mg_2SiO_4).⁸ After this early study several magnesium containing minerals were examined, such as grandidierite,⁹ chrysotile,¹⁰ diopside¹¹ and several others¹². In these early ^{25}Mg SS-NMR studies, the signal-to-noise ratio for the obtained spectra was quite low and for the most part only peak positions are reported. There have also been several accounts of ^{25}Mg SS-NMR employed in inorganic/metallic systems, such as Mg-metal alloys,^{13, 14} Mg-doped silicon nitrides,¹⁵ silica Zener pinned nanocrystalline MgO,¹⁶ $\text{Zn}_{1-x}\text{Mg}_x\text{O}$ systems,¹⁷ various Mg-

containing salts and materials with Mg in cubic environments such as MgO, MgS, or Mg₂Si,¹⁸ and Mg metal.^{19, 20} These early works have demonstrated that ²⁵Mg SS-NMR can provide valuable information about the local environment of magnesium.²¹⁻²⁷ The sensitivity issue of ²⁵Mg NMR has been partially resolved in some cases by using samples enriched in ²⁵Mg.^{22, 24}

Given the experimental difficulties associated with ²⁵Mg NMR, the number of compounds studied has remained relatively small, and in many cases the range of ²⁵Mg NMR parameters, such as chemical shift and quadrupolar coupling constant, are either unknown or approximate. It is generally assumed that for light alkali earth metals, such as magnesium, the contribution from chemical shift anisotropy, at moderate magnetic fields, is essentially negligible. In fact, the reports of an experimentally observed chemical shift anisotropy interaction are few indeed.^{23, 24} As well, quadrupolar coupling constants (C_Q) typically reported for Mg compounds are between ~1-5 MHz.^{8, 9, 12, 20, 21, 23-25, 28} However, there are a few interesting cases where a large ²⁵Mg quadrupolar coupling constant has been reported. Wong *et al.* report a $C_Q = 13.0$ MHz and $C_Q = 12.9$ MHz for ²⁵Mg sites in monopyridinated aqua(magnesium) phthalocyanine and chlorophyll *a* respectively.²⁶ As well, Wu *et al.* report a ²⁵Mg quadrupolar coupling constant of 15.3 MHz for bis(pyridine)-(5, 10, 15, 20-tetraphenylporphyrinato)-magnesium(II).²⁷

With these previous reports in mind, the goal of this study was to perform a systematic ²⁵Mg SS-NMR study for a series of magnesium compounds with well established crystal structures in conjunction with first-principles calculations. Given the

low sensitivity of ^{25}Mg , the assessment of the viability and practicality of ^{25}Mg SS-NMR together with establishing the reasonable limits for accessible quadrupolar coupling constant, C_Q were among the main focuses of this work. Table 1 lists the magnesium-containing compounds studied in this work. The logic behind the choices made was quite straightforward.

Table 1 – Mg-containing compounds studied in this work.

MgO	Brucite, $\text{Mg}(\text{OH})_2$	$\text{MgSO}_4 \cdot 6\text{H}_2\text{O}$
$\text{Mg}(\text{NH}_4)_2(\text{SO}_4)_2 \cdot 6\text{H}_2\text{O}$	$\text{MgCl}_2 \cdot 6\text{H}_2\text{O}$	$\text{MgSO}_4 \cdot 7\text{H}_2\text{O}$
$\text{Mg}_3(\text{PO}_4)_2 \cdot 8\text{H}_2\text{O}$	$\text{MgHPO}_4 \cdot 3\text{H}_2\text{O}$	$\text{Mg}(\text{NO}_3)_2 \cdot 6\text{H}_2\text{O}$
Forsterite, Mg_2SiO_4	MgMoO_4	MgWO_4
$\alpha\text{-Mg}_2\text{V}_2\text{O}_7$	$\text{Mg}(\text{VO}_3)_2$	$\text{Mg}_3(\text{VO}_4)_2$
Geikielite, MgTiO_3	Magnesite, MgCO_3	Spinel, MgAl_2O_4
$\alpha\text{-MgSO}_4$	$\beta\text{-MgSO}_4$	$\text{Mg}(\text{HCOO})_2 \cdot \text{H}_2\text{O}$
$\text{Mg}(\text{AcAc})_2 \cdot 2\text{H}_2\text{O}$	$\text{Mg}(\text{OAc})_2 \cdot 4\text{H}_2\text{O}$	MgS
MgH_2	MgCl_2	Mg_3N_2
Mg_2Si	Mg-phthalocyanine	

An attempt was made to study Mg in different coordinating environments, in organic and inorganic frameworks, as well as study the effects, if any, of hydration on the NMR parameters of ^{25}Mg . As well, an attempt to study the peculiar coordinating environment of Mg-phthalocyanine was undertaken. Of course, one of the major considerations taken into account when deciding what compounds to study was the availability of a highly crystalline material with a very accurate crystal structure. As will be described later, an accurate crystal structure was necessary for performing the type of first-principles calculations used in this work. So, with these considerations in mind, a systematic study of the ^{25}Mg SS-NMR along with first-principles calculations were done to understand the range of interactions in the ^{25}Mg nucleus and resolve any relationships between coordinating environment of Mg and the NMR parameters. As well, with accurate

experimental NMR parameters obtained in conjunction with calculated parameters, correlations between experiment and calculation can be constructed.

1.1.2 S-containing Materials

Sulfur is yet another element that has great importance in nature and many industrial processes. It occurs as the 12th most abundant element in the universe and the 16th most abundant element in the earth's crust by mass and as a result appears in a large number of naturally occurring minerals.^{2,3}

Sulfur in the sulfate (SO_4^{2-}) form occurs in a wide variety of natural and synthetic materials and are of great importance to a number of applications and processes.²⁹ For instance, sulfates have been shown to have application as solid electrolytes for fuel cells³⁰, as an important element in concrete formation and cementous materials³¹, and as a major component in agro-chemicals.³² The importance of these materials in practical applications demands the development of a fundamental understanding of the structure and chemistry of these sulfates.

³³S SS-NMR is expected to be a very informative method to study the structure and properties of sulfate materials. However, the nuclear properties of the ³³S isotope make experimental ³³S SS-NMR even more difficult than ²⁵Mg. ³³S is the only magnetically active isotope of sulfur with a very low natural abundance of 0.75%. ³³S is also a quadrupolar nucleus with spin, $I = 3/2$, and a moderate quadrupole moment of -6.78 fm^2 .⁷ Again, similar to ²⁵Mg, ³³S has a low magnetogyric ratio, γ , of

$2.056 \cdot 10^7 \cdot \text{rad} \cdot \text{s}^{-1} \cdot \text{T}^{-1}$ resulting in a low Larmor frequency even at high field strengths. All these properties make ^{33}S SS-NMR a challenge indeed and as one would expect, previously reported studies of ^{33}S NMR in the solid-state are quite few.

The earliest natural abundance study of ^{33}S in solid materials was done by Eckert and Yesinowski on a variety of inorganic sulfur-containing materials as well as a few natural sulfur-containing minerals.³³ There are cases where the study of ^{33}S SS-NMR is not excruciatingly difficult: those in which sulfur is in a highly symmetric environment, such as cubic sulfide materials.³³⁻³⁵ However, the more typical case has sulfur in a non-symmetrical environment causing significant broadening in the experimental ^{33}S spectrum due to quadrupolar interactions. This explains why previously reported studies are typically limited to relatively small quadrupolar coupling constants up to 2 MHz. These studies are mostly concerned with sulfates or aluminum sulfates, and performed at natural abundance.^{33, 34, 36-40} More recently, quadrupolar coupling constants of up to 9.3 MHz were reported for ^{33}S in layered sulfides of transition metals⁴¹ and quadrupolar coupling constants up to 16 MHz have been reported in condensed sulfates.⁴²

Most of the previously reported ^{33}S SS-NMR has been done at moderate field strengths and the signal to noise ratio is often poor. The accuracy of the derived spectroscopic parameters can be often questioned. One of the preliminary goals of this study is to systematically inspect the early ^{33}S SS-NMR of anhydrous sulfates and attempt to improve the accuracy of the experimental data by working at ultra-high magnetic field. The next step is to examine the correlations between the spectroscopic

and structural parameters. One of the interesting things about a large majority of known anhydrous sulfates is the abundance of reported crystal structures for the same material. Table 2 shows the anhydrous sulfates studied in this work and the number of reported crystal structures associated with each material.

Table 2 – Reported crystal structures for sulfates studied in this work.

Compound	Number of Structures (Year Solved)	Compound	Number of Structures (Year Solved)
Li ₂ SO ₄	2 (1964 ⁴³ and 1976 ⁴⁴)	CaSO ₄	2 (1964 ⁴³ and 1975 ⁴⁵)
Na ₂ SO ₄	2 (1964 ⁴³ and 1975 ⁴⁶)	SrSO ₄	1 (1998 ⁴⁷)
K ₂ SO ₄	1 (1995 ⁴⁸)	BaSO ₄	5 (1964 ⁴³ , 1967 ⁴⁹ , 1977 ⁵⁰ , 1978 ⁵¹ , and 1998 ⁴⁷)
Rb ₂ SO ₄	2 (1974 ⁵² and 2010 ⁵³)	ZnSO ₄	1 (1988 ⁵⁴)
Cs ₂ SO ₄	2 (1964 ⁴³ and 2010 ⁵⁵)	Al ₂ (SO ₄) ₃	1 (1993 ⁵⁶)
(NH ₄) ₂ SO ₄	3 (1964 ⁴³ , 1966 ⁵⁷ , and 2010 ⁵⁸)	Ga ₂ (SO ₄) ₃	1 (1995 ⁵⁹)
α-MgSO ₄	1 (2007 ⁶⁰)	In ₂ (SO ₄) ₃	1 (1995 ⁵⁹)
β-MgSO ₄	2 (2007 ⁶⁰ and 2007 ⁶¹)		

The experimental NMR parameters in anhydrous sulfates are compared to those calculated for various reported crystal structures. Although most structures are relatively simple, the deviations among those reported can be quite substantial. One can expect that from a locally-sensitive technique such as NMR these deviations can be detected. Thus, in addition to examining the raw ³³S SS-NMR experimental results, a structural assessment can be made on the existing structural database given calculated and experimental SS-NMR parameters.

1.2 Solid-State NMR

1.2.1 General Considerations

Nuclear magnetic resonance spectroscopy, in general, is a powerful technique capable of probing a variety of local interactions. The method is based on an intrinsic nuclear property called spin. For fermions, such as protons and neutrons, the total intrinsic spin of each particle is $1/2$. When protons and neutrons are brought together in a nucleus, the combination of these particles creates non-degenerate total nuclear spins for the entire nucleus. The ground state nuclear spin, I , is typically what is reported for a given isotope of a given nucleus. For example, ^1H ($I = 1/2$), ^{13}C ($I = 1/2$), ^{14}N ($I = 1$), ^{25}Mg ($I = 5/2$), ^{33}S ($I = 3/2$), etc. The ground state nuclear spin of a nucleus then gives rise to $(2I + 1)$ -degenerate spin states ranging from $-I$ to $+I$. When these spins are placed in a magnetic field, these spin states become non-degenerate. This effect is called nuclear Zeeman splitting and can be seen in Figure 1.

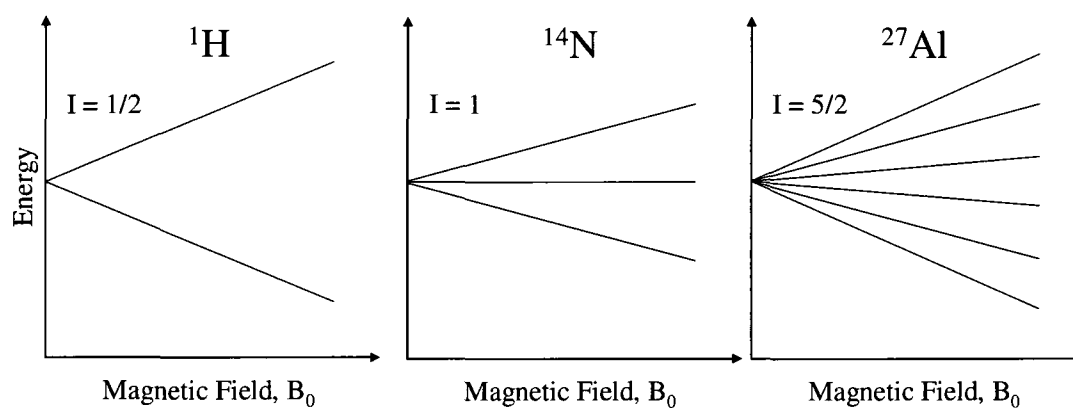


Figure 1 – Nuclear Zeeman splitting for the ^1H , ^{14}N , and ^{27}Al nuclear ground states. (adapted from ⁶²)

Note that the relative splittings between the spin states of different nuclei at the same magnetic field are different. The separation is proportional to the intrinsic magnetic moment and spin of a given nucleus, and related by the proportionality constant, γ , or the magnetogyric ratio. The energy of a spin state is given as:

$$E = -\gamma m_I \hbar B_0 \quad [1]$$

and the difference in energy between spin states is:

$$\Delta E = \gamma \hbar B_0 \quad [2]$$

The nucleons that make up a nucleus have an intrinsic magnetic moment thus giving atomic nuclei an intrinsic magnetic moment. Nuclei that have a non-zero nuclear spin will then have a non-zero magnetic moment. Interaction of the nuclear spin of a given nucleus with an external magnetic field gives rise to spin precession. This spin precession action can be viewed as similar to the precession of a spinning top in the presence of gravitational field. For a nucleus, this precession frequency is called the Larmor frequency and is given by:

$$\omega_0 = -\gamma B_0 \quad [3]$$

where ω_0 is the angular Larmor frequency, γ is the magnetogyric ratio of a given nucleus and B_0 is the strength of the external magnetic field at that particular nucleus. While this precession happens continuously, tiny distortions, from a variety of sources, in the external field felt by a particular nucleus cause fluctuations in the orientation of the nucleus' magnetic moment. These fluctuations break the isotropy of the nuclear spin polarization and a macroscopic nuclear magnetic moment will begin to develop. The Zeeman interaction will dictate, at a given temperature, that a particular orientation of the

nuclear spin states is lower in energy. This leads to a slightly higher probability to find the nuclear spin at the lower magnetic energy state. In a large ensemble of non-interacting spins, there will be a slightly larger population of spins in the lower energy state. The difference in populations of the energy levels at thermal equilibrium results in bulk magnetization within a sample and is the origin of an NMR signal. With practically obtainable magnetic field strengths, the energy difference between different spin states is typically four to six orders of magnitude lower than the available thermal energy at room temperature. In practice, this means that the bulk magnetization in the direction of the external magnetic field is virtually immeasurable.

To get around this detriment, NMR spectroscopy makes use of induced transverse magnetization. As mentioned earlier, the Larmor precession frequency of a given nucleus comes about as a result of the interaction with the external magnetic field. This frequency is typically in the r.f. or radio frequency range of the electromagnetic spectrum. If one applies a r.f. pulse perpendicular to the external magnetic field that is on-resonance with the Larmor frequency of the spins of interest, a rotation of the bulk magnetization occurs. The r. f. pulse rotates the net magnetization into a plane perpendicular to the external magnetic field called the transverse plane. This is also called a 90° or $\pi/2$ pulse. If the length of the pulse is doubled, the magnetization will invert its direction from thermal equilibrium. This pulse is called a 180° or π pulse. The spins in the transverse plane will still precess at their Larmor frequency, inducing a magnetic field which oscillates at the Larmor frequency. This transverse magnetic field can be detected producing an

observable NMR signal. This was first demonstrated independently by Felix Bloch⁶³ and Edward Purcell⁶⁴ in 1946 and resulted in the Nobel Prize in Physics for both in 1952.

If all nuclei of the same type precessed at exactly their Larmor frequency, then NMR spectroscopy would be quite uninteresting and suitable perhaps only for accurate measurements of the nuclear magnetic moment. In fact, it is minor perturbations in the Zeeman interaction from external and internal sources that provide interesting and detailed insights into the chemical environments of a given nucleus.

When considering the state of a given system, one typically must consider the motions and positions of the nuclei as well the extremely large number of electrons in the system. The quantum state of an entire system can be described by a wavefunction that contains information about the motion, positions, and spin states of all electrons and nuclei. This wavefunction obeys the time-dependent Schrödinger equation:

$$\frac{d}{dt}|\psi_{full}(t)\rangle = -i\hat{H}_{full}|\psi_{full}(t)\rangle \quad [4]$$

where \hat{H}_{full} contains all interactions within a system. Although complete, this equation is almost impossible to solve for any realistic system. Typically for NMR, the interactions within the entire system are simplified to include only the terms which may affect the nuclear spin states. This means that the time-dependent Schrödinger equation can be simplified to:⁶²

$$\frac{d}{dt}|\psi_{spin}(t)\rangle \equiv -i\hat{H}_{spin}|\psi_{spin}(t)\rangle \quad [5]$$

where $|\psi_{spin}(t)\rangle$ is the spin state of the nuclei and \hat{H}_{spin} is the nuclear spin Hamiltonian, which only contains terms that involve interactions in the nuclear spin states. This simplification largely makes the assumption that contributions from fast-moving electrons can be averaged due to the differences in time-scale for nuclear motions compared to electron motions.⁶² As such, the spin Hamiltonian can be separated into various interactions that are of interest to NMR spectroscopy. The largest contribution for a typical NMR experiment comes from the external magnetic field, creating the well known Zeeman splitting. The other main external interaction is the applied r.f. pulse applied perpendicular to the static external field. This r.f. field is used both to create the transverse magnetization and to probe the internal spin interactions. There are numerous internal spin interactions that can give interesting insights into the state of the system. The most common interaction examined is the chemical shielding interaction. Chemical shielding is the result of a magnetic shielding effect the surrounding electrons have on the nucleus of interest. Given the importance of this interaction, it will be explained more thoroughly in Section 1.2.2. The other major interaction important for this work is the quadrupolar coupling interaction, which describes the electric interaction between nuclei with $I > 1/2$ and the surrounding electric field gradients. This interaction is also explained in more detail in a further section. There are also 2-spin interactions that can be used to probe possible connections between nuclei. One of them is the direct dipole-dipole interaction responsible for through-space magnetic interactions between 2 spins. The other is the scalar or J-coupling interaction which examines through-bond electron mediated magnetic interactions between spin pairs. There are also some other weak or situation-specific interactions that can have an effect of the NMR spectrum. Among them

is the spin-rotation interaction, which examines the interaction of nuclear spins with magnetic fields generated from molecular motion. There is also the paramagnetic interaction present in systems with unpaired electrons. Lastly, the interaction of a nucleus with conduction electrons is responsible for the Knight shift and is present in conductive or metallic systems. These last interactions, however, are not pertinent to the systems under study in this work and so are simply mentioned for completeness.

One extremely important consideration for all interactions in NMR is the state of matter of the studied system. When the system is in a gaseous or liquid state, motional averaging of individual molecules simplifies the majority of interactions to only their isotropic components. For these applications typically the isotropic chemical shielding interaction and the scalar-coupling interaction are studied. However, when the system under study is in the solid-state the interactions, for the most part, are anisotropic and become increasingly complex. The strength of the anisotropic components of the major interactions can sometimes impair the ability to observe the weaker interactions that may be present in a system. For this reason the majority of SS-NMR is concerned with the shielding, the quadrupolar coupling (in the case of $I > 1/2$) and dipole-dipole interactions. In a practical setting, dipole-dipole interactions can complicate spectra to the point that the useful information cannot be resolved. Fortunately, there are experimental techniques, such as magic angle spinning (MAS) or high-power decoupling that can be used to eliminate or reduce the effect of dipole-dipole interactions.

1.2.2 Nuclear Shielding

As mentioned earlier, the shielding interaction is the effect surrounding electrons have on the magnetic field experienced by a given nuclear spin. That is, the magnetic field experienced by a particular spin will be dependent on the chemical environment of the spin of interest. This effect arises from the external magnetic field generating induced electronic currents in the surrounding electron cloud, which in turn generates a magnetic field. This induced magnetic field effectively screens or shields the nuclei of the system from the external, static magnetic field. The fundamental development of this effect has first shown by Ramsey⁶⁵⁻⁶⁸ and Pople^{69, 70} and the actual magnetic field experienced by a given nucleus can be simplified to:

$$B_{nuc} = (1 - \sigma)B_0 \quad [6]$$

or written as the Hamiltonian of the interaction:

$$\hat{H}_{CS} = -\gamma B_0 \cdot \sigma \cdot \hat{I} \quad [7]$$

where B_{nuc} is the magnetic field experienced by the nucleus, B_0 is the external magnetic field, γ is the magnetogyric ratio of the given nucleus, I is the nuclear spin operator, and σ is the so-called chemical shielding interaction. The shielding at a given nucleus is quite sensitive to the local electron density and so different chemical environments can typically be distinguished on the basis of precession frequency differences arising from different magnetic fields experienced by those environments. σ is not simply a scalar value representing either an increase or decrease in the magnetic field experienced at the nucleus, but is in fact a 2nd rank tensor, which can be written as a 3x3 matrix, that is

dependent on the orientation of a given nuclear environment. For example, if a fixed axis system is placed such that the external magnetic field is along the z-direction, then [6] becomes:

$$\begin{bmatrix} B_{nucl,x} \\ B_{nucl,y} \\ B_{nucl,z} \end{bmatrix} = \left(1 - \begin{bmatrix} \sigma_{xx} & \sigma_{xy} & \sigma_{xz} \\ \sigma_{yx} & \sigma_{yy} & \sigma_{yz} \\ \sigma_{zx} & \sigma_{zy} & \sigma_{zz} \end{bmatrix} \right) \cdot \begin{bmatrix} 0 \\ 0 \\ B_0 \end{bmatrix} \quad [8]$$

This shielding tensor is antisymmetric but can be decomposed into a symmetric part and an antisymmetric part. However, the observable component of the shielding tensor, accurate to first-order, is symmetric in nature ($\sigma_{xy} = \sigma_{yx}$).⁷¹ The antisymmetric part of the shielding tensor has such little effect that in real systems it is nearly impossible to detect.^{72, 73} As such, the symmetric part of the shielding tensor can be diagonalized into its own principal axis system of PAS and thus can be rewritten as:

$$\sigma_{PAS} = \begin{bmatrix} \sigma_{11} & 0 & 0 \\ 0 & \sigma_{22} & 0 \\ 0 & 0 & \sigma_{33} \end{bmatrix} \quad [9]$$

The diagonal elements of the tensor are referred to as the principal components of the shielding tensor. Standard convention orders the components as: $\sigma_{11} < \sigma_{22} < \sigma_{33}$.⁷⁴ The isotropic shielding, σ_{iso} , is defined as:

$$\sigma_{iso} = \frac{1}{3} Tr(\sigma) = \frac{1}{3} (\sigma_{11} + \sigma_{22} + \sigma_{33}) \quad [10]$$

Other useful parameters obtained from manipulation of the components of the shielding tensor are the chemical shielding anisotropy parameter, $\Delta\sigma_{aniso}$, and the chemical

shielding asymmetry parameter, η_{CSA} , as defined by the Haeberlen convention^{75, 76}, where:

$$|\sigma_{33} - \sigma_{iso}| \geq |\sigma_{11} - \sigma_{iso}| \geq |\sigma_{22} - \sigma_{iso}| \quad [11]$$

$$\Delta\sigma_{aniso} = \sigma_{33} - \frac{(\sigma_{11} + \sigma_{22})}{2} \quad [12]$$

$$\eta_{CSA} = \frac{(\sigma_{22} - \sigma_{11})}{(\sigma_{33} - \sigma_{iso})} \quad [13]$$

As mentioned previously, the shielding interaction experienced by a particular spin has a dependence on the relative orientation of the molecule or chemical site as well as the symmetry of the surrounding electron density. Generally, the electron density around a nuclear centre is not spherically symmetric and contributes to the CSA interaction. However, if there is a large degree of molecular mobility (i.e. translational or rotational mobility) in a sample, one will typically only observe and measure an average of the shielding interaction, or the isotropic chemical shielding, σ_{iso} , similar to the case of NMR in liquids. If one has a finely ground crystalline solid, then a powder-averaged pattern is observed giving the information necessary to describe the CSA of given nuclear spin. A typical powder pattern dominated by the CSA interaction can be seen in Figure 2.

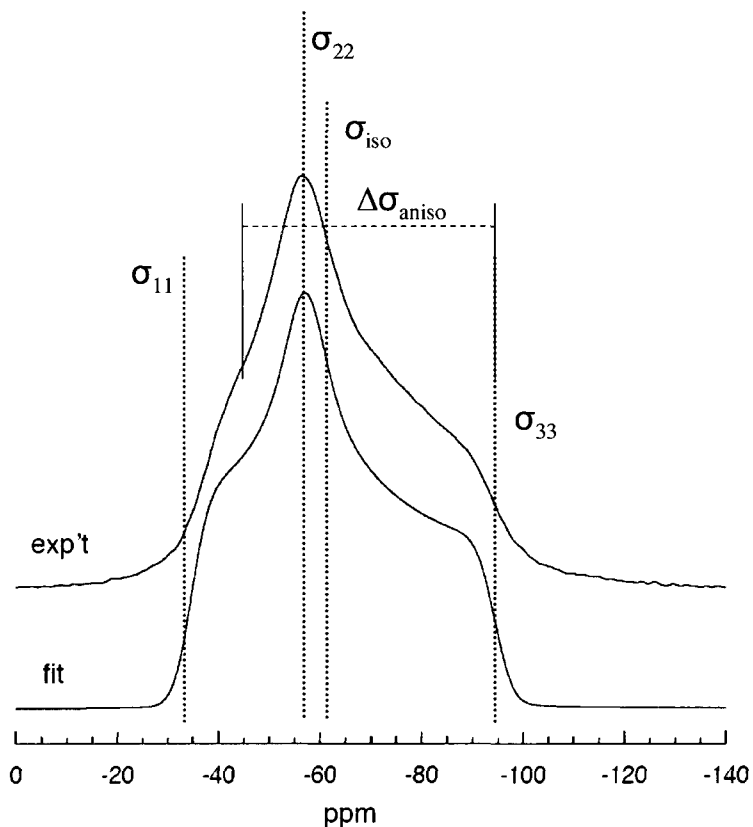


Figure 2 –Experimental CSA interaction-dominated SS-NMR powder pattern for ^{29}Si in Co-doped forsterite (Mg_2SiO_4). Relative positions of the principal shielding components are shown. It should be noted that the “ppm” scale reflects the experimental chemical shift scale, δ , not shielding. (adapted from ⁷⁷).

Another point of interest concerning the CSA interaction (and some other interactions in SS-NMR, in general) is the description of this interaction in terms of the 2nd order Legendre polynomial (based on the cosine function). That is, the anisotropic parts of the interaction rely on the relation $(3\cos^2\theta - 1)$ where θ is the angle between the principal component of an axially symmetric shielding tensor, σ_{33} , and the external magnetic field. Without going into further detail, it can be shown that spinning a crystalline powder sample at high speeds can average the anisotropic components of the shielding tensor giving simply the isotropic shielding component, known as magic angle spinning or MAS.^{78, 79} This effect can be seen in Figure 9.

It is important to note that actual values for shielding parameters are generally quite small, on the order of 10^{-6} with respect to the Zeeman interaction, and are generally reported in parts per million, or ppm. Since it is difficult to measure exact or absolute shielding values, especially due to the variation between environments,⁸⁰ this interaction is reported as an observable difference, called the “chemical shift”, δ , with respect to a reference material. The shielding interaction of the reference is ideally as close to a shielding interaction of zero, or a bare nucleus, as possible. The chemical shift scale is related to the shielding scale as follows:

$$\delta_{ij} = \frac{\sigma_{iso,ref} - \sigma_{ij}}{1 - \sigma_{iso,ref}} \quad [14]$$

where $\sigma_{iso,ref}$ is the isotropic shielding of the reference, σ_{ij} is the shielding component of interest, and δ_{ij} is the position of the corresponding component relative to the reference. Typically the chemical shift is reported with respect to a common accepted reference. For example, tetramethylsilane, or TMS, is used as a $\delta_{iso} = 0$ ppm chemical shift reference for ^1H , ^{29}Si and ^{13}C NMR.

1.2.3 Quadrupolar Interaction

The other interaction that is important for this work and SS-NMR, in general, is the quadrupolar interaction. This interaction, in contrast to the magnetic character of the shielding interaction, is an electrostatic interaction that a nucleus of spin $> 1/2$ has with the surrounding electric fields. This interaction arises from the fact that nuclei that have a

ground state spin $> 1/2$ have a non-spherically symmetric charge distribution. A pictorial description of the charge distribution in a nucleus is shown in Figure 3. The electric dipole moment of a nucleus is always zero, while for nuclei with ground state spin $> 1/2$ the quadrupole moment is non-zero.

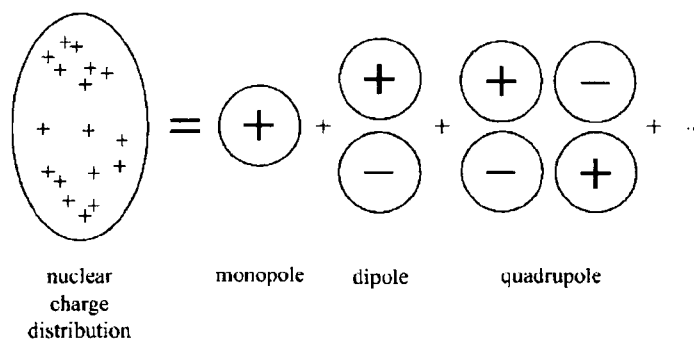


Figure 3 – Schematic of the charge distribution in a nucleus. The quadrupole moment is non-zero for nuclei with ground state spin $> 1/2$. (adapted from ⁸¹)

This quadrupole moment can interact with the electric field gradients created by the distribution of electrons in a given molecule. A simplified example of an electric field gradient created by a linear molecule can be seen in Figure 4.

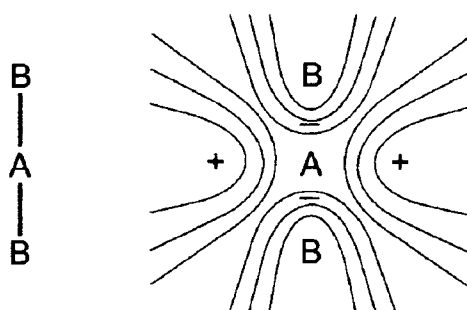


Figure 4 – A model linear molecule AB_2 , shown on left, would generate an electric field gradient. The gradient generated from the electronic distribution in this linear molecule would resemble the diagram on the right. (adapted from ⁸¹)

Quadrupolar interactions can be described by the following Hamiltonian:

$$\hat{H}_Q = \frac{eQ}{6I(2I-1)\hbar} \hat{I} \cdot V \cdot \hat{I} \quad [15]$$

where eQ is the nuclear electric quadrupole moment, I is the spin operator, and V is the second-rank tensor, similar to the shielding tensor, that describes the electric field gradient, EFG, at the nucleus of interest. Again, similar to the shielding interaction, the electric field gradient can be written as a symmetric, traceless 3x3 matrix such as:

$$V = \begin{bmatrix} V_{xx} & V_{xy} & V_{xz} \\ V_{yx} & V_{yy} & V_{yz} \\ V_{zx} & V_{zy} & V_{zz} \end{bmatrix} \quad [16]$$

Again, this tensor can be diagonalized such that it is in its own PAS and thus rewritten as:

$$V = \begin{bmatrix} V_{11} & 0 & 0 \\ 0 & V_{22} & 0 \\ 0 & 0 & V_{33} \end{bmatrix} \quad [17]$$

with the elements ordered as $V_{33} \geq V_{22} \geq V_{11}$.⁸² The EFG tensor is traceless, so $V_{33} + V_{22} + V_{11} = 0$. Useful parameters that are commonly reported for the quadrupolar interaction are:

$$eq = V_{33} \quad [18]$$

$$C_Q = \frac{eqeQ}{h} \quad [19]$$

$$\eta_Q = \frac{V_{11} - V_{22}}{V_{33}} \quad [20]$$

where eq is the principal component of the EFG tensor, C_Q is the quadrupolar coupling constant, Q is the nuclear quadrupole moment, and η_Q is the asymmetry parameter. It should be noted that C_Q is typically on the order of MHz. Given the definition of the EFG tensor and the fact that it is traceless, it follows that the $0 \leq \eta_Q \leq 1$.

The effect this interaction has on the transitions between nuclear spin states is not as straightforward as in the case of the shielding. The quadrupolar interaction, in the high-field case where the interaction is considered as a perturbation from the Zeeman interaction, can be reasonably truncated to second-order, such that the Hamiltonian for this interaction can be described as⁸³:

$$\hat{H}_Q = \hat{H}_Q^{(1)} + \hat{H}_Q^{(2)} \quad [21]$$

The first order term simplified by assuming an axially symmetric EFG tensor, $\eta_Q = 0$, can be written as:

$$\hat{H}_Q^{(1)} = \frac{eqeQ}{4I(2I-1)} \frac{3\cos^2\theta - 1}{2} (3\hat{I}_z^2 - I(I+1)\hat{1}) \quad [22]$$

where θ is the angle between the principal component of the EFG tensor and the external magnetic field, B_0 . The second-order component of the quadrupolar interaction is much more complicated and can be written (again assuming $\eta_Q = 0$ for simplicity) as:

$$\hat{H}_Q^{(2)} = -\left(\frac{eqeQ}{4I(2I-1)}\right)^2 \frac{2}{5\omega_0} \left\{ \begin{aligned} &\left(\frac{9}{5}\hat{A}_z - \frac{3}{5}\hat{I}_z(3-4I(I+1))\right) + \\ &\left(\frac{18}{7}\hat{A}_z + \frac{3}{14}\hat{I}_z(3-4I(I+1))\right)\left(\frac{3\cos^2\theta-1}{2}\right) + \\ &\left(-\frac{153}{35}\hat{A}_z + \frac{27}{70}\hat{I}_z(3-4I(I+1))\right)\left(\frac{35\cos^4\theta-30\cos^2\theta+3}{8}\right) \end{aligned} \right\} \quad [23]$$

where,

$$\hat{A}_z = (5\hat{I}_z^2 - 3I(I+1) + 1)\hat{I}_z \quad [24]$$

and ω_0 is the Larmor frequency. Note that the second-order quadrupolar interaction is inversely proportional to the Larmor frequency, meaning that increasing the static, external field will decrease the strength of this interaction.

One may recall from Figure 1 that more than one transition exists for spin $>1/2$. When the quadrupolar Hamiltonian is applied to these different spin eigenstates, various shifts in the energies are observed. The so-called central, or $|+1/2\rangle \leftrightarrow |-1/2\rangle$ transition, is unaffected to first-order by the quadrupolar interaction, whereas all transitions are affected to second-order. A schematic of these energy shifts can be seen in Figure 5 for a general $I = 5/2$ nucleus.

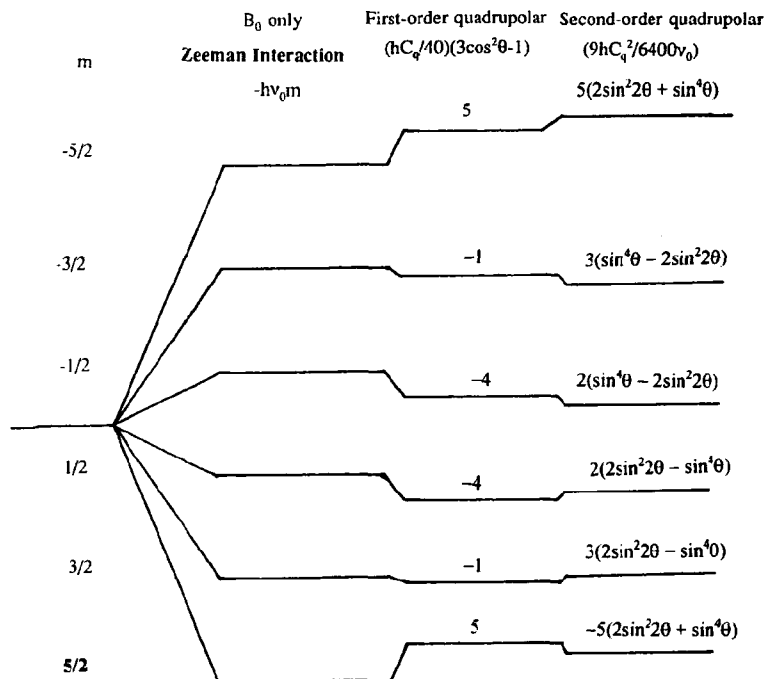


Figure 5 – Energy splitting diagram for a typical $I = 5/2$ nucleus showing the degree to which the quadrupolar interaction affects the energy of each transition. (adapted from ⁸⁴)

Typically, the satellite transitions ($|+3/2\rangle \leftrightarrow |-3/2\rangle$, $|+5/2\rangle \leftrightarrow |-5/2\rangle$, etc.) are difficult to observe for systems with a large C_Q given the large frequency range of all transitions. Therefore, only the central transition is usually observed and all data reported herein refer to the central transition of a given nucleus, unless otherwise stated. It should be noted that for integer spin nuclei, such as ^{14}N ($I = 1$), ^2H ($I = 1$), ^{10}B ($I = 3$), etc., there is no central transition and typically the $|+1\rangle \leftrightarrow |0\rangle$ and $|-1\rangle \leftrightarrow |0\rangle$ transitions are observed, which are affected to first-order by the quadrupolar interaction. However, since this study is only concerned with half-integer spin nuclei, integer spin transitions are only mentioned here in passing.

From equations [22] and [23] and Figure 5 it can be seen that there is an angular dependence of the interaction between the EFG tensor and the static, external magnetic

field. This anisotropy can be exploited to determine various NMR interaction parameters for a given system. Similar to the shielding interaction, if a sample is undergoing MAS, the first-order quadrupolar interaction can be averaged to zero, leaving only the partially averaged second-order quadrupolar interaction. This leaves the commonly observed second-order central transition powder averaged lineshape for a typical quadrupolar nucleus. The typically observed central transition powder pattern lineshapes for various values of η_Q can be seen in Figure 6. Figure 7 shows the effect the quadrupolar coupling constant, C_Q , has on the observed lineshape for the central transition of a system under MAS and Figure 8 shows how C_Q and η_Q can be determined from an experimental spectrum.

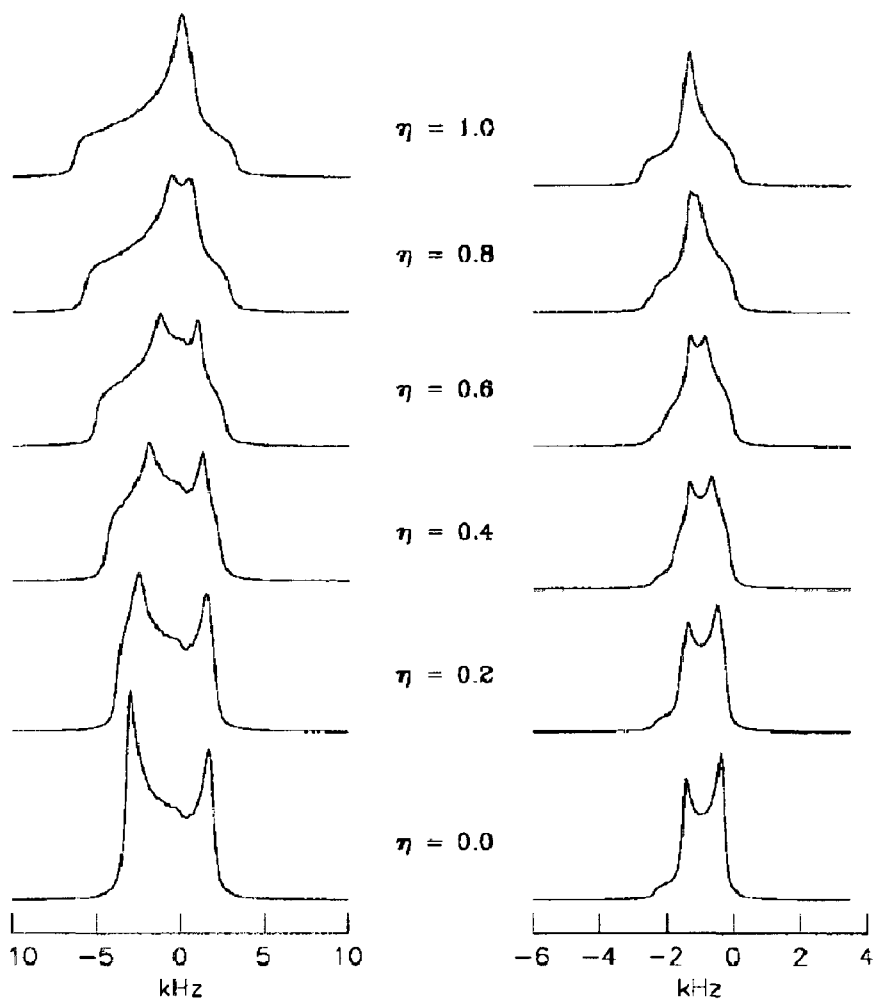


Figure 6 – Typical central transition powder patterns for a quadrupolar interaction for different values of η_Q . The static lineshape is shown on the left, where the right shows a typical MAS central transition lineshape dominated by the 2nd order quadrupolar interaction. Note also that conventionally the frequency axis is reported as decreasing to right, opposite of what is shown here. (adapted from ⁸¹)

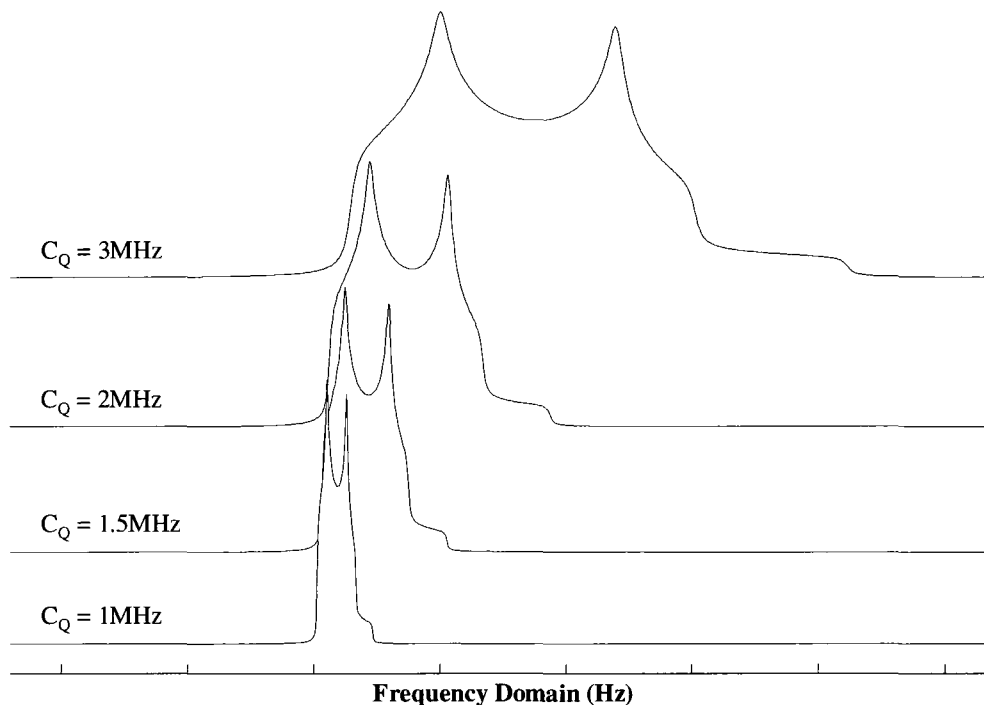


Figure 7 – Effect of the quadrupolar coupling constant, C_Q , on the central transition MAS powder pattern for a typical quadrupolar interaction-dominated system. ($\eta_Q = 0.3$; $I = 3/2$)

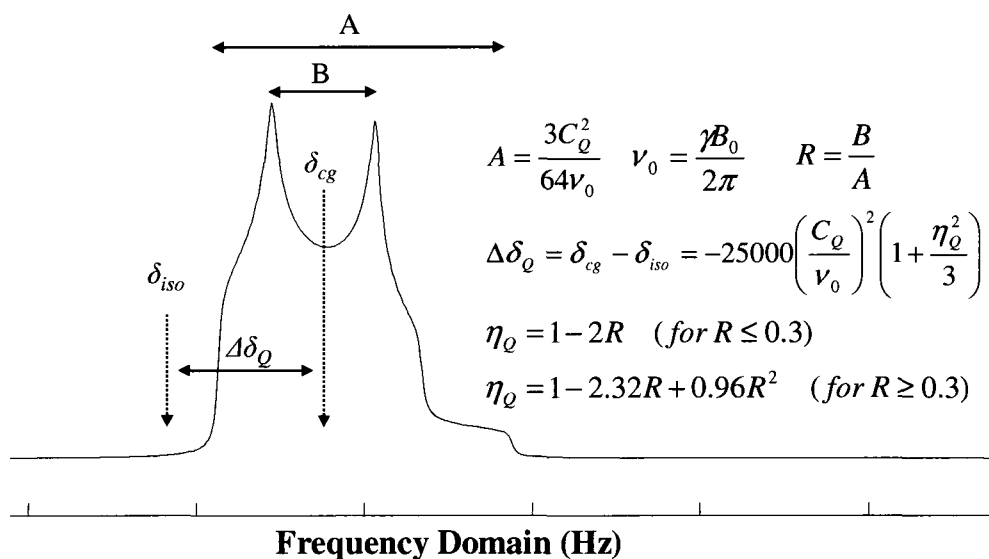


Figure 8 – Visible singularities of the central transition of a quadrupolar interaction dominated system under MAS ($C_Q = 2$ MHz, $\eta_Q = 0.3$, $I = 3/2$). (adapted from ^{85, 86})

1.2.4 Experimental Techniques

Over the past several decades, numerous technical and experimental developments have advanced the area of NMR spectroscopy. Dramatic improvements in sensitivity and resolution have revolutionized SS-NMR and made possible studies of previously unattractive or almost impossible nuclei and chemical systems.

One of the major improvements has been the continuous increase in magnetic field strength of commercially available superconducting magnets. Magnets in the range of 17.6-22.3 T are now readily accessible. As shown in Figure 1, an increase in the magnetic field strength has the immediate benefit of increasing the Larmor resonance frequency and subsequently the energy difference between nuclear spin states. This creates a larger population difference between spin states at thermal equilibrium and thus improves the intensity of the NMR signal. As well, the increase in magnetic field strength has the added benefit of improved sensitivity and resolution for quadrupolar nuclei due to the inverse relationship between the 2nd order quadrupolar interaction and the Larmor resonance frequency.^{81, 87} This increased sensitivity allows for a substantial increase in the range of quadrupolar coupling constants accessible by SS-NMR. The other added benefit of larger magnetic fields is improved resolution in the spectra due to the linear relationship between chemical shielding and magnetic field strength. This improves accuracy in the experimentally determined chemical shifts as well as presenting a better chance of detecting and accurately evaluating chemical shielding anisotropy, especially

in the case of low- γ nuclei such as ^{25}Mg , ^{33}S , or ^{43}Ca , where CSA is difficult to measure, in general.

Another important improvement especially useful for SS-NMR of low- γ , quadrupolar nuclei is the use of line-narrowing and sensitivity enhancing techniques. The most common line narrowing technique used for SS-NMR is magic angle spinning or MAS.^{78, 79, 88} It was previously shown that for the chemical shielding and quadrupolar interaction (as well as the dipole-dipole interaction⁸⁹) all have a dependence on the 2nd order Legendre polynomial, which is $(3\cos^2\theta - 1)$. This function has a zero point at an angle of 54.74° . Experimentally it results in an interesting effect that can occur when a powdered sample is placed at 54.74° to the static, external magnetic field and then spun at high speeds (typically from a few kHz to tens of kHz). The interactions present for each nuclear spin within a given crystallite become time dependent. At this angle, called the magic angle, each crystallite experiences an average of the various interactions and eliminates the anisotropy that would normally broaden a spectrum. For the CSA interaction, the anisotropy is broken up into “spinning sidebands” that resembles the original powder pattern and are spaced apart an amount equal to the spinning frequency. When spun sufficiently high enough, only the isotropic peak remains. An example of how this effect works on a real sample can be seen in Figure 9.

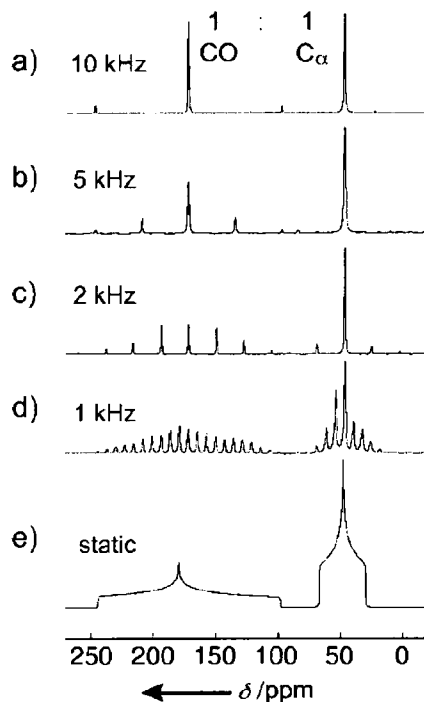


Figure 9 – Solid-State ^{13}C NMR spectra (at $B_0 = 11.7$ T) of a labeled glycine powder sample. MAS spinning speed is shown in each spectrum and e) shows the static CSA powder pattern. As spinning speed is increased the anisotropy is averaged to only the isotropic peak (a)). (adapted from ⁹⁰).

The effect on the quadrupolar interaction is somewhat more complicated. Since only the first-order component of the interaction is dependent on $(3\cos^2\theta - 1)$, the first order component is averaged under MAS, but the second order component is only partially averaged, giving a typical second order quadrupolar lineshape, as seen in Figures 6 and 7.

Another ubiquitous sensitivity enhancing technique common to SS-NMR of quadrupolar nuclei is the Carr-Purcell-Meiboom-Gill, or CPMG,^{91, 92} and more specifically the quadrupolar CPMG^{93, 94}, or QCPMG technique. The CPMG technique is based on Hahn's spin-echo⁹⁵ and quadrupolar echo⁹⁶⁻⁹⁸ technique, widely used in NMR spectroscopy to reduce the adverse effects of having a short effective spin-spin relaxation

time, T_2^* , by refocusing the transverse magnetization at a time τ after the last pulse. Essentially, the CPMG technique makes use of the fact that spin-spin relaxation time, T_2 , is generally longer than the effective spin-spin relaxation time, T_2^* , that results from field inhomogeneities and internal interactions that cause inhomogeneous line broadening. In the CPMG technique, a standard Hahn echo is applied, followed by a series of 180° pulses to constantly refocus the transverse magnetization, for which the signals can then be recorded. A schematic diagram of the Hahn echo and QCPMG pulse sequences can be seen in Figure 10. The QCPMG sequence, then, creates a train of echoes with each echo representing the full pattern. When the Fourier transform of the time domain is executed, a spikelet pattern, similar to spinning sidebands under MAS, representing the entire powder pattern appears. The spikelet separation in QCPMG, however, is based on the echo time delay instead of the spinning speed in MAS. Generally speaking, the QCPMG technique can give sensitivity enhancements of an order of magnitude compared to the regular echo techniques. This greatly reduces the time required for obtaining high quality spectra for nuclei with large quadrupolar interactions. The QCPMG technique can be further combined with MAS,⁹⁹ allowing an additional significant signal enhancement at improved resolution.

There are various other signal enhancement techniques that exist that can be used in conjunction with the QCPMG, echo, or basic one-pulse acquisition. One example is the Rotor-Assisted Population Transfer, or RAPT,¹⁰⁰ sequence. This technique is used to enhance the central transition of half integer quadrupolar nuclei. It consists of a train of very short pulses of opposite phase followed by the usual pulse sequence (QCPMG, echo,

etc.) as shown in Figure 10. These short pulses effectively saturate the satellite transitions increasing the population difference between the central transition producing a theoretical enhancement of $(I+1/2)$. Other central transition enhancement techniques include Double-Frequency Sweeps (DFS)¹⁰¹ and Hyperbolic Secant (HS)¹⁰² pulses. Like RAPT, these pulses affect the satellite transitions, however, for DFS and HS the frequency of excitation is swept in such a manner that the satellite transitions are inverted instead of saturated. This ultimately gives a theoretical signal enhancement of $(2I)$ if both satellites are inverted. A schematic of these pulse sequences can be seen in Figure 10. A serious problem with acquiring high quality spectra of quadrupolar nuclei, aside from the general sensitivity problem, is excitation of very broad, sometimes several MHz wide, NMR spectra. Commonly used rectangular pulses provide a rather finite frequency excitation range of about 100 kHz at best. A recently introduced technique that addresses this issue is the adiabatic wideband uniform-rate smooth truncation (WURST) pulse¹⁰³ that can also be coupled to the QCPMG technique for further signal enhancement.¹⁰⁴ This technique is another frequency-swept pulse technique that uniformly excites a broader frequency range allowing the examination of very broad central transition patterns in one piece. An example of this can also be seen in Figure 10.

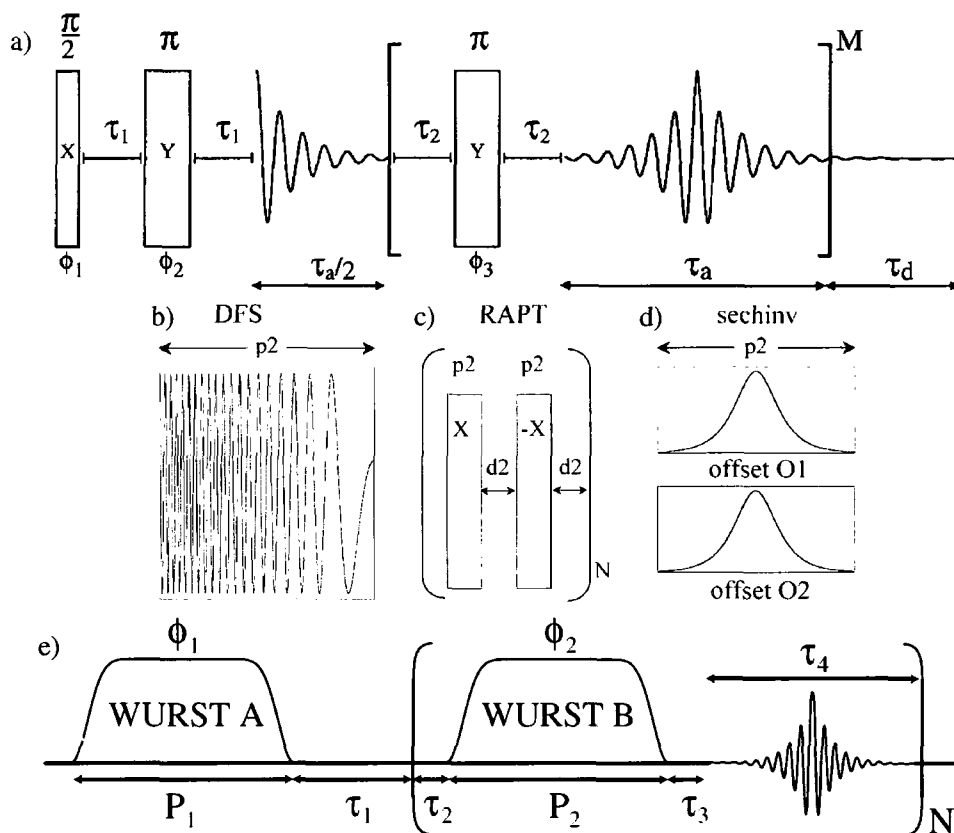


Figure 10 – Schematic diagrams of the various signal-enhancing techniques useful for observing the central transition of half-integer spin quadrupolar nuclei. a) shows the QCPMG technique, where before the π pulse train is a typical quadrupolar or Hahn echo. b) shows the amplitude modulated DFS pulse, c) shows the short phase-inverted pulse train of RAPT, and d) shows the HS or sechinv pulse. b), c) and d) pulses can be placed in front of the first $\pi/2$ of a) to give signal enhancement. e) shows the WURST-QCPMG pulse sequence used for ultra-wideline spectra.

Another important sensitivity and resolution enhancement technique that must be mentioned is heteronuclear dipolar decoupling. As already mentioned, the dipole-dipole interaction can play a significant role in SS-NMR, particularly when there are protons present in the sample. Given the high natural abundance (~99.9%) and extremely large magnetogyric ratio ($26.75 \cdot 10^7 \cdot \text{rad} \cdot \text{s}^{-1} \cdot \text{T}^{-1}$) of protons, $^1\text{H-X}$ dipole-dipole interactions can be quite strong and ultimately broaden the observed transition to the point of not being useful. $^1\text{H-X}$ dipolar coupling also has the effect of shortening the spin-spin relaxation,

T_2 , which reduces the effectiveness of the QCPMG experiment. This effect can be reduced through additional r.f. irradiation of the sample at the proton Larmor frequency. This equilibrates the populations of the proton spin states and averages out any dipole-dipole interactions with protons. The first and most commonly used decoupling scheme is the single-frequency excitation with continuous wave or CW spin decoupling, where the ^1H are irradiated constantly at a particular power level for the duration of the acquisition.^{105, 106} More efficient ^1H decoupling can be achieved by using multiple pulse and composite pulse-based techniques.^{107, 108}

1.3 Quantum Mechanical Computation of Spectral Parameters

As the level of computation power continues to rise, so too does the interest in being able to accurately predict the observables in a given system. The ability to predict NMR parameters, such as the shielding tensor and magnetic susceptibility, and electric field gradients would be extremely useful to gain *a priori* knowledge and possibly to assist in optimization of the experimental conditions or provide help in an assignment of a complicated spectrum. There has been a tremendous amount of work done on implementing Hartree-Fock, HF, and Density Functional Theory-based, DFT, approaches for predicting NMR parameters.¹⁰⁹⁻¹¹¹ These approaches work well for gas-phase systems, however, they do not reproduce the infinite, periodic nature of crystalline solids. This is typically circumvented by creating a cluster that attempts to represent the infinite solid. That cluster is then treated as a gas-phase molecule and the NMR parameters can be predicted for all atoms.¹¹²⁻¹¹⁴ As long as the order of the particular interaction does not

extend significantly beyond the boundaries of the cluster, then this method can potentially reproduce NMR parameters in the solid-state. Unfortunately, true convergence with respect to basis set and cluster size is often not possible due to the limitations of computational resources. So, to solve this problem for NMR calculations in solids, an *ab initio* DFT-based method was developed using periodic boundary conditions and pseudopotentials for the calculation of NMR shielding in solids.¹¹⁵⁻¹¹⁷ This method went through a number of iterations and improvements¹¹⁸⁻¹²¹, mostly to the nature of the pseudopotentials used, and ultimately, by using DFT, periodic boundary conditions and thus a plane wave basis set in conjunction with pseudopotentials, a method known as Gauge Including Projector Augmented Wave, or GIPAW, was developed to calculate NMR parameters for all nuclei in the solid-state without using a cluster approximation.^{118,121}

Essentially, this approach makes use of the fact that many properties of a crystalline solid are periodic in the repeating cell. So, for instance, one can write the electron wavefunctions as periodic in nature, such that:¹¹⁹

$$\psi_{n,k}(r) = u_{n,k}(r) \exp(ik \cdot r) \quad [25]$$

where $u(r)$ is periodic within the infinite solid, and so can be made into a series expansion of a set of basis functions. For this approach these basis functions are plane-waves, such that each single-electron wavefunction is:

$$\psi_{n,k}(r) = \sum_G u_{n,k}(G) \exp(i(k + G) \cdot r) \quad [26]$$

where G and k represent reciprocal wavevectors that correspond to the periodicity of the solid. However, to represent the entire infinite solid, the number of wavevectors, G and k , must be infinite. It turns out that although the number of k -vectors must be infinite, and at each a solution for $\psi_{n,k}$ exists, the change in $\psi_{n,k}$ becomes negligible as the k -points come close together. This is called k -point sampling and is sometimes referred to as the k -grid. The number of G -vectors, as well, does not need to be considered to infinity to yield accurate calculations. In fact, the number of wavevectors used for a wavefunction, and ultimately the quality of the basis set, can be controlled using a single parameter:¹¹⁹

$$E_c = \frac{\hbar(G+k)^2}{2m} \quad [27]$$

where E_c is called the cutoff energy, such that, E_c is expressed as the energy of a free electron with the wavefunction described by the largest wavevector in the plane-wave basis. So, all plane waves with a free electron energy less than the cutoff energy, E_c , are used in the expansion of the plane-wave basis. This makes it easy to determine the convergence quality of the basis set.

However, although the free-electron approach works well for valence electrons, so-called core electrons, or electrons very close to the nucleus are far from a free-electron wavefunction description. In fact, to properly describe these electrons, millions of plane-waves would be required, rendering this method impossible for core electrons. However, this problem is overcome by using pseudopotentials, which replaces the nuclear charge and core electron potential with a fixed potential below some cut-off radius, r_c . There are various constraints placed on pseudopotentials. One of the requirements is that above the

cut-off radius the pseudopotential must match the all-electron potential and the all-electron potential eigenvalue must equal that of the pseudopotential. The norm-conserving pseudopotential¹²² places the condition that the charge or integral of the pseudopotential generated wavefunction must be equal to that of the all-electron wavefunction below r_c . Although pseudopotentials remove the nodal character, and thus the overly complicated nature of the all-electron potential, the pseudopotentials can be quite hard near the nucleus. Hard pseudopotentials will generally require a large number of plane waves and thus a larger energy cut-off E_c to accurately describe the valence wave functions ultimately limiting these pseudopotentials to the study of lighter nuclei. This also has an adverse effect on the memory and computation power requirements. The development and use of Vanderbilt's ultrasoft pseudopotentials¹²³ has been implemented with the GIPAW formalism¹²⁰ to calculate chemical shielding and thus can be applied to a variety of heavier nuclei. This method of calculating NMR parameters has been made available in the CASTEP computational module.^{119, 121} First principles computations in SS-NMR have seen considerable use in recent years in a variety of disciplines, including biochemistry, earth sciences and silicate research.¹²⁴⁻¹³⁰

2. Experimental Details

2.1 Materials

All Mg-containing compounds studied were natural abundance in ^{25}Mg (10.0%), with the exception of Mg-phthalocyanine (see prep. below), and were obtained from a variety of sources. All S-containing compounds studied were natural abundance in ^{33}S (0.75%) and also obtained from a variety of sources. The following compounds were purchased from commercial sources and used as is: Mg_3N_2 (Aldrich, 99.5+%), Mg_2Si (Aldrich, 99+%), $\text{Mg}(\text{AcAc})_2 \cdot 2\text{H}_2\text{O}$ (Aldrich, 98%), $\text{Mg}(\text{OAc})_2 \cdot 4\text{H}_2\text{O}$ (Aldrich, 98+%, A.C.S. reagent), MgWO_4 (Aldrich, 99.9%), $\text{MgHPO}_4 \cdot 3\text{H}_2\text{O}$ (Aldrich, >97%), MgCl_2 (Aldrich, Anhydrous, -10mesh, 99.99%), $\text{Mg}(\text{NO}_3)_2 \cdot 6\text{H}_2\text{O}$ (Aldrich, >98%), MgH_2 (Aldrich, hydrogen-storage grade), $\text{Mg}(\text{HCOO})_2 \cdot 2\text{H}_2\text{O}$ (Fluka, >98.0%), $\text{MgSO}_4 \cdot 6\text{H}_2\text{O}$ (Fluka, >99.0%), $\text{Mg}_3(\text{PO}_4)_2 \cdot 8\text{H}_2\text{O}$ (Fluka, >97%), MgO (Strem Chemicals, 99.5%), MgMoO_4 (Strem Chemicals, 99%), MgS (GFS Chemicals, 99.5%), $\text{MgCl}_2 \cdot 6\text{H}_2\text{O}$ (Anachemia, 99.0%), MgTiO_3 (Alfa Aesar, 99%), Li_2SO_4 (Aldrich, $\geq 98.0\%$), $(\text{NH}_4)_2\text{SO}_4$ (Aldrich, $\geq 99.0\%$), Na_2SO_4 (Aldrich, $\geq 99.0\%$), K_2SO_4 (Aldrich, $\geq 99.0\%$), Rb_2SO_4 (Aldrich, $\geq 99.0\%$), Cs_2SO_4 (Aldrich, $\geq 99\%$), CaSO_4 (Aldrich, 99%), SrSO_4 (Strem Chemicals, Reagent Grade), and BaSO_4 (Aldrich, 99%).

$\text{Mg}(\text{NH}_4)_2(\text{SO}_4)_2 \cdot 6\text{H}_2\text{O}$ was prepared by crystallization from an equimolar solution of MgSO_4 and $(\text{NH}_4)_2\text{SO}_4$ in water. Large crystals were observed after a few days. $\text{MgSO}_4 \cdot 7\text{H}_2\text{O}$ was prepared by re-crystallizing $\text{MgSO}_4 \cdot 6\text{H}_2\text{O}$ in water at 9°C for 8

weeks. $\text{Mg}(\text{OD})_2$ was prepared by hydrolyzing Mg_3N_2 with D_2O . $\beta\text{-MgSO}_4$ was obtained commercially (Aldrich, anhydrous, >99.5%) and then additionally calcined at 600°C for 24h. $\alpha\text{-MgSO}_4$ was prepared by slow evaporation of a 1M H_2SO_4 aqueous solution saturated in MgSO_4 at 250°C followed by heating at 600°C for 24h. $\alpha\text{-Mg}_2\text{V}_2\text{O}_7$, $\text{Mg}(\text{VO}_3)_2$, and $\text{Mg}_3(\text{VO}_4)_2$ were synthesized from magnesium hydroxide and ammonium metavanadate *via* a previously described method by Sam et al.¹³¹ Briefly, $\text{Mg}(\text{OH})_2$ starting material was prepared by precipitation from a solution of $\text{MgCl}_2 \cdot 6\text{H}_2\text{O}$ (0.25 M) and KOH (0.5 M, reagent grade). The suspension was washed with distilled water 3 times and then dried under vacuum at 100°C . $\alpha\text{-Mg}_2\text{V}_2\text{O}_7$: 4.005 g (34.24 mmol) NH_4VO_3 was dissolved in 50 mL of 1% NH_4OH . 2.012 g (34.50 mmol) $\text{Mg}(\text{OH})_2$ was added and then suspension was allowed to evaporate with stirring and then dried at 120°C for 24 h. The solid mixture was then calcined in air at 550°C for 30 min, 640°C for 18 h, and finally at 700°C for 23 h. The sample was ground before each heating. $\text{Mg}(\text{VO}_3)_2$: Same as above except with 5.273 g (45.08 mmol) NH_4VO_3 and 1.316 g (22.57 mmol) $\text{Mg}(\text{OH})_2$. Also, the calcination process was only at 700°C for 24 h. $\text{Mg}_3(\text{VO}_4)_2$: Same as above but with 3.426 g (29.29 mmol) NH_4VO_3 and 2.587 g (44.36 mmol) $\text{Mg}(\text{OH})_2$. As well, the calcination process was 550°C for 6 h, 635°C for 65 h, 640°C for 46 h, 750°C for 7 h and finally 800°C for 18 h. The sample was ground before each heating. Mg-phthalocyanine was prepared by heating monopyridinated aqua(magnesium) phthalocyanine (obtained as 99.1% ^{25}Mg enriched from Dr. Gang Wu, Queen's University) in vacuum at 100°C for 48h. $\text{Al}_2(\text{SO}_4)_3$ was prepared by calcining $\text{Al}_2(\text{SO}_4)_3 \cdot 18\text{H}_2\text{O}$ at 600°C for 24 h. ZnSO_4 was prepared by calcining $\text{ZnSO}_4 \cdot 6\text{H}_2\text{O}$ at 500°C for 24 h. $\text{In}_2(\text{SO}_4)_3$ was prepared as described previously by Deichman.¹³² Briefly, it was prepared by dissolving $\text{In}_2(\text{SO}_4)_3$

hydrate (Strem Chemicals) in a slight excess of sulfuric acid with gentle heating in the presence of H_2O_2 . After dissolution was complete, the solution was evaporated to dryness and the residue was heated to 500°C to obtain pure $\text{In}_2(\text{SO}_4)_3$. $\text{Ga}_2(\text{SO}_4)_3$ was prepared by heating $\text{Ga}_2(\text{SO}_4)_3 \cdot \text{H}_2\text{O}$ (Strem Chemicals) at 450°C for 48 h. Natural sample – brucite ($\text{Mg}(\text{OH})_2$), spinel (MgAl_2O_4), forsterite (Mg_2SiO_4), diopside ($\text{MgCaSi}_2\text{O}_6$), and magnesite (MgCO_3) were obtained as mineral samples from private collections. PXRD was used to confirm the purity of all compounds studied. PXRD measurements were done on a Bruker model D8 Advance diffractometer equipped with a solid-state detector model LynxEye using $\text{Cu K}\alpha$ radiation ($\lambda = 1.5406 \text{ \AA}$).

2.2 Solid-State NMR Spectroscopy

^{25}Mg SS-NMR spectra were obtained at frequencies of 55.10 MHz (static magnetic field, $B_0 = 21.1 \text{ T}$) and 24.51 MHz ($B_0 = 9.4 \text{ T}$) on Bruker Avance II and Avance consoles, respectively. At 21.1 T a homebuilt 7 mm single-channel solenoid probe (radiofrequency field $B_1 = 33 \text{ kHz}$), a homebuilt 7 mm $^1\text{H}/\text{X}$ solenoid probe ($B_1 = 28 \text{ kHz}$), a homebuilt 4 mm $^1\text{H}/\text{X}$ solenoid probe ($B_1 = 67 \text{ kHz}$), a Bruker 4 mm low- γ MAS probe ($B_1 = 46 \text{ kHz}$), a Bruker 7 mm single-channel MAS probe ($B_1 = 35 \text{ kHz}$), were used. At 9.4 T a Bruker 4 mm $^1\text{H}/\text{X}$ MAS probe ($B_1 = 44 \text{ kHz}$) and Bruker 7 mm $^1\text{H}/\text{X}$ MAS probe ($B_1 = 28 \text{ kHz}$) were used. External referencing for ^{25}Mg spectra was accomplished using a 1 M solution of MgCl_2 in water (set to 0 ppm). A non-selective solid $\pi/2$ pulse for each probe as follows: At 21.1 T – 7 mm solenoid, 2.5 μs at 4.0 dB attenuation; 4 mm MAS, 1.8 μs at 4.0 dB attenuation; 7 mm MAS, 2.4 μs at 2.0 dB

attenuation; 4 mm solenoid, 2 μ s at 7.0 dB attenuation. At 9.4 T – 4 mm MAS, 7.6 μ s at 14.0 dB attenuation; 7 mm MAS, 3.0 μ s at 4.0 dB attenuation. FIDs were collected using standard Bloch Decay, Hahn-Echo ($\pi/2$ - τ - π - τ -acq),⁹⁵ QCPMG ($\pi/2$ - τ_1 -(- τ_2 - π - τ_3 -acq)_n),¹³³ QCPMG-MAS synchronized,⁹⁹ and WURST-QCPMG^{103, 104} pulse programs. When protons were present in the sample, high-power ¹H-decoupling was used. Recycle delays ranged from 1 s to 60 s depending on the sample and complete relaxation of the signals was tested individually for each sample. Between 16 and 2000 scans were normally acquired to achieve an acceptable signal to noise ratio.

³³S SS-NMR spectra were obtained at frequencies of 69.09 MHz ($B_0 = 21.1$ T), 38.39 MHz ($B_0 = 11.8$ T) and 30.71 MHz ($B_0 = 9.4$ T) on Bruker Avance II, Avance III and Avance III consoles, respectively. At 21.1 T a homebuilt 10 mm single-channel solenoid probe (radiofrequency $B_1 = 23$ kHz), a homebuilt 7 mm single-channel solenoid probe ($B_1 = 39$ kHz), a homebuilt 7 mm ¹H/X solenoid probe ($B_1 = 36$ kHz), and a Bruker 7 mm low- γ MAS single-channel MAS probe ($B_1 = 39$ kHz) were used. At 11.8 T a homebuilt 7 mm single-channel solenoid probe ($B_1 = 25$ kHz), and a Varian 4 mm ¹H/X MAS probe ($B_1 = 27$ kHz) were used. At 9.4 T a homebuilt 10 mm ¹H/X solenoid probe ($B_1 = 30$ kHz) was used. External referencing of ³³S spectra was done using a 2 M solution of Cs₂SO₄ in water as a secondary chemical shift reference (333 ppm relative to CS₂). Another secondary chemical shift reference of trimethylene sulfoxide (TMSO) in acetone (1:1 by volume) was also used (chemical shift of 367.55 ppm). A non-selective solid $\pi/2$ pulse was calibrated for each probe as follows: At 21.1 T – 10 mm solenoid, 5.5 μ s at 4 dB attenuation; 7 mm solenoid, 3.25 μ s at 2 dB attenuation; 7 mm ¹H/X

solenoid, 3.5 μs at 2 dB attenuation; 7 mm MAS, 3.25 μs at 2 dB attenuation. At 11.8 T – 7 mm solenoid, 5 μs at 4 dB attenuation; 4 mm MAS, 4.75 μs at 6 dB attenuation. At 9.4T – 10 mm solenoid, 4.25 μs at 4 dB attenuation. FIDs were collected using standard Bloch Decay, Solid-Echo,⁹⁵ QCPMG,¹³³ QCPMG-MAS synchronized,⁹⁹ and RAPT ((χ_0 - τ_1 - χ_{180} - τ_1)_n- τ_2 -(Solid Echo or other sequence))¹⁰⁰ pulse programs. High power ¹H-decoupling was used when acquiring spectra for (NH₄)₂SO₄. Recycle delays used ranged from 5 s to 150 s depending on the sample. Between 1000 and 25000 scans were normally acquired to achieve an acceptable signal to noise ratio.

2.3 Spectral Simulations

Analytical simulations of experimental spectra were carried out with the DMFit¹³⁴, WSolids¹³⁵, and Bruker's TopSpin Lineshape Analysis Tool¹³⁶ simulation packages. For all simulations the MAS spectra were fitted first to determine the isotropic chemical shift, δ_{iso} , the quadrupolar coupling constant, C_Q , and the quadrupolar asymmetry parameter, η_Q . These values were then used to aid in the determination of the shielding interaction parameters, $\Delta\sigma_{aniso}$, η_{CSA} and the Euler angles α , β , and γ . Special attention was given to reproducing the spectral discontinuities.

2.4 Quantum Chemical Calculations

Calculation of ²⁵Mg and ³³S electric field gradient and nuclear magnetic shielding tensors were accomplished using known crystallographic data for all compounds (see

text). Plane wave-based basis set DFT calculations were performed using the NMR module of the CASTEP DFT code that employs the GIPAW algorithm¹²⁰ and is part of the Accelrys Materials Studio simulation and modeling package (Version 4.4).¹³⁷ This method is specifically designed for extended lattice structures of crystalline materials. The Perdew-Burke-Ernzerhof (PBE) functional was used with the Generalized Gradient Approximation (GGA) for all calculations.^{138, 139} On-the-fly ultra-soft pseudopotentials were used and obtained directly from Accelrys Inc. (San Diego, CA). The convergence of calculated NMR parameter on the size of a Monkhorst-Pack k -grid and a basis set cut-off energy were tested for all systems. The k -point space in Monkhorst-Pack k -grid was always smaller than 0.05 \AA^{-1} . The minimum cut-off energy used was 430 eV but the majority of compounds were run with a cut-off energy of 610 eV. Geometry optimization calculations were performed using the Broyden-Fletcher-Goldfarb-Shanno (BFGS) algorithm¹⁴⁰ and with the same functional, Monkhorst-Pack k -grid spacings and cut-off energies as in the single-point energy calculations. Convergence tolerance parameters for geometry optimization were as follows: maximum energy $2.0 \cdot 10^{-5} \text{ eV/atom}$, maximum force 0.05 eV/\AA , maximum stress 0.1 GPa and maximum displacement 0.002 \AA . Computation time ranged from 30 min to about 3 days. Computations were performed using an Intel 2.6 GHz dual core processor. The Euler angles relating the EFG tensor PAS to the CSA tensor PAS (α, β, γ) were determined using the program EFG-Shield.¹⁴¹

3. ^{25}Mg in Mg-Containing Materials

As mentioned previously, ^{25}Mg is a low natural abundance, low magnetogyric ratio, quadrupolar ($I = 5/2$) nucleus. As such, ^{25}Mg SS-NMR is not trivial and the number of reports on ^{25}Mg SS-NMR are quite few. So, the goal of this study was to explore the limits of ^{25}Mg SS-NMR at Ultrahigh magnetic field of 21.1T ($\nu_0(^{25}\text{Mg}) = 55.1$ MHz) and to evaluate the accuracy and reliability of first principles calculations using the CASTEP package. As well, the relationship between structural and ^{25}Mg SS-NMR parameters was examined for the various compounds studied. Lastly, an effort to correlate calculated NMR parameters to experimentally determined parameters was attempted. A total of 29 Mg-containing compounds were examined in this study, attempting to cover a wide variety of interesting coordinating environments for magnesium.

3.1 Structural Details of Systems Studied

The exact compounds under study for this part of this work have already been mentioned in Table 1. However, Table 3 shows more pertinent structural data available for these compounds. Given the large number of compounds studied, only the most relevant data from the most recent crystal structure is shown here. More information can be found in the .cif files in Appendix B.

Table 3 – Structural details of magnesium compounds studied.

Compound	Site	Site Ratio	Space Group	Cell	Mg site Point Group	Struc. Ref.
MgO	1	-	<i>Fm-3m</i>	Cubic	O _h	142
Brucite, Mg(OH) ₂ /Mg(OD) ₂	1	-	<i>P-3m1</i>	Hexagonal	D _{3d}	143
MgSO ₄ ·6H ₂ O	1 2	1:1	<i>C2/c</i>	Monoclinic	C _i C ₂	144
MgSO ₄ ·7H ₂ O	1	-	<i>P2₁2₁2₁</i>	Orthorhombic	C ₁	145
Mg(NH ₄) ₂ (SO ₄) ₂ ·6H ₂ O	1	-	<i>P2₁/a</i>	Monoclinic	C _i	146
Mg(NO ₃) ₂ ·6H ₂ O	1	-	<i>P2₁/c</i>	Monoclinic	C _i	147
MgCl ₂ ·6H ₂ O	1	-	<i>C2/m</i>	Monoclinic	C _{2h}	148
Mg ₃ (PO ₄) ₂ ·8H ₂ O	1 2	2:1	<i>C2/m</i>	Monoclinic	C _{2h} C ₂	149
MgHPO ₄ ·3H ₂ O	1	-	<i>Pbca</i>	Orthorhombic	C ₁	150
Forsterite, Mg ₂ SiO ₄	1 2	1:1	<i>Cmcm</i>	Orthorhombic	C _i C _s	43
MgMoO ₄	1 2	1:1	<i>C2/m</i>	Monoclinic	C _s C ₂	151
MgWO ₄	1	-	<i>P2/c</i>	Monoclinic	C ₂	152
α-Mg ₂ V ₂ O ₇	1	-	<i>P2₁/c</i>	Monoclinic	C ₁	153
Mg(VO ₃) ₂	1	-	<i>C2/m</i>	Monoclinic	C _{2h}	43
Mg ₃ (VO ₄) ₂	1 2	2:1	<i>Cmca</i>	Orthorhombic	C _{2h} C ₂	154
Geikielite, MgTiO ₃	1	-	<i>R-3</i>	Hexagonal	C ₃	155
Magnesite, MgCO ₃	1	-	<i>R-3c</i>	Hexagonal	S ₆	156
Spinel, MgAl ₂ O ₄	1	-	<i>Fd3m</i>	Cubic	T _d	157
Åkermanite, Ca ₂ MgSi ₂ O ₇	1	-	<i>P-42₁m</i>	Tetragonal	S ₄	158
α-MgSO ₄	1	-	<i>Cmcm</i>	Orthorhombic	C _{2h}	60
β-MgSO ₄	1	-	<i>Pnma</i>	Orthorhombic	C _i	60
Mg(HCOO) ₂ ·2H ₂ O	1 2	1:1	<i>P2₁/c</i>	Monoclinic	C _i C _i	43
Mg(AcAc) ₂ ·2H ₂ O	1	-	<i>P2₁/c</i>	Monoclinic	C _i	159
Mg(OAc) ₂ ·4H ₂ O	1	-	<i>P2₁/c</i>	Monoclinic	C _i	160
MgS	1	-	<i>Fm-3m</i>	Cubic	O _h	43
MgH ₂	1	-	<i>P4₂/mn m</i>	Tetragonal	D _{2h}	161
MgCl ₂	1	-	<i>R-3m</i>	Hexagonal	D _{3d}	162
Mg ₃ N ₂	1	-	<i>Ia-3</i>	Cubic	C ₁	43
Mg ₂ Si	1	-	<i>Fm3m</i>	Cubic	T _d	163
Mg-phthalocyanine	1	-	<i>P2₁/c</i>	Monoclinic	C _i	164

As can be seen in Table 3, there are a large variety of structural systems under study. An attempt was made in this study to cover a broad range of different magnesium site symmetries and overall crystal structures to establish the ^{25}Mg NMR parameters one might expect from these systems. The majority of these compounds have only one crystallographically unique magnesium site, however, there are a few where two unique sites exist in various ratios. As will be shown, for the systems where multiple Mg sites are present, ^{25}Mg SS-NMR was able to resolve these sites and extraction of reliable NMR parameters was accomplished. As well, the symmetry environment that magnesium is present in in these compounds varies considerably. The majority of the compounds have magnesium in an octahedrally coordinated site, in some cases (eg. MgS and MgO) it is a perfectly cubic environment. However, as will be shown, some very interesting results were obtained for compounds with magnesium present in a tetrahedrally coordinating environment (eg. Mg_3N_2 , Spinel). And, as an interesting and potentially biologically relevant study, ^{25}Mg SS-NMR was carried out on the seemingly uncommon, planar, chelating compound Mg-phthalocyanine. The structural and NMR-related results will be discussed for these systems in more detail in the following sections.

3.2 Determination of ^{25}Mg NMR Parameters

Figures 13 – 23 and A1 – A11 show representative natural abundance ^{25}Mg SS-NMR spectra for the magnesium-containing compounds studied. Only the central transition is observed in all cases shown, both under MAS and as stationary samples. The QCPMG sequence was used in some cases to improve the signal to noise where the

quadrupolar coupling constant was large (> 5 MHz). All spectra shown were taken at 21.1 T. Spectra were also taken at 9.4 T ($\nu_0(^{25}\text{Mg}) = 24.5$ MHz) (not shown) for a few of the compounds with small quadrupolar interactions to improve the accuracy in detection of the quadrupolar parameters. It should be noted that although quantitative spin-lattice relaxation, T_1 , times were not determined, qualitatively the T_1 values for ^{25}Mg in the majority of the samples is quite long, ranging from approximately 1 to 20 s. Many of the previous ^{25}Mg SS-NMR studies acquired spectra with tens to hundreds of thousands of transients and very short inter-acquisition delays. Conversely, in this work the majority of spectra are obtained with less than 1000 transients but with inter-acquisition delays of 5-60 s giving more efficiently and reliably obtained high signal to noise ^{25}Mg spectra.

Unlike the ^{33}S work discussed in the next section, the compounds studied for ^{25}Mg SS-NMR will be separated into two main groups: Magnesium compounds with magnesium in an oxygen-coordinating environment and magnesium in a non-oxygen coordinating environment. This is not to suggest that all compounds with Mg in an oxygen-coordinating environment are identical in terms of NMR parameters, but is done merely to impose a partition for the large number of materials studied. Though, as will be shown, there are similarities in NMR parameters when Mg is in similar coordinating environments. For example, Mg compounds with water in the first coordination sphere show a very narrow window of isotropic chemical shifts.

Table 4 summarizes the experimental data and the results of the corresponding first principles calculations. The calculated quadrupolar coupling constants, C_Q , and

asymmetry parameter, η_Q , can be directly compared with experimentally determined values. However, the first principles calculations provide the absolute shielding, σ , of a given compound instead of the experimentally measured chemical shift, δ , which is measured in reference to a common standard (for ^{25}Mg $\delta_{\text{iso}} = 0$ ppm for 1 M MgNO_3 in water). As mentioned previously, the determination of the absolute shielding of a given material is difficult and so typically the calculated isotropic shielding and the experimental isotropic shift are correlated and if the calculations are reliable and accurate a linear relationship exists. This relationship is shown in the next section. For a very good theoretical model the correlation should be unity, or 1:1, and should provide the position of the reference on the absolute isotropic shielding scale.

Table 4 – Experimental and calculated ^{25}Mg NMR parameters for all compounds studied.

Compound	Site	Experimental ^{25}Mg NMR			Calculated ^{25}Mg parameters (CASTEP)					η_Q^a
		δ_{iso} , (ppm)	C_Q , (MHz)	η_Q^a	σ_{iso}^{calc} , (ppm)	δ_{iso}^{calc} , (ppm) ^b	$\Delta\sigma_{aniso}^{calc}$, (ppm) ^c	η_{CSA}	C_Q^d , (MHz)	
MgO	1	26.26 ±0.05	0.0	N/A	535.00	31.1	0.01	0.00	~0	0.80
Brucite, Mg(OH) ₂	1	11.8 ±0.2	3.09 ±0.01	0.00 ±0.01	550.75	15.3	-13.02	0.01	-2.79	0.00
MgSO ₄ x6H ₂ O	1	1.0 ±0.1	0.0	N/A	557.27	8.8	11.27	0.98	3.46	0.97
	2	1.2 ±0.2	2.15 ±0.03	0.40 ±0.02	551.53	14.5	5.53	0.14	1.90	0.95
MgSO ₄ x7H ₂ O	1	1.6 ±0.1	1.80 ±0.01	0.20 ±0.02	559.14	6.9	-5.43	0.89	2.84	0.97
Mg(NH ₄) ₂ (SO ₄) ₂ x6H ₂ O	1	4.0 ±0.5	2.61 ±0.02	0.61 ±0.02	557.26	8.8	8.48	0.59	-3.84	0.49
MgCl ₂ x6H ₂ O	1	-0.16 ±0.03	0.0	N/A	561.00	5.06	-3.03	0.21	0.82	0.04
Mg ₃ (PO ₄) ₂ x8H ₂ O	1	1.5 ±0.2	1.41 ±0.01	0.52 ±0.03	564.96	1.1	6.08	0.11	1.88 [3.40]	0.15
	2	7.7 ±1.5	6.55 ±0.10	0.00 ±0.10	561.45	4.6	31.44	0.07	-12.53 [-4.01]	0.01
MgHPO ₄ x3H ₂ O	1	-6.3 ±0.2	2.49 ±0.10	0.05 ±0.05	572.10	-6.0	-5.65	0.68	2.67	0.25
Mg(NO ₃) ₂ x6H ₂ O	1	0.18 ±0.05	1.49 ±0.02	0.00 ±0.05	562.40	3.7	-4.82	0.52	-2.37 [-2.42]	0.62
Forsterite, Mg ₂ SiO ₄	1	14.5 ±1.0	5.10 ±0.03	0.97 ±0.02	549.49	16.6	-19.29	0.64	-5.15	0.96
	2	2.4 ±1.0	4.17 ±0.04	0.40 ±0.02	561.73	4.3	-5.89	0.33	5.53	0.10
MgMoO ₄	1	-10.6 ±0.3	2.36 ±0.04	1.00 ±0.03	578.78	-12.7	8.67	0.29	2.95	0.81
	2	-8.3 ±0.3	4.29 ±0.02	0.21 ±0.02	576.82	-10.8	-9.01	0.93	4.85	0.12
MgWO ₄	1	-1.7 ±0.1	2.20 ±0.01	1.00 ±0.02	573.32	-7.3	7.07	0.21	-2.07	0.55
	1	2.8 ±0.2	2.13 ±0.02	0.88 ±0.02	567.26	-1.2	10.21	0.96	2.87	0.79
α -Mg ₂ V ₂ O ₇	2	-4.4 ±0.3	2.44 ±0.02	0.74 ±0.01	574.01	-8.0	-10.72	0.97	-4.42	0.16
Mg(VO ₃) ₂	1	-8.7 ±4.0	8.85 ±0.10	0.97 ±0.02	580.84	-14.8	-13.96	0.83	-13.15	0.38
	1	7.1 ±0.3	2.94 ±0.02	0.36 ±0.02	561.53	4.5	14.70	0.84	2.51	0.48
Mg ₃ (VO ₄) ₂	2	13.1 ±3.0	8.16 ±0.05	0.20 ±0.03	566.48	-0.4	28.46	0.45	8.47	0.99
	1	9.9 ±0.1	1.82 ±0.02	0.10 ±0.04	559.29	6.8	-7.84	0.00	1.79	0.00
Pervoskite, MgTiO ₃	1	-3.8 ±0.2	2.24 ±0.02	0.04 ±0.02	569.11	-3.1	-2.17	0.00	-3.56 [-3.38]	0.00
Magnesite, MgCO ₃	1	48.2 ±1.0	0.0	N/A	504.85	61.2	-0.04	0.00	~0	0.79
Spinel, MgAl ₂ O ₄	1	-8.1 ±1.0	7.41 ±0.05	0.35 ±0.02	577.30	-11.2	18.80	0.37	9.36 [8.89]	0.39
α -MgSO ₄	1	0.2 ±3.0	10.4 ±0.1	1.00 ±0.02	579.59	-13.5	28.50	0.68	12.00 [12.15]	0.95
β -MgSO ₄	1	-0.6 ±0.3	2.34 ±0.05	0.81 ±0.04	564.51	1.6	6.74	0.60	3.63	0.56
Mg(HCOO) ₂ x2H ₂ O	2	-3.9 ±0.3	3.52 ±0.03	0.23 ±0.04	561.33	4.7	11.71	0.85	4.33	0.47

Experimental ^{25}Mg NMR			Calculated ^{25}Mg parameters (CASTEP)							
Compound	Site	δ_{iso} (ppm)	C_Q (MHz)	η_Q^a	σ_{iso}^{calc} (ppm)	δ_{iso}^{calc} (ppm)	$\Delta\sigma_{aniso}^b$ (ppm)	η_{CSA}^c	C_Q^d [MHz]	η_Q^a
Mg(AcAc) $_2$ x2H $_2$ O	1	2.7 \pm 4.0	7.2 \pm 0.1	0.96 \pm 0.02	560.60	5.5	20.33	0.63	10.18 [9.72] ^f	0.77
Mg(OAc) $_2$ x4H $_2$ O	1	4.1 \pm 0.3	2.53 \pm 0.02	0.75 \pm 0.03	559.49	6.6	-19.12	0.76	-5.15	0.89
MgS	1	-1.11 \pm 0.02	0.0	N/A	568.34	-2.3	-0.06	0.00	-0	0.81
MgH $_2$	1	10.3 \pm 1.0	3.06 \pm 0.02	0.89 \pm 0.05	554.07	12.0	-13.71	0.86	-1.49 [-2.18] ^f	0.66
MgCl $_2$	1	2.3 \pm 0.1	1.62 \pm 0.02	0.00 \pm 0.05	558.58	7.5	-6.41	0.00	-1.70	0.00
Mg $_3$ N $_2$	1	101.0 \pm 2.0	9.30 \pm 0.05	0.44 \pm 0.01	465.13	100.9	40.84	0.14	-9.74	0.37
Mg $_2$ Si	1	61.7 \pm 0.1	0.0	N/A	504.07	62.0	0.00	N/A	0.00	N/A
MgCp $_2$ (See ref. ²³)	1	-91 \pm 3	5.80 \pm 0.05	0.01 \pm 0.01	669.64	-103.6	53.74	0.25	-6.10	0.10
Mg-phthalocyanine	1	-	26.9 \pm 0.5	0.0 \pm 0.1	523.79	42.27	68.94	0.13	39.4	0.08

^a η_Q defined as: $|V_{11} - V_{22}|/N_{33}$. ^b δ_{iso}^{calc} obtained as $\delta_{iso} = -(\sigma_{iso} - \sigma_{ref})$ with $\sigma_{ref} = 566.06$ ppm from the intercept in Figure 11

^cChemical shielding anisotropy $\Delta\sigma_{aniso}$ from CASTEP is defined as $\Delta\sigma_{aniso} = \sigma_{33} - (\sigma_{11} + \sigma_{22})/2$. ^dAsymmetry parameter η_{CSA} in CASTEP is defined as $\eta = (\sigma_{22} - \sigma_{11})/(\sigma_{33} - \sigma_{iso})$. Principle components of the symmetric shielding tensor ordered as: $|\sigma_{33} - \sigma_{iso}| \geq |\sigma_{11} - \sigma_{iso}| \geq |\sigma_{22} - \sigma_{iso}|$. ^e C_Q calculated for optimized structure. ^fOnly positions of protons were optimized.

3.3 Structural Correlation of the Shielding Interaction

Figure 11 shows the linear correlation between the calculated isotropic shielding and the experimental isotropic chemical shift for all the compounds examined in this work. It can be seen that a correlation of $\sigma_{iso} = -1.072 (\pm 0.036) \cdot \delta_{iso} + 566.06 (\pm 0.99)$ with a regression factor of 0.9626 was obtained. Such a high quality linear relationship observed for a broad range of chemical shifts together with a deviation from unity by less than 8% gives a good indication of the reliability of CASTEP-calculated shielding constants.

From Table 4 and Figure 11 it can be seen that the observed chemical shift range for ^{25}Mg is quite moderate extending from about -100 ppm to +100 ppm where the majority of the compounds are concentrated within approximately -10 ppm to 15 ppm. It is interesting to note that tetrahedral-coordinated Mg environments show a much larger chemical shift range than the octahedrally-coordinated Mg environments. Octahedral environments are mostly concentrated within the -10 ppm to 15 ppm range whereas tetrahedral Mg sites are more deshielded with 101 ppm for Mg_3N_2 being the most deshielded site in all studied compounds.

Another interesting finding that arose from the calculations performed was the seemingly minute contribution of the chemical shielding anisotropy, $\Delta\sigma_{aniso}$. As shown in Table 4 the calculated quadrupolar interactions dominate the calculated shielding anisotropy for the majority of the Mg compounds studied. This was confirmed

experimentally and only for a very limited number of materials was a measurable CSA detected. For this reason, the experimental CSA is not listed in Table 1, and discussed separately for the cases where the interaction produced a distinctly observable effect in the spectrum.

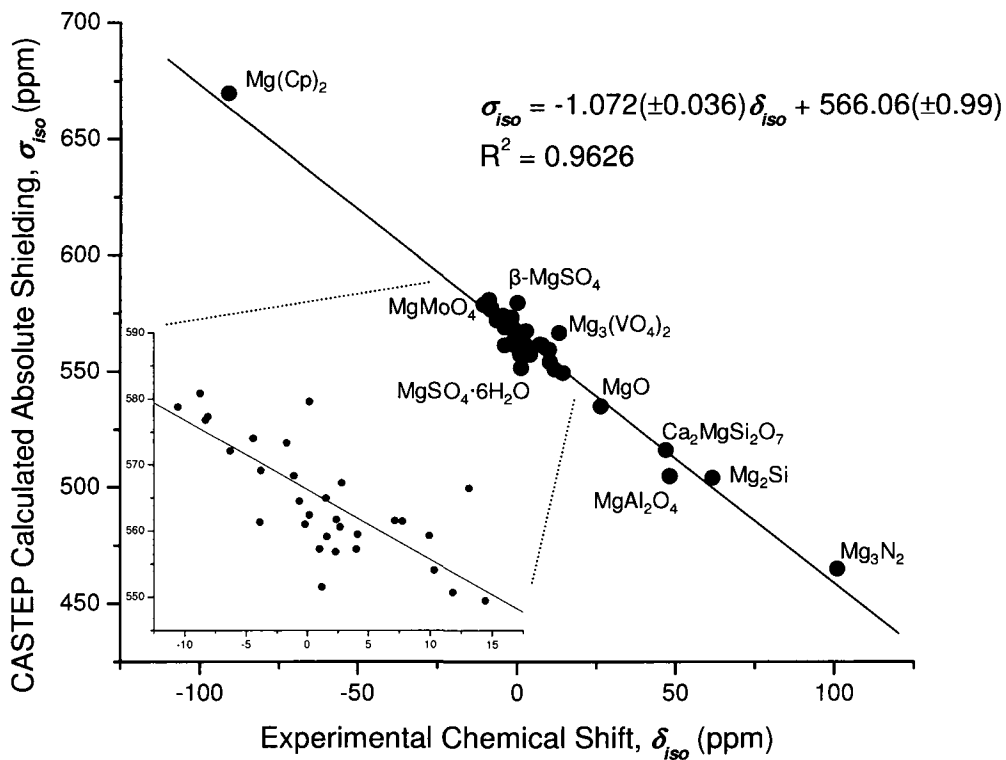


Figure 11 – Correlation between ^{25}Mg experimentally determined chemical shift and calculated absolute shielding as determined by CASTEP for all 28 Mg compounds studied. Line of best fit is shown. The inset shows enlarged portion of correlation where most compounds are found.

Table 5 – Experimental and calculated ^{25}Mg CSA parameters for Mg compounds studied with an observable interaction.

Compound	CSA Parameters			Euler Angles		
	δ_{iso} [σ_{iso}^{calc}] (ppm)	$-\Delta\delta_{aniso}^b$ [$\Delta\sigma_{aniso}$], (ppm)	$\eta_{CSA}[\eta]$	α , (°)	β , (°)	γ , (°)
Brucite, $\text{Mg}(\text{OH})_2$	11.82 \pm 0.20	-15.75 \pm 3.00	0.0 \pm 0.2	0 ^a	0 \pm 5	0 ^a
CASTEP calculations	15.3 [550.75]	[-13.01]	[0.01]	120	90	180
Mg_3N_2	101.0 \pm 2.0	42.0 \pm 6.0	0.7 \pm 0.2	150	10	164
CASTEP calculations	100.9 [465.13]	[40.84]	[0.14]	\pm 30	\pm 10	\pm 30
α - MgSO_4	-8.1 \pm 1.0	25.5 \pm 3.0	0.40 \pm 0.2	235	2	235
CASTEP calculations	-11.2 [577.30]	[18.80]	[0.37]	90 \pm 5	0 \pm 5	0 \pm 5

^a Arbitrarily set to 0 since it did not affect the lineshape ^b The sign of the chemical shielding anisotropy $\Delta\sigma_{aniso}$ from CASTEP is opposite to the experimental CSA $\Delta\delta_{aniso}$.

3.4 Structural Correlation of the Quadrupolar Interaction

Figure 12 shows the linear correlation between the calculated quadrupolar coupling constant and the experimentally determined constant for all compounds studied in this work. It can be seen that a correlation of $C_Q^{calc} = 1.316 (\pm 0.041) C_Q$ with a regression factor of 0.945 was obtained. This deviation from unity of about 34% shows that generally calculated quadrupolar coupling constants were much larger and thus overestimated from the experimentally determined values.

There are several possible explanations for why the majority of the calculated C_Q 's for ^{25}Mg are larger than what is observed experimentally. One possible explanation is that the possible contribution of thermal motion of the atoms in the crystal lattice. This thermal motion may, in fact, contribute to the electric field gradients within a lattice and CASTEP single-point energy calculations do not account for this possible motion. All

calculations are done with the assumption of rigid structures with the atoms fixed in their crystallographic coordinates. The NMR experiments, however, are performed at a temperature where molecular motion is undoubtedly present. In principle, it is possible to take into account molecular motion, but this is expected to be extremely computationally demanding. An excellent discussion by Harris et al.¹⁶⁵ shows the limitations of this computational technique for determining shielding parameters on a crystallographic basis with various sources of uncertainty. It is possible that for many of the compounds studied the water molecules are more mobile than the crystal structure would lead one to expect. In fact, a few interesting ^2H NMR studies have shown that water is quite mobile in hydrated salt compounds. Studies of $\text{CaCl}_2 \cdot x\text{H}_2\text{O}$ ($x = 2, 4, 6$)¹⁶⁶ and $\text{CuSO}_4 \cdot 5\text{H}_2\text{O}$ ¹⁶⁷ have shown that at room temperature water is in motion: either rotating, performing a reorientation or changing positions on a time scale that is, at least, shorter than the time scale of the measurable NMR interactions at the nucleus. This extra mobility may cause an observed averaging of these interactions at the ^{25}Mg nucleus and could, therefore, account for deviations from calculated and experimental EFG parameters. As a model example, the compound $\text{Mg}(\text{NO}_3)_2 \cdot 6\text{H}_2\text{O}$ has one crystallographically unique Mg site with an experimental $C_Q = 1.49 \pm 0.02$ MHz and $\eta_Q = 0.00 \pm 0.05$ while the calculated $C_Q^{\text{calc}} = -2.37$ MHz with $\eta_Q^{\text{calc}} = 0.62$. $\text{Mg}(\text{NO}_3)_2 \cdot 6\text{H}_2\text{O}$ crystallizes in a $P2_1/c$ space group (Table 3) where the Mg is in an octahedral environment completely coordinated by water molecules with only C_i point group symmetry if the water molecules are kept rigid. If, however, the water is allowed to be more mobile then the Mg centre is located on an axis which approximates C_4 symmetry. This would lend itself to an axially symmetric EFG tensor with $\eta_Q = 0$ instead of the $\eta_Q^{\text{calc}} = 0.62$. The effect of motion can be tested by

carrying out variable temperature experiments. However, this is outside the scope of this work and so these experiments were not performed.

As mentioned, another source of error in the calculated NMR parameters may arise from inaccuracies in the reported crystal structure used in the calculations. This effect is examined in the ^{33}S part of this work in the following sections. For instance, the coordinates of hydrogen atoms from XRD data are, in general, less reliable than for other atoms. A possible method for improving the agreement is to perform a geometry optimization for the positions of all atoms in the lattice or of just the protons while leaving other atoms in the lattice fixed. To illustrate the success of this technique, O'Dell and Schurko have shown that proton-optimized CASTEP calculations can provide a more accurate prediction for η_Q in the study of ^{14}N in some crystalline amino acids.¹⁶⁸ Due to time limitations no systematic tests were carried out in this work and such optimizations were performed only for several selected compounds, namely $\text{Mg}_3(\text{PO}_4)_2 \cdot 8\text{H}_2\text{O}$, $\text{Mg}(\text{NO}_3)_2 \cdot 6\text{H}_2\text{O}$, MgH_2 , $\alpha\text{-MgSO}_4$, $\beta\text{-MgSO}_4$, $\text{Mg}(\text{AcAc})_2 \cdot 2\text{H}_2\text{O}$, åkermanite and MgCO_3 . Although in some cases there is a little improvement in the calculated ^{25}Mg NMR parameters (Table 4), generally no significant improvement in agreement with the experiment was observed.

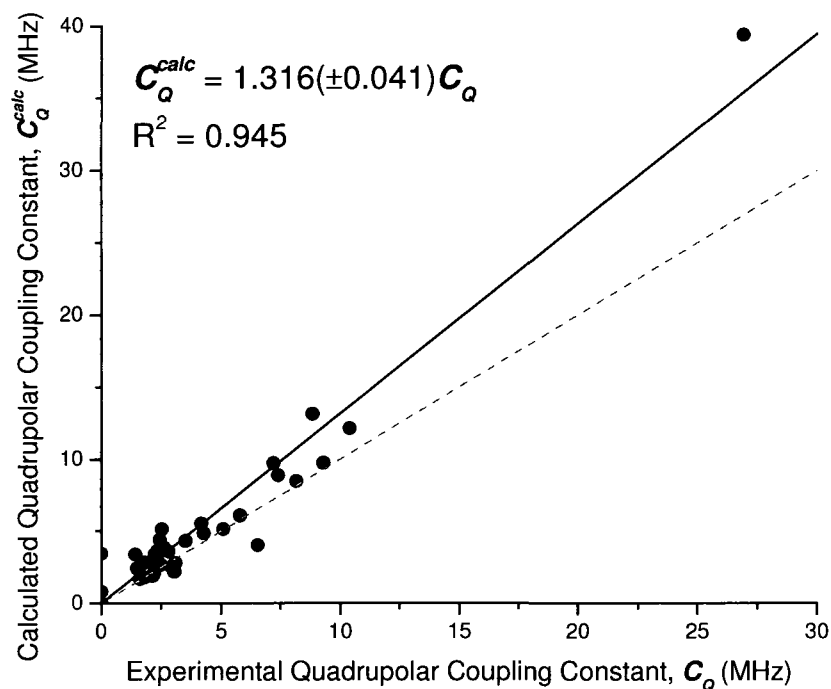


Figure 12 - Correlation between ^{25}Mg experimentally determined quadrupolar coupling constant, C_Q , and the calculated quadrupolar coupling constant, C_Q^{calc} , as determined by CASTEP for all 29 Mg compounds studied. Line of best fit is shown as the solid line. The dashed line shows a perfect 1:1 correlation.

3.5 Mg in O-coordinating Environments

The simplest Mg compound in an oxygen-coordinated environment is MgO. This material has been studied previously^{12, 18, 169} and has a reported isotropic chemical shift range of $\delta_{iso} = 25\text{-}26.5$ ppm. These differences in isotropic chemical shift, though slight, may have arisen from variations in the concentration of Mg^{2+} in the external reference or possible impurities in the samples. A $\delta_{iso} = 26.26 \pm 0.05$ ppm for MgO was obtained in this study (Figure A1 in Appendix A) and calculations gave an absolute shielding of $\sigma_{iso} = 535.00$ ppm which correlates well to the experimental value. MgO is a cubic system

(Table 4) thus the quadrupolar interaction for ^{25}Mg is zero in this case. Another seemingly simple oxygen-coordinating Mg compound is brucite, of $\text{Mg}(\text{OH})_2$. This compound has been shown to have $\delta_{iso} = 11.82 \pm 0.20$ ppm both for the natural mineral and the deuterated $\text{Mg}(\text{OD})_2$ (Figure 13). The static spectra for both $\text{Mg}(\text{OH})_2$ (not shown) and $\text{Mg}(\text{OD})_2$ are identical, indicating that the contribution of proton dipolar coupling is very small. The calculated shielding constant for brucite ($\sigma_{iso} = 550.75$ ppm) is about 16 ppm higher than that of MgO ($\sigma_{iso} = 535.00$ ppm), which is in excellent agreement with the experimental difference in the chemical shifts of 14.59 ppm. The isotropic chemical shift for $\text{Mg}(\text{OH})_2$ has been previously reported with slightly differing values of 10 ± 50 ppm,¹⁶⁹ 13.5 ppm,¹⁷⁰ and 14.1 ppm.¹² While reported values vary, the shift reported in this work matches well with Bastow's single-crystal SS-NMR study.¹⁷⁰ According to the structural data (Table 3), Mg in $\text{Mg}(\text{OH})_2$ is found in a distorted octahedral environment ($P-3m$ space group) with a D_{3d} point group symmetry. A nucleus present in a D_{3d} point group site symmetry will only have two independent eigenvalues for the symmetric part of the magnetic shielding tensor, which would imply an axially symmetric tensor.^{171, 172} Similarly, the presence of this C_3 proper rotation axis at the Mg site would imply an axially symmetric EFG tensor as well.^{1, 173} This is exactly what was observed for $\text{Mg}(\text{OH})_2$ with a quadrupolar coupling constant, $C_Q = 3.09 \pm 0.01$ MHz and asymmetry parameter $\eta_Q = 0.00$. Bastow, in fact, performed a single-crystal SS-NMR study of $\text{Mg}(\text{OH})_2$ ¹⁷⁰ and determined C_Q to be 3.056 ± 0.005 MHz, which is very close to the value determined in this work. The spectrum of the deuterated material, $\text{Mg}(\text{OD})_2$, has very little broadening due to dipolar coupling and its stationary spectrum is well defined (Figure 13). Therefore, this is one of only a few compounds in which the

contribution of the CSA is large enough to be extracted reliably. Given the axially symmetric nature of the tensors, the tensor orientations are restricted such that one of the eigenvectors corresponding to the unique eigenvalues of the corresponding tensors must be oriented along the C_3 rotation axis. This means that the commonly defined Euler angle⁸³, β , made between the largest component of the shielding tensor, σ_{33} , and the principal component of the EFG tensor, V_{33} , must be either 0° or 90° . As such, the anisotropy parameters extracted from the stationary spectrum for brucite were found to be $\Delta\sigma_{aniso} = -15.75 \pm 3.00$ ppm with asymmetry $\eta_{CSA} = 0.0 \pm 0.1$ and the Euler angle $\beta = 0.0 \pm 5.0^\circ$, as expected (Table 5). The calculated CSA was found to be quite similar to experiment, although, the calculated value for β was 90° where experimentally it was determined to be 0° (Figure 13).

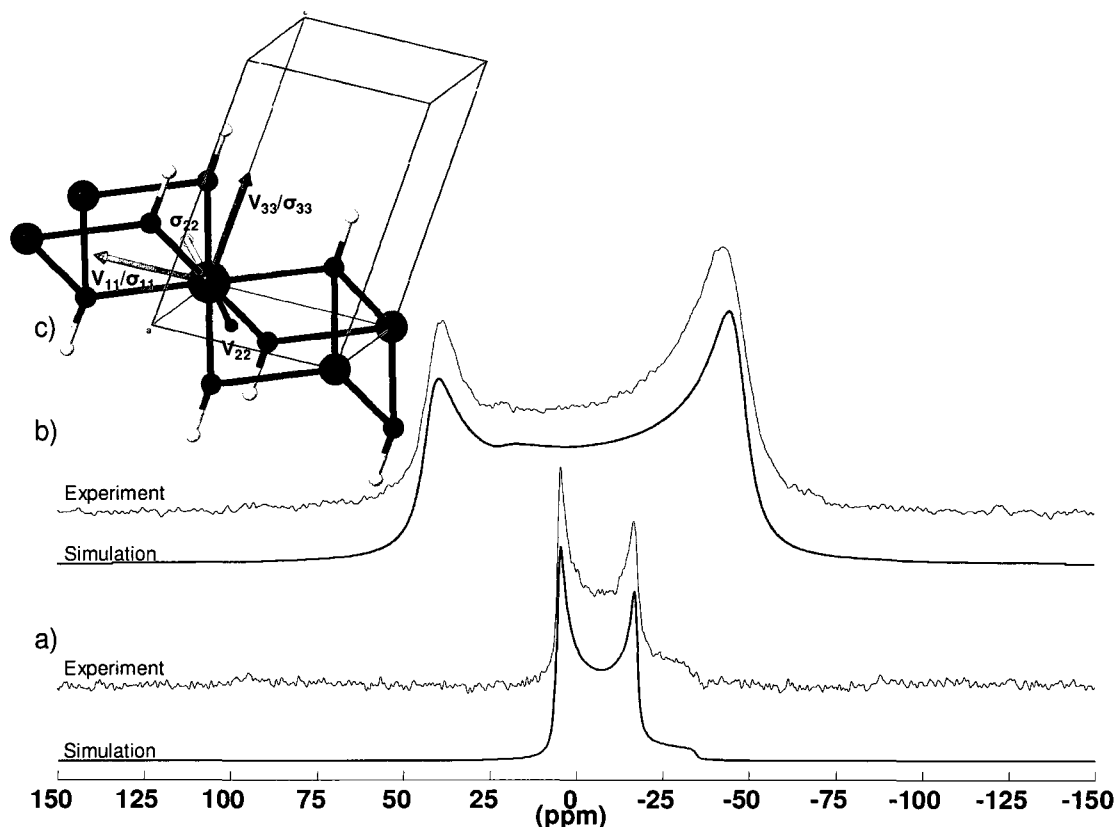


Figure 13 – a) 10 kHz MAS ^{25}Mg SS-NMR spectrum of brucite ($\text{Mg}(\text{OH})_2$). b) Static Bloch decay ^{25}Mg SS-NMR spectrum of $\text{Mg}(\text{OD})_2$. c) Representative portion of the brucite unit cell showing the one crystalline Mg site in the lattice. Calculated CSA and EFG tensor orientations are shown for one Mg atom. Note that V_{33} and σ_{33} point in the direction of the C_3 rotation axis and Euler angle $\beta = 90^\circ$ ($\beta = 0^\circ$ was determined experimentally (Table 5)).

The next series of compounds studied represents those where water molecules exist in the first coordination sphere around Mg. This includes: $\text{MgSO}_4 \cdot 6\text{H}_2\text{O}$, $\text{MgSO}_4 \cdot 7\text{H}_2\text{O}$, $\text{Mg}(\text{NH}_4)_2(\text{SO}_4)_2 \cdot 6\text{H}_2\text{O}$, $\text{MgCl}_2 \cdot 6\text{H}_2\text{O}$, $\text{Mg}_3(\text{PO}_4)_2 \cdot 8\text{H}_2\text{O}$, $\text{MgHPO}_4 \cdot 3\text{H}_2\text{O}$, and $\text{Mg}(\text{NO}_3)_2 \cdot 6\text{H}_2\text{O}$ (Figures 14, 15, A2, A3). The chemical shift range for these compounds is quite small ($-6.3 \text{ ppm} \leq \delta_{iso} \leq 7.7 \text{ ppm}$) (Table 4). In fact, when the coordination sphere of the Mg ion is completely filled with water molecules (*i.e.* $\text{MgCl}_2 \cdot 6\text{H}_2\text{O}$, $\text{Mg}(\text{NO}_3)_2 \cdot 6\text{H}_2\text{O}$, $\text{MgSO}_4 \cdot 6\text{H}_2\text{O}$, $\text{MgSO}_4 \cdot 7\text{H}_2\text{O}$) the isotropic chemical shift is very close to 0 ppm, which is the aqueous Mg^{2+} ion reference (Figure 14). In all of

these compounds the molecules of water seem to completely shelter the Mg ions from other shielding contributions. In situations where some other ligands coordinate to Mg in addition to water, there appears to be some influence on the shielding at the Mg nucleus from these additional ligands. These compounds are $\text{MgHPO}_4 \cdot 3\text{H}_2\text{O}$ and $\text{Mg}_3(\text{PO}_4)_2 \cdot 8\text{H}_2\text{O}$ (Figure 15), where the effect on the shielding is on the order of several ppm. The agreement between experimental chemical shift and calculated shielding is quite acceptable (Table 4). The very small range of isotropic chemical shifts in this group of materials demonstrates clearly the dominant effect of the first-coordination sphere surrounding Mg on the shielding interaction felt at the nucleus and is not as much influenced by the other cations or anions present in higher order coordination spheres.

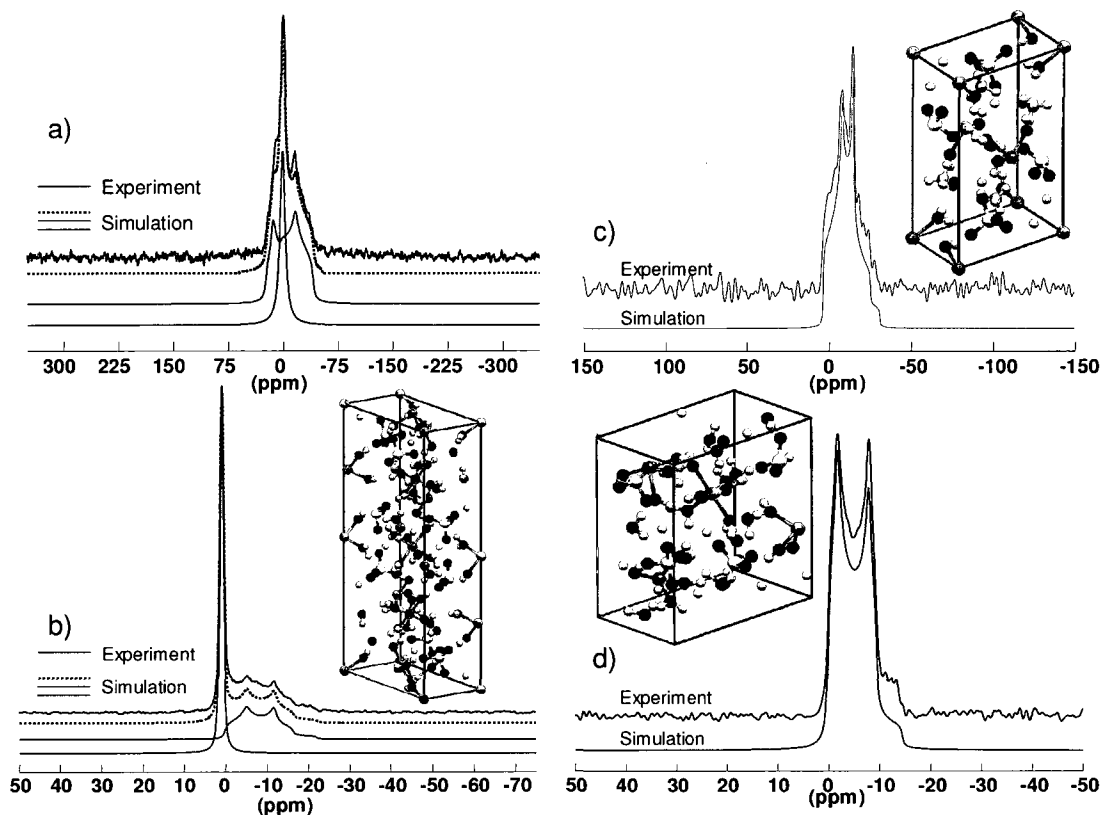


Figure 14 – ^{25}Mg SS-NMR spectra (experimental and simulated) of a) $\text{MgSO}_4 \cdot 6\text{H}_2\text{O}$ - Static Hahn Echo. b) $\text{MgSO}_4 \cdot 6\text{H}_2\text{O}$ – 5 kHz MAS Bloch Decay. Unit cell shown with Mg atoms in green. c) $\text{Mg}(\text{NH}_4)_2(\text{SO}_4)_2 \cdot 6\text{H}_2\text{O}$ – 5 kHz MAS Bloch Decay. Unit cell shown. d) $\text{MgSO}_4 \cdot 7\text{H}_2\text{O}$ – 5 kHz MAS Bloch Decay. Unit cell shown.

The quadrupolar interaction parameters, however, vary substantially for these compounds, ranging from $C_Q = 0.0$ MHz for $\text{MgCl}_2 \cdot 6\text{H}_2\text{O}$ to $C_Q = 6.55 \pm 0.10$ MHz ($\eta_Q = 0.0 \pm 0.1$) for one of the two sites in $\text{Mg}_3(\text{PO}_4)_2 \cdot 8\text{H}_2\text{O}$. This may be explained by noting the variation in the other polyatomic ions present in the crystal lattice. It is clear that other species present in higher order coordination spheres affects the electric field gradient felt at the Mg nucleus. The agreement between calculated and experimental EFG parameters for these compounds ranges from very good, with a variance of about 6%, to fair with the calculated C_Q being about half the experimental value. Most likely, as mentioned earlier, the discrepancy arises from the inaccuracies in the crystal structure

data used in the calculations. This is well illustrated by a case of anhydrous MgCl_2 , where use of a more recently reported crystal structure¹⁶², resulted in a dramatic improvement in the agreement between the calculated and experimental C_Q . With the more recent structure the $C_Q^{calc} = 1.70$ MHz, only 5% above the experimental value. The older structure¹⁷⁴, however, produced a $C_Q^{calc} = 2.53$ MHz, about 56% above the experimental value. It is interesting, though, that both structures produced very similar isotropic shielding values (σ_{iso} (via ¹⁷⁴) = 556.83 ppm versus σ_{iso} (via ¹⁶²) = 558.58 ppm). This example highlights very clearly the importance of an accurate crystal structure for these first principles calculation methods. These effects are examined in the second half of this work (see section 4). Nevertheless, there are some additional, less understood sources of discrepancy between the calculated and experimental electric field gradients. A striking example of such a disagreement for ²⁵Mg was demonstrated recently for MgBr_2 .²⁵ Even after a complete optimization of the structure and nearly perfect agreement between the experiment and CASTEP calculations for the EFG tensor at the ^{79/81}Br site, there was a substantial disagreement for the calculated C_Q for ²⁵Mg. Similarly, a substantial (up to 40%) systematic overestimation in the calculated C_Q 's, that could not be attributed to inaccuracies in the crystal structures, has been observed in the case of ^{35/37}Cl in alkaline earth chloride hydrates.¹⁷⁵

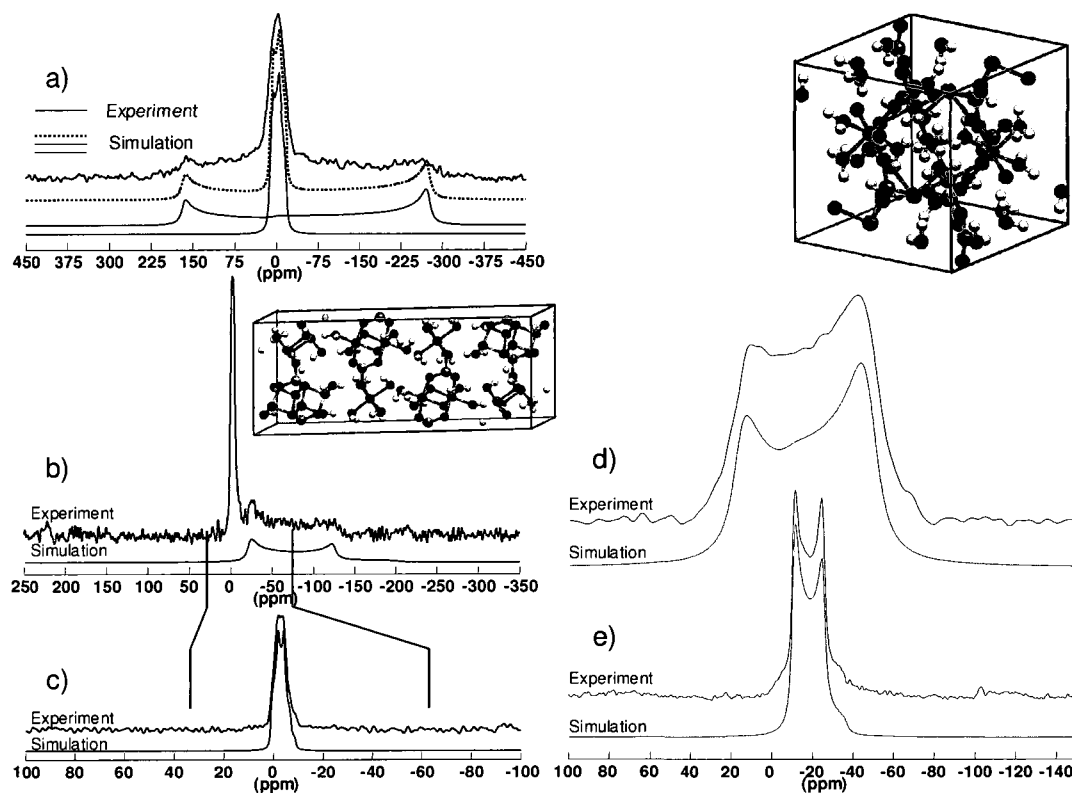


Figure 15 – ^{25}Mg SS-NMR spectra (experimental and simulated) of a) Both sites in $\text{Mg}_3(\text{PO}_4)_2 \cdot 8\text{H}_2\text{O}$ – Static Hahn Echo. b) The second, broader site of $\text{Mg}_3(\text{PO}_4)_2 \cdot 8\text{H}_2\text{O}$ – 12 kHz MAS full Hahn Echo. Simulation of narrower signal shown in c). Unit cell is shown with Mg atoms in green. c) Narrow site of $\text{Mg}_3(\text{PO}_4)_2 \cdot 8\text{H}_2\text{O}$ – 5 kHz MAS Bloch Decay. The second site (in b)) is too broad to be seen at this spinning speed. d) $\text{MgHPO}_4 \cdot 3\text{H}_2\text{O}$ – Static Hahn Echo. Unit cell is shown. e) $\text{MgHPO}_4 \cdot 3\text{H}_2\text{O}$ – 5 kHz MAS Bloch Decay.

Another group of oxygen-coordinating Mg compounds studied were the following anhydrous salts: forsterite (Mg_2SiO_4), MgMoO_4 , MgWO_4 , $\alpha\text{-Mg}_2\text{V}_2\text{O}_7$, $\text{Mg}(\text{VO}_3)_2$, $\text{Mg}_3(\text{VO}_4)_2$, geikielite (MgTiO_3), magnesite (MgCO_3), spinel (MgAl_2O_4) $\alpha\text{-MgSO}_4$, $\beta\text{-MgSO}_4$ (Figures 16 – 19 and A4 - A8 in Appendix A), and reference is made to åkermanite ($\text{Ca}_2\text{MgSi}_2\text{O}_7$) investigated by Kroeker and Stebbins.¹⁷⁶ This group, in fact, contains a few Mg-containing minerals. Generally, SS-NMR of minerals can sometimes be difficult due to fractional occupancies of some lattice sites as well as the possibility of paramagnetic impurities. This can potentially cause distributions in the spectral

parameters and broadening of the signals. Nevertheless, as one can see from Table 4 and Figures 17, 18 and 19, the spectra for forsterite, geikielite, magnesite and spinel were obtained with relative ease. The chemical shift range for this class of compounds, although still not very large, varies more than that for compounds with primarily water-coordination at the Mg site. For these compounds δ_{iso} ranges from the most deshielded $\delta_{iso} = 48.20 \pm 1.00$ ppm for the one site in spinel (MgAl_2O_4) to the most shielded $\delta_{iso} = -10.55 \pm 0.30$ ppm for one site of MgMoO_4 (Figure 16). In fact, it is interesting to note that the most deshielded ^{25}Mg sites in this group, spinel (MgAl_2O_4) and åkermanite ($\text{Ca}_2\text{MgSi}_2\text{O}_7$) (Table 4), are also the only compounds with Mg in a tetrahedral coordinating environment in this group (Table 3). This moderate isotropic chemical shift range is reproduced by calculations with a fair degree of accuracy as can be seen in Table 4 and Figure 11. Quadrupolar coupling constants for these compounds range from about 2 MHz to over 10 MHz (Table 4) with β - MgSO_4 having the largest $C_Q = 10.4 \pm 0.1$ MHz in this group (Figure 16). All compounds in this set have notably asymmetrical environments for the magnesium centres. The exception to this being magnesite (MgCO_3) with S_6 symmetry at the single magnesium site. This results in an almost perfectly axially symmetric EFG tensor with $\eta_Q = 0.04 \pm 0.02$ (Figure 17). The quadrupolar coupling constant for magnesite is $C_Q = 2.24 \pm 0.02$ MHz, however, as can be seen from the static spectrum (Figure 17), the quadrupolar interaction dominates and the shielding CSA interaction is too small to be determined. ^{25}Mg SS-NMR for MgCO_3 has been previously reported by Bastow¹⁷⁷ and their results match what is reported herein quite well. Although CASTEP correctly predicts the axially symmetric nature of the EFG tensor, the quadrupolar coupling constant is somewhat overestimated with $C_Q^{calc} = -3.56$ MHz,

which is about a 60% disagreement and increase from experiment. In these calculations the same crystal structure for MgCO_3 ¹⁵⁶ that has been used in previous calculations using the Wien97 package¹⁷⁷, which produced only about a 10% discrepancy with the experimentally determined C_Q . In fact, all three crystallographic datasets reported for MgCO_3 ^{156, 178, 179} produced poor agreement between CASTEP calculated quadrupolar coupling constants and experimental findings. It should also be noted that geometry optimization of the experimental structures did not produce any significant improvement either: $C_Q^{calc} = -3.56$ MHz without optimization, and $C_Q^{calc} = 3.38$ MHz with a complete atom optimization. Since the earlier Wien97 calculations for magnesite¹⁷⁷ reproduce the quadrupolar parameters very well, it is unlikely that the dynamic processes in the lattice (i.e. rotation of CO_3 -groups) can be the cause of disagreement between the experimental and the CASTEP calculated quadrupolar coupling. At this time it is difficult to say why there is such a large discrepancy between calculated and experimental C_Q in such a seemingly uncomplicated compound such as MgCO_3 .

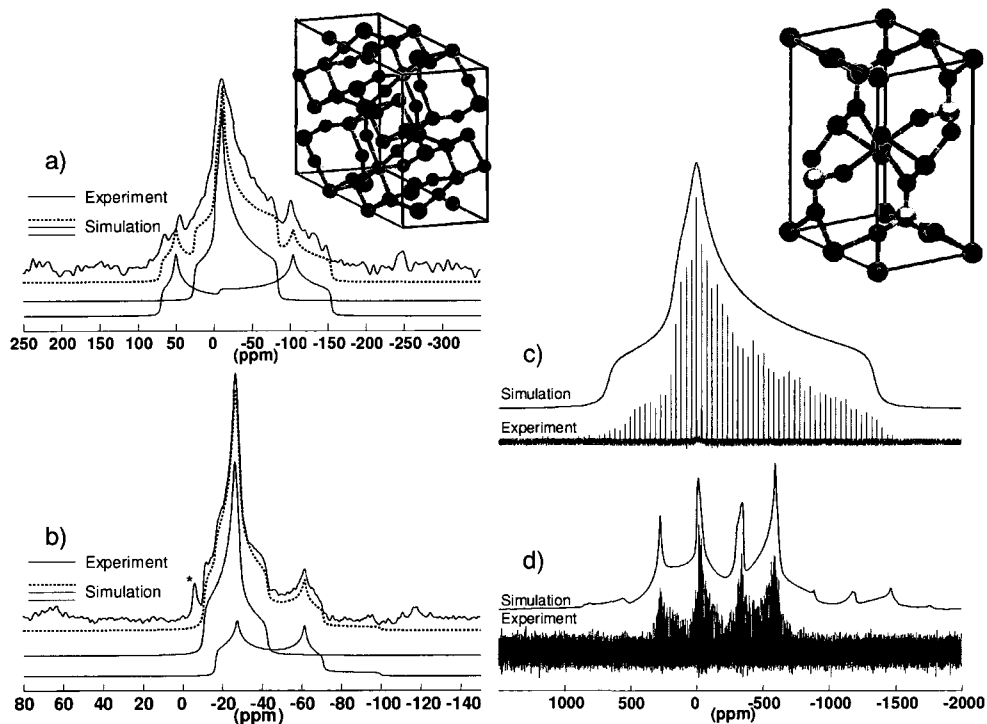


Figure 16 – ^{25}Mg SS-NMR spectra (experimental and simulated) of a) MgMoO_4 – Static Hahn Echo. Unit cell is shown with Mg atoms in green. b) MgMoO_4 – 5 kHz MAS Bloch Decay. *impurity. c) $\beta\text{-MgSO}_4$ – Static QCPMG. Unit cell is shown. d) $\beta\text{-MgSO}_4$ – 16 kHz MAS QCPMG.

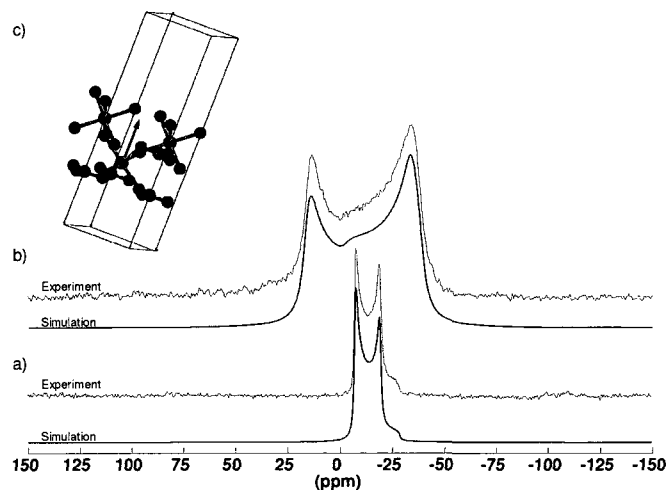


Figure 17 – a) 5 kHz MAS Bloch decay ^{25}Mg SS-NMR spectrum of natural magnesite (MgCO_3). b) Static Bloch decay ^{25}Mg SS-NMR spectrum of natural magnesite. Note that little to no CSA interaction was observed in the static spectrum. c) Representative portion of the magnesite unit cell showing the single crystallographically unique Mg site and the C_3 rotation axis (black arrow).

Similar to magnesite, the calculations for geikielite (MgTiO_3) produced an axially symmetric EFG tensor such that $\eta_Q = 0$. This makes sense as the point group at the magnesium site (C_3) in this compound is similar to that of magnesite in that it contains a proper 3-fold axis of rotation. However, the experimentally determined asymmetry parameter, within error, shows a slight deviation from perfect axial symmetry ($\eta_Q^{\text{expt}} = 0.10 \pm 0.04$) (Figure 18). It would appear that although the $R\bar{3}$ space group of crystalline geikielite (Table 3) should display an axially symmetric EFG tensor, there are presumably enough distortions in the system due to local disorder or possible fractional occupancies to break the symmetry enough to result in a non-zero η_Q . It is also important to note that NMR parameters for MgTiO_3 have been previously reported by Padro et al. and quadrupolar interaction parameters C_Q and η_Q reported herein match perfectly with their study.¹⁸⁰

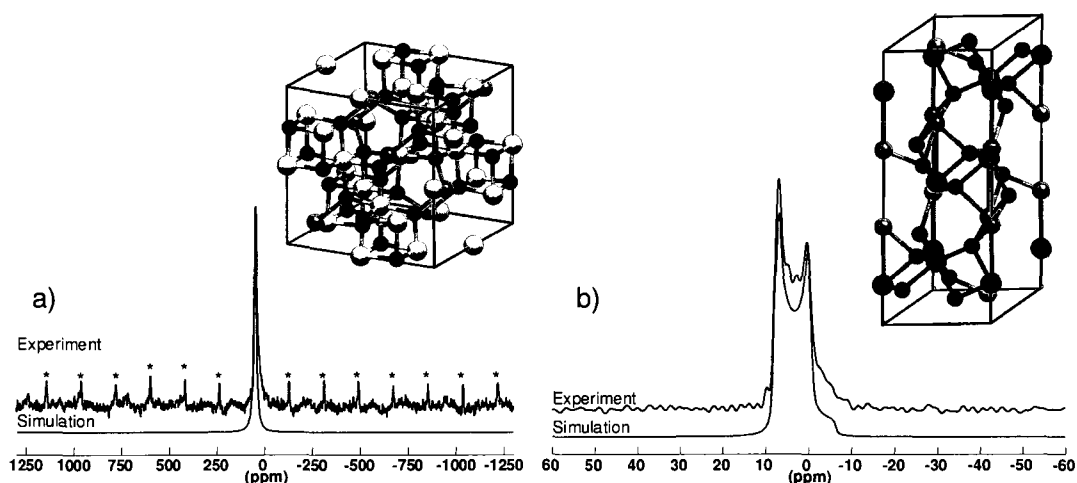


Figure 18 – ^{25}Mg SS-NMR spectra (experimental and simulated) of a) Spinel (MgAl_2O_4) – 10 kHz MAS Bloch Decay. * spinning sidebands. Unit cell is shown with Mg atoms in green. b) Geikielite (MgTiO_3) – 5 kHz MAS Bloch Decay. Unit cell shown.

Another interesting example in this group is another natural mineral forsterite (Mg_2SiO_4), as the quadrupolar interaction parameters have been previously reported by Derighetti et

al.,⁸ one of the earliest ^{25}Mg SS-NMR studies. This single-crystal Dynamic Nuclear Polarization (DNP)-NMR study provides the most accurate-to-date C_Q and η_Q values for both Mg sites in crystalline forsterite and our experimental powder data confirms this early study (Table 4 and Figure 19). The agreement between calculated and experimental NMR parameters for forsterite is also quite reasonable.

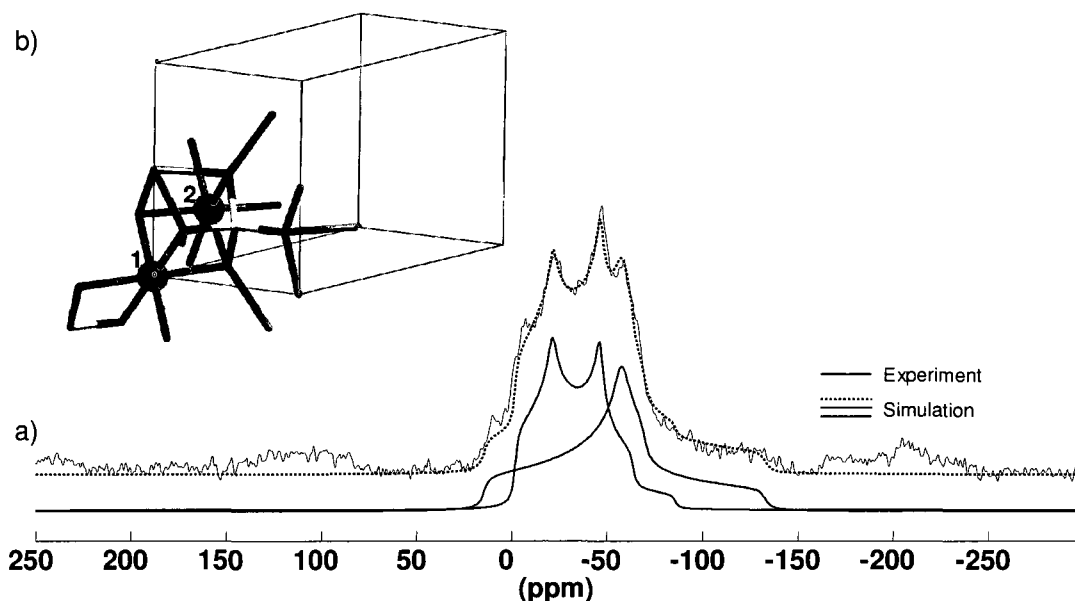


Figure 19 – a) 8 kHz MAS Bloch decay ^{25}Mg SS-NMR spectrum of natural forsterite (Mg_2SiO_4) showing both crystalline Mg sites resolved clearly. b) Representative portion of the forsterite unit cell showing the two crystallographically unique Mg sites.

^{25}Mg SS-NMR parameters for $\text{Mg}(\text{VO}_3)_2$ have also been reported previously by Larsen et al.¹⁸¹ The agreement between this previous report and the parameters reported herein is quite good, the exception being the reported value for η_Q . Acquiring a spectrum for this particular compound proved somewhat difficult given the relatively large quadrupolar coupling constant ($C_Q = 8.85 \pm 0.10$ MHz) (Figure A5 in Appendix A) and, as well, in both studies this compound was synthesized with unknown levels of purity. The PXRD of the material studied in this work (not shown) indicates that some unknown

impurities are indeed present. Given the nature of the various spectra obtained for this compound, it was, therefore, assumed that although there is a second singularity present in the spectrum that may appear to be part of a site with a smaller value for η_Q it is in fact an impurity and η_Q is actually much closer to 1 (Table 4). This, however, is not supported by the CASTEP calculations and the calculated C_Q is much larger than the experimental value. This inaccuracy in calculations may be explained by either a faulty or inaccurate crystal structure or poorly represented pseudopotentials for ^{25}Mg and/or other neighboring atoms in the crystal. In general, there is a slight tendency for these CASTEP calculations to overestimate C_Q values (Figure 12). This may suggest that the problem stems from the use of pseudopotential approximations instead of full electron functions.

The last group of oxygen-coordinating Mg compounds examined are those that may be described as organometallic Mg complexes or as the magnesium salts of organic acids: $\text{Mg}(\text{HCOO})_2 \cdot 2\text{H}_2\text{O}$, $\text{Mg}(\text{AcAc})_2 \cdot 2\text{H}_2\text{O}$, and $\text{Mg}(\text{OAc})_2 \cdot 4\text{H}_2\text{O}$ (Figure 20). As with previous compounds, the correlation between calculated chemical shielding and the experimental chemical shift is excellent (Table 4 and Figure 11). The error on δ_{iso} for $\text{Mg}(\text{AcAc})_2 \cdot 2\text{H}_2\text{O}$ is relatively large ($\delta_{iso} = 4.5 \pm 4.0$ ppm), however, it is still within the expected range looking at all the materials studied as a whole. Interestingly, the crystal structure of $\text{Mg}(\text{HCOO})_2 \cdot 2\text{H}_2\text{O}$ dictates two distinct Mg sites (Table 3) and these two sites are clearly resolved in the NMR spectrum for this compounds, giving reasonable NMR parameters (Table 4). The quadrupolar coupling constants for these compounds are quite moderate with $\text{Mg}(\text{AcAc})_2 \cdot 2\text{H}_2\text{O}$ having the largest $C_Q = 7.4 \pm 0.1$ MHz. Structurally speaking, all three of these compounds have octahedrally coordinated Mg,

like most of the compounds studied. However, the presence of these bulkier, carbon-containing ligands breaks the seemingly symmetric environment for Mg in these complexes, creating a fairly large quadrupolar coupling constant. The distortions in the crystal structure create a large degree of axial asymmetry, especially for $\text{Mg}(\text{AcAc})_2 \cdot 2\text{H}_2\text{O}$ where $\eta_Q = 1.00 \pm 0.02$. Although the computations once again overestimate the C_Q values (Table 4), they still correctly reproduce the trend of large C_Q and η_Q . Both $\text{Mg}(\text{OAc})_2 \cdot 4\text{H}_2\text{O}$ and $\text{Mg}(\text{HCOO})_2 \cdot 2\text{H}_2\text{O}$ have been studied previously by Sham and Wu at 11.7 T.²⁴ However, the NMR parameters they obtained for these two compounds are quite different from what is reported herein. It is possible that there were variations in hydration levels between the compounds studied but it is difficult to speculate exactly the reason behind this discrepancy. The previous study used materials enriched in ^{25}Mg and prepared in small quantities, which may have prevented accurate tests of the phase purity of these prepared materials. In this study the phase purity of the compounds was tested thoroughly using PXRD, and even at natural abundance spectra have better defined line shapes and higher signal to noise ratios than those obtained for the enriched samples. Therefore, it is believed that the spectral parameters obtained in this work are more accurate.

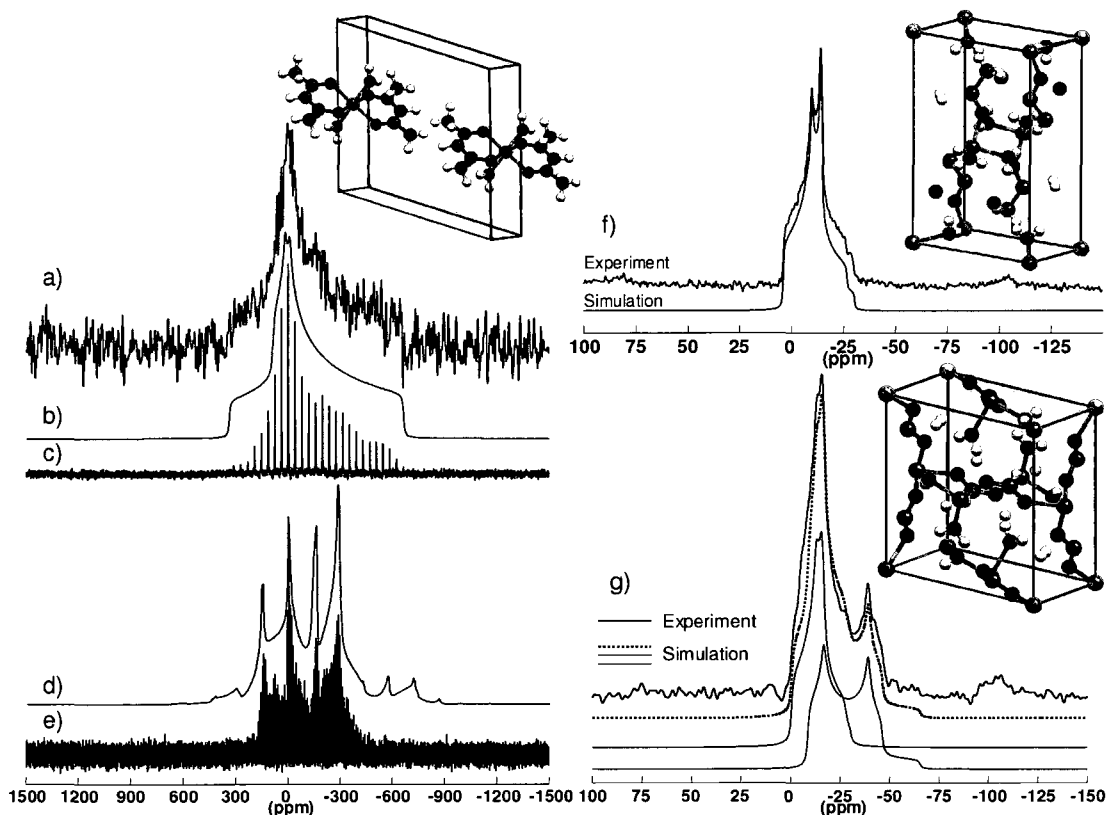


Figure 20 – ^{25}Mg SS-NMR spectra (experimental and simulated) of a) $\text{Mg}(\text{AcAc})_2 \cdot 2\text{H}_2\text{O}$ – Static Hahn Echo obtained in 3 pieces using varying central excitation frequencies (O1) to observe edge singularities. Unit cell shown with Mg atoms in green. b) Simulation of a) and c). c) $\text{Mg}(\text{AcAc})_2 \cdot 2\text{H}_2\text{O}$ – Static QCPMG. d) Simulation of e). e) $\text{Mg}(\text{AcAc})_2 \cdot 2\text{H}_2\text{O}$ – 5 kHz MAS QCPMG. f) $\text{Mg}(\text{OAc})_2 \cdot 4\text{H}_2\text{O}$ – 5 kHz MAS Bloch Decay. Unit cell is shown. g) $\text{Mg}(\text{HCOO})_2 \cdot 2\text{H}_2\text{O}$ – 12 kHz MAS Hahn Echo. Unit cell is shown.

3.6 Mg in Non-O-coordinating Environments

Given the prevalence of oxygen in inorganic salts of Mg there are few compounds where Mg is in an environment that is not oxygen-coordinated. The materials studied in this work that fall in this category can be divided roughly either into Mg in a more ionic environment or Mg in a more covalent or network environment.

The materials with Mg in a more ionic environment studied here include: MgS, MgH₂, and MgCl₂ (Figure 21 and Figure A9 in Appendix A). Magnesium sulfide is relatively unexciting as it bears many similarities to MgO and crystallizes in the same *Fm-3m* cubic space group (Table 3). The chemical shift for ²⁵Mg in MgS is obviously different from that of MgO and was found to be $\delta_{iso} = -1.11 \pm 0.02$ ppm. This chemical shift correlates well with the calculated absolute shielding of $\sigma_{iso}^{calc} = 568.34$ ppm. Like MgO, Mg in MgS is in an O_h symmetrical environment resulting in a zero electric field gradient felt at the Mg nucleus (Table 4). MgS has been previously reported by Dupree and Smith¹⁸ with an isotropic chemical shift of -3 ± 0.5 ppm. It is most likely that the slight discrepancy for δ_{iso} in the previous study of MgS is due to differences in the reference used. Another non-oxygen-coordinating magnesium compound, anhydrous MgCl₂, is quite interesting in the way it differs from the hexahydrated form. It is, in fact, slightly more deshielded than in the hydrated form with $\delta_{iso} = 2.32 \pm 0.10$ ppm. This makes sense given that the first-coordination sphere changes from octahedral Mg in an OH₂ environment to octahedral Mg in a Cl environment. Similar to previous compounds, the experimental chemical shift matches calculations well. Interestingly, the change in first coordination sphere and the lack of water change the space group to the hexagonal *R-3m* with the Mg centre having a slightly distorted octahedral geometry (Table 3) with point group D_{3d} giving a $C_Q = 1.62 \pm 0.02$ MHz. The EFG tensor is also axially symmetric with $\eta_Q = 0.00 \pm 0.05$ which is unsurprising considering the proper 3-fold rotation axis present at the Mg centre under D_{3d} symmetry.¹⁷³ It can be seen in the MAS spectrum for MgCl₂ (Figure 21), however, that there appears to be a slight distortion in the spectrum as an increased intensity in the high-field singularity. This most likely arises

from the specific morphology of the crystallites (e.g. thin flakes, needles), that may produce a dominant orientation of the crystals in a powder. Another interesting compound studied was MgH_2 , which has one crystallographically unique Mg site and crystallizes in the $P4_2/mnm$ tetragonal space group (Table 3). This compound has a slightly deshielded Mg site with a chemical shift of $\delta_{iso} = 10.3 \pm 1.0$ ppm, which correlates well with the calculated chemical shielding. It also has a fairly modest quadrupolar coupling constant, $C_Q = 3.06 \pm 0.02$ MHz, and an axially asymmetric EFG tensor with $\eta_Q = 0.89 \pm 0.05$. This compound is one of the unusual cases where the CASTEP calculations underestimate the strength of the quadrupolar interaction with $C_Q^{calc} = -1.49$ MHz (for optimized structure $C_Q^{calc} = -2.18$ MHz) (Figure 12). However, noting the D_{2h} symmetry at the Mg centre, it is not surprising the C_Q and η_Q are both non-zero.

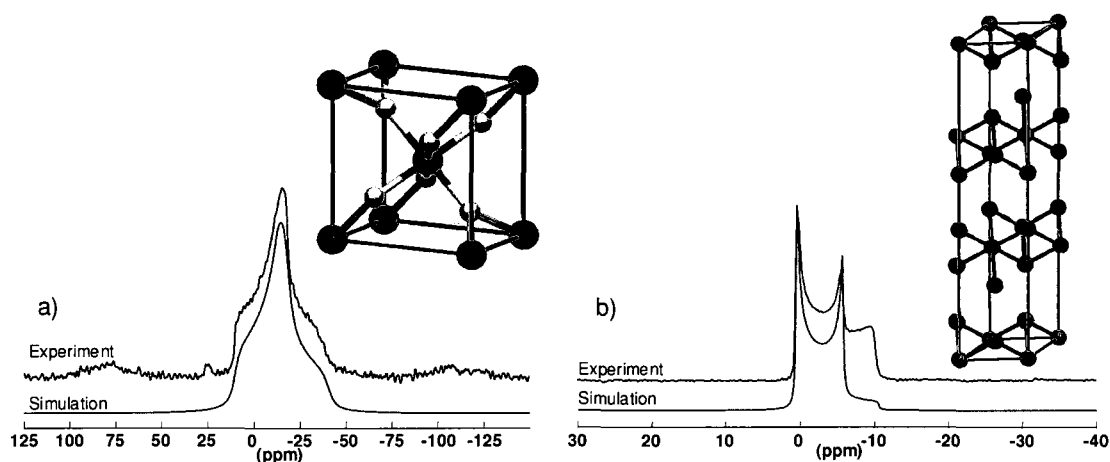


Figure 21 – ^{25}Mg SS-NMR spectra (experimental and simulated) of a) MgH_2 – 5 kHz MAS Bloch Decay. Unit cell shown with Mg atoms in green. b) MgCl_2 – 5 kHz MAS Bloch Decay. Unit cell shown.

One of the most dramatic discoveries of this ^{25}Mg SS-NMR study was the class of “covalent”-like non-oxygen-coordinating Mg materials, even though a small handful

were studied. Mg_2Si , Mg_3N_2 and Mg-phthalocyanine (Mg-pc) (Figures 22, 23, and A10 in Appendix A) were examined in this study and reference is made to bis(cyclopentadienyl)-magnesium (MgCp_2) investigated by Hung and Schurko.²³ To the best of our knowledge, the materials in this group demonstrate the largest reported chemical shift range for any Mg-containing compounds. MgCp_2 has the most shielded Mg site with $\delta_{iso} = -91 \pm 3$ ppm, a moderate quadrupolar interaction with $C_Q = 5.80 \pm 0.05$ MHz and $\eta_Q = 0.01 \pm 0.01$. The next nearest shielded Mg environment is one of the sites in MgMoO_4 , showing the interesting shielding environment that an aromatic ligand like cyclopentadienyl provides. Mg_2Si and Mg_3N_2 are at the opposite end of the chemical shift range, being the most deshielded Mg environments yet reported. As well, it is of interest to note that both Mg_2Si and Mg_3N_2 have tetrahedrally coordinated Mg sites. It should be noted that given the quite dramatic and interesting results obtained for Mg-pc, the isotropic shift for ^{25}Mg in this environment is unknown, within experimental error. However, given the remarkable results obtained for the isotropic chemical shifts for the other compounds in this group it is expected that δ_{iso} for ^{25}Mg in Mg-pc would not be in the typical range of -10 to 15ppm either. Mg_2Si has $\delta_{iso} = 61.67 \pm 0.10$ ppm and matches quite well with the predicted CASTEP shielding. The chemical shift has been previously reported by Dupree and Smith¹⁸ and the two values are well within uncertainty for the experimentally determined chemical shifts. This material crystallizes in a cubic $Fm\bar{3}m$ space group (Table 3) and the one crystallographically unique Mg site has perfect T_d symmetry, so of course, there is no measurable quadrupolar interaction for ^{25}Mg in this material. The shielding interaction in Mg_3N_2 is somewhat similar to Mg_2Si , however, its one crystallographically unique Mg site is much more deshielded with $\delta_{iso} = 101.0 \pm 2.0$

ppm. Unsurprisingly, this compound has the lowest calculated absolute isotropic shielding value for all of the compounds studied and this matches well with the observed correlation. NMR parameters for Mg_3N_2 have been previously reported by Dupree and Smith as well.¹⁸ They report a peak maximum for ^{25}Mg in Mg_3N_2 at 10 ± 100 ppm, which does not quite coincide with any peak maxima in the ^{25}Mg spectrum for Mg_3N_2 reported herein. It is possible that in the previous study only a part of the spectrum was excited and fine structure was not observed. There are several other aspects of Mg_3N_2 which make it quite interesting. First of all, like Mg_2Si , Mg in Mg_3N_2 is in a tetrahedral arrangement that crystallizes in the cubic $Ia-3$ space group (Table 3). However, although this is a cubic unit cell, the Mg site is far from T_d symmetry. In fact, the site is so distorted from perfect tetrahedral symmetry that it is only C_1 symmetry. So, as expected, ^{25}Mg in Mg_3N_2 has a strong quadrupolar interaction with $C_Q = 9.30 \pm 0.05$ MHz and $\eta_Q = 0.44 \pm 0.01$. The EFG tensor parameters determined by calculations are quite accurate for this compound in particular (Table 4). It is possible that the crystal structure used for calculation is quite accurate or it is possible that both Mg and N pseudopotentials were very applicable in this particular case. Either way, knowing that the isotropic chemical shift and EFG tensor parameters were calculated accurately, it was reasonable to assume that the calculated anisotropy in the shielding interaction may be quite accurate. As such, aside from Mg₂pc, Mg_3N_2 has the largest calculated shielding anisotropy, with $\Delta\sigma_{\text{aniso}}^{\text{calc}} = 40.84$ ppm, of all the compounds examined. So, this compound would be an excellent opportunity to possibly observe an anisotropic shielding interaction. As can be seen in Figure 22 and Table 5, an anisotropy of $\Delta\sigma_{\text{aniso}} = 42.0 \pm 6.0$ ppm with $\eta_{\text{CSA}} = 0.78 \pm 0.10$ was found for ^{25}Mg in Mg_3N_2 . These values match quite well with calculated values,

however, it is still interesting to note that CASTEP calculated shielding anisotropies are, in general, quite small. Looking at the calculated shielding anisotropies for the compounds studied (Table 4), it is then of no surprise that the quadrupolar interaction dominates by far over the shielding interaction in the majority of magnesium-containing compounds. An excellent example of this effect occurs in Mg-pc, where the single crystallographically unique Mg site gives a ^{25}Mg quadrupolar coupling constant of $C_Q = 26.9 \pm 0.5$ MHz with $\eta_Q = 0.0 \pm 0.1$ (Figure 23 and Table 4). This is, so far, the largest known quadrupolar coupling reported for ^{25}Mg , with the next largest being $C_Q = 15.32$ MHz for bis(pyridine)-(5,10,15,20-tetraphenylporphyrinato)-magnesium(II) reported by Wu et al.²⁷ Given such a large quadrupolar coupling constant it is then of no surprise that the spectrum of ^{25}Mg -enriched material has to be collected using the WURST-QCPMG sequence over several transmitter frequencies. It should be noted that there is an additional signal present in the ^{25}Mg SS-NMR spectrum for Mg-pc with a $C_Q \approx 12$ MHz and $\eta_Q \approx 0.75$. This is expected to be some form of the starting material, monopyrindinated aqua(magnesium) phthalocyanine as previously reported ^{25}Mg quadrupolar coupling interaction parameters for substituted Mg-pc materials are similar to those found here.²⁶

²⁷ Additional heating under vacuum reduces the intensity of the signal with the smaller C_Q with corresponding increase in intensity of the broader signal. This demonstrates the release of the acetate moiety in the starting material to leave only pure Mg-pc behind.²⁶ It is extremely difficult to experimentally determine the isotropic chemical shift from such a broad spectrum and the isotropic shift for ^{25}Mg in this environment remains unknown. However, given the remarkable values of isotropic chemical shifts for the other compounds in this group it is expected that δ_{iso} for ^{25}Mg in Mg-pc would not be in the

typical range of -10 to 15 ppm either. Using the obtained correlation between experiment and calculation (Figure 11), the isotropic chemical shift can be estimated from the calculated isotropic chemical shielding of $\sigma_{iso}^{calc} = 523.79$ ppm, giving a proximity δ_{iso} of ~42 ppm. Together with the results for Mg_3N_2 this points that nitrogen-coordinated Mg sites are in a more deshielding environment than that of oxygen-coordinating materials. Mg-pc crystallizes in a monoclinic lattice with space group $P2_1/c$ where the Mg-pc molecules form a somewhat offset layered structure. It is then of no surprise that the symmetry at the Mg site is merely C_i and the quadrupolar coupling constant is as large as it is ($C_Q = 26.9 \pm 0.5$ MHz with $\eta_Q = 0.0 \pm 0.1$). Given the low level of symmetry at the Mg site there is no reason to assume an axially symmetric EFG tensor, although calculations give $\eta_Q = 0.08$. However, when considering the local symmetry at the Mg centre, and a resonance structure assumed for the phthalocyanine ligand, then the Mg centre assumes pseudo- D_{4h} symmetry. Such a high degree of local symmetry could explain the axially symmetric nature of the EFG tensor. As well, similar to most of the other calculations, the calculated quadrupolar coupling constant is severely overestimated with $C_Q^{calc} = 39.4$ MHz. It is possible that the impurities present are impeding pure crystallinity of Mg-pc, that there are possible dynamic processes unaccounted for in the crystal structure, or the possibility of π -stacking among planar molecules reduces the electric field gradients throughout the crystal. The calculated shielding anisotropy for Mg-pc is the largest calculated anisotropy with $\Delta\sigma_{aniso}^{calc} = 68.94$ ppm, however, given that the ^{25}Mg site is dominated by the quadrupolar interaction, it is not surprising that this has not been detected.

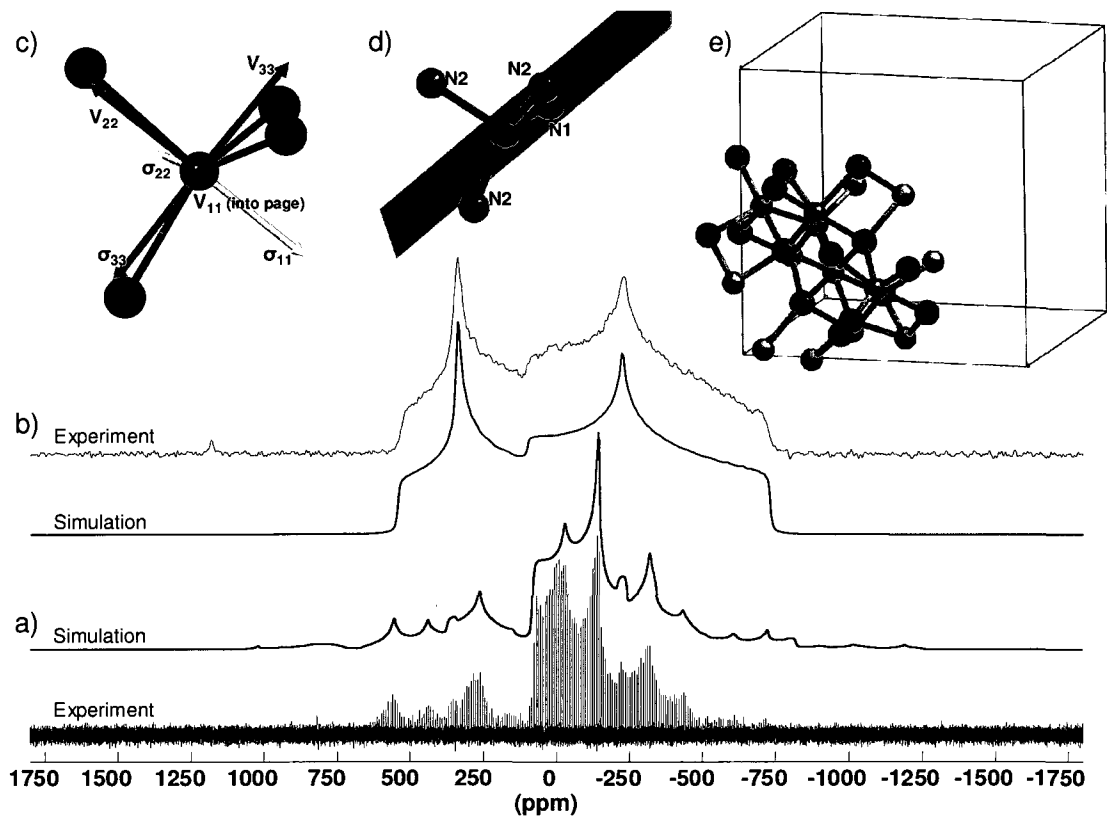


Figure 22 – a) 16 kHz MAS-synchronized QCPMG ^{25}Mg SS-NMR spectrum of Mg_3N_2 . b) Static Bloch decay ^{25}Mg SS-NMR spectrum of Mg_3N_2 . c) Calculated CSA and EFG tensor orientations are shown for the single crystallographically unique Mg site in Mg_3N_2 . d) Mean plane through symmetrically distinct nitrogens N1 and N2 as well as the single Mg site in the crystal lattice to show the break in tetrahedral symmetry around the Mg site. e) Representative portion of the cubic unit cell.

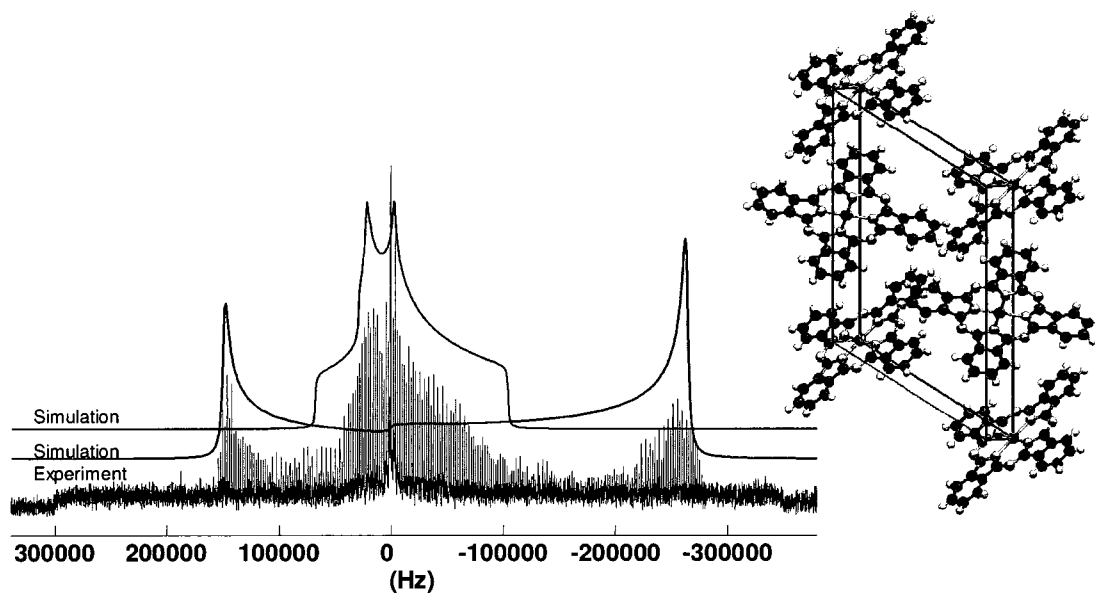


Figure 23 – Static WURST-QCPMG ^{25}Mg (enriched in ^{25}Mg) SS-NMR spectrum of Mg-phthalocyanine. The signal with the smaller C_Q (purple simulation) is an impurity or starting material (see text). Unit cell is shown with Mg atoms in green.

4. ^{33}S in Anhydrous Sulfates

As previously mentioned, ^{33}S is similar to ^{25}Mg in that it is a quadrupolar nucleus (although with $I = 3/2$) with low natural abundance and has a relatively low magnetogyric ratio. This makes ^{33}S SS-NMR, in general, quite difficult. As such, the reports on ^{33}S SS-NMR are few indeed. However, the focus of this work is not to investigate the range of SS-NMR parameters of previously unstudied systems as in the case of ^{25}Mg . Now the aim is to evaluate the possibility of using SS-NMR on this challenging nucleus in conjunction with *ab initio* DFT calculations in structural studies of sulfur-containing materials. As a starting point we have chosen anhydrous sulfates.

4.1 Structural Details of Systems Studied

The specific compounds under study were previously mentioned along with the number of earlier reported structures for each of the sulfates (Table 2). Table 6 shows the structural details for each of the sulfates reviewed in this work.

Table 6 – Structural details of sulfate compounds studied.

Structural Parameters							S site Point Group	Method & Reference
Compound	a (Å)	b (Å)	c (Å)	Z	Space Group	Cell		
Li ₂ SO ₄ [1]	8.2500	4.9500	8.4400	4	<i>P 2₁/a</i>	Monoclinic ($\beta = 107.9^\circ$)	C ₁	S.C. X-ray ⁴³ , 1964
Li ₂ SO ₄ [2]	8.239	4.9540	8.474	4	<i>P 2₁/a</i>	Monoclinic ($\beta = 107.9^\circ$)	C ₁	RT S.C. X-ray ⁴⁴ , 1976
Na ₂ SO ₄ [1]	5.8630	12.3040	9.8210	8	<i>Fddd</i>	Orthorhombic	D ₂	RT S.C. X-ray ⁴³ , 1964
Na ₂ SO ₄ [2]	9.829	12.302	5.868	8	<i>Fddd</i>	Orthorhombic	D ₂	RT S.C. X-ray ⁴⁶ , 1975
K ₂ SO ₄	5.7704	10.0712	7.4776	4	<i>Pmcn</i>	Orthorhombic	C _s	RT S.C. X-ray ⁴⁸ , 1995
Rb ₂ SO ₄ [1]	7.8128	10.4255	5.9694	4	<i>Pnam</i>	Orthorhombic	C _s	RT S.C. X-ray ⁵² , 1974
Rb ₂ SO ₄ [2]	7.8035	5.9725	10.4101	4	<i>Pnma</i>	Orthorhombic	C _s	RT S.C. X-ray ⁵³ , 2010
Rb ₂ SO ₄ [3]	7.8133	5.9717	10.4269	4	<i>Pnma</i>	Orthorhombic	C _s	RT S.C. X-ray ⁵³ , 2010
Cs ₂ SO ₄ [1]	8.1980	6.2180	10.8840	4	<i>Pnma</i>	Orthorhombic	C _s	RT S.C. X-ray ⁴³ , 1964
Cs ₂ SO ₄ [2]	8.2329	6.2538	10.9344	4	<i>Pnma</i>	Orthorhombic	C _s	RT S.C. X-ray ⁵⁵ , 2010
(NH ₄) ₂ SO ₄ [1]	7.7820	5.9930	10.6360	4	<i>Pnma</i>	Orthorhombic	C _s	S.C. X-ray ⁴³ , 1964
(NH ₄) ₂ SO ₄ [2]	7.7820	10.6360	5.9930	4	<i>Pnam</i>	Orthorhombic	C _s	RT S.C. Neutron ⁵⁷ , 1966
(NH ₄) ₂ SO ₄ [3]	7.7804	5.9876	10.6323	4	<i>Pnma</i>	Orthorhombic	C _s	RT S.C. X-ray ⁵⁸ , 2010
α -MgSO ₄	5.1747	7.8756	6.4952	6	<i>Cmcm</i>	Orthorhombic	C _{2v}	RT Powder Neutron ⁶⁰ , 2007
β -MgSO ₄ [1]	8.5787	6.6953	4.7438	4	<i>Pnma</i>	Orthorhombic	C _s	RT S.C. X-ray ⁶¹ , 2007
β -MgSO ₄ [2]	4.7460	8.5831	6.7093	4	<i>Pbnm</i>	Orthorhombic	C _s	RT Powder Neutron ⁶⁰ , 2007
CaSO ₄ [1]	6.2380	6.9910	6.9960	6	<i>Bbmm</i>	Orthorhombic	C _{2v}	S.C. X-ray ⁴³ , 1964
CaSO ₄ [2]	6.993	6.995	6.245	6	<i>Amma</i>	Orthorhombic	C _{2v}	RT S.C. X-ray ⁴⁵ , 1975
SrSO ₄	6.8671	8.3545	5.3458	4	<i>Pbnm</i>	Orthorhombic	C _s	S.C. X-ray ⁴⁷ , 1998
BaSO ₄ [1]	8.8701	5.4534	7.1507	4	<i>Pnma</i>	Orthorhombic	C _s	S.C. X-ray ⁴³ , 1964
BaSO ₄ [2]	8.884	5.458	7.153	4	<i>Pnma</i>	Orthorhombic	C _s	S.C. X-ray ⁴⁹ , 1967
BaSO ₄ [3]	8.8842	5.4559	7.1569	4	<i>Pnma</i>	Orthorhombic	C _s	RT S.C. X-ray ⁵⁰ , 1977
BaSO ₄ [4]	7.157	8.884	5.457	4	<i>Pbnm</i>	Orthorhombic	C _s	S.C. X-ray ⁵¹ , 1978
BaSO ₄ [5]	7.1540	8.8790	5.4540	4	<i>Pbnm</i>	Orthorhombic	C _s	S.C. X-ray ⁴⁷ , 1998
ZnSO ₄	8.604	6.746	4.774	4	<i>Pnma</i>	Orthorhombic	C _s	S.C. X-ray ⁵⁴ , 1988
In ₂ (SO ₄) ₃	8.44	8.44	23.093	6	<i>R -3</i>	Hexagonal	C ₁	S.C. X-ray ⁵⁹ , 1995
Ga ₂ (SO ₄) ₃	8.054	8.054	21.840	6	<i>R -3</i>	Hexagonal	C ₁	S.C. X-ray ⁵⁹ , 1995
Al ₂ (SO ₄) ₃	8.0246	8.0246	21.357	6	<i>R -3</i>	Hexagonal	C ₁	S.C. X-ray ⁵⁶ , 1993

As can be seen in Table 6 the structural parameters for many of the sulfates are quite similar. That is, the unit cells are mostly orthorhombic, aside from Li_2SO_4 and the Group 13 sulfates, and that the majority of the cells are less than 500 \AA^3 making them quite suitable for plane wave computational methods. It should also be noted that all of these compounds contain only one crystallographically unique sulfur site (see the corresponding .cif files in Appendix B). This makes acquisition of SS-NMR spectra somewhat simpler without the need for deconvolution of potentially complicated multiple sites as in the case of ^{25}Mg . Also, even though the unit cell and crystallographic coordinates vary between reported structures of the same compound they still share the same symmetry. One thing that is particularly interesting about all of these sulfates is that although the sulfur site in all these compounds is formally tetrahedral, none of them show perfect tetrahedral symmetry. None of the sulfur sites possess T_d point group symmetry, and generally have significantly lower symmetry (Table 6). This is particularly noticeable in the SS-NMR parameters obtained for these sulfates as shown in the next sections. As can be seen in Table 6, a few compounds are essentially isostructural. For example, Rb_2SO_4 and Cs_2SO_4 are isostructural, as well as SrSO_4 and BaSO_4 . One could expect that the Group 13 sulfates, $\text{Al}_2(\text{SO}_4)_3$, $\text{Ga}_2(\text{SO}_4)_3$, and $\text{In}_2(\text{SO}_4)_3$ would be isostructural too, however, the positions of the sulfur atoms (and SO_4^{2-} groups in general) (seen in Appendix B) are different for each compound, despite having the same space group.

4.2 Determination of ^{33}S NMR Parameters

Figures 24 – 34, 37, and 38 show representative natural abundance ^{33}S SS-NMR spectra for the studied sulfates. Only the central transition is observed both under MAS and for stationary samples. Various sensitivity enhancement techniques, such as QCPMG and RAPT, were used in some cases to improve signal to noise when quadrupolar coupling constants were relatively large (> 1.5 MHz). For all compounds the spectral data were obtained at 21.1 T ($\nu_0(^{33}\text{S}) = 69.1$ MHz). To remove potential ambiguity in the determination of the NMR parameters, for some materials spectra were also obtained at 9.4 T ($\nu_0(^{33}\text{S}) = 30.7$ MHz) and 11.7 T ($\nu_0(^{33}\text{S}) = 38.4$ MHz). It should be noted that Wagler et al.⁴⁰ have shown that spin-lattice relaxation time T_1 for ^{33}S in anhydrous sulfates can range from about 1 s ($(\text{NH}_4)_2\text{SO}_4$) to about 45 s (CaSO_4). As such, to reflect these various spin-lattice relaxation times, spectra were obtained with acquisition delays of 5-150 s resulting in high signal to noise ^{33}S spectra.

Table 7 shows the experimental and CASTEP calculated ^{33}S SS-NMR parameters for studied sulfates. Note that calculations are performed for each available structure. It can be seen that the calculated NMR parameters for different structures of the same compound vary substantially. It is important to mention that the calculation conditions (i.e. E_c and k-grid) were kept the same for materials of the same type, thus allowing a comparison between calculations on the basis of structure. For some of the sulfates studied in this work ^{33}S SS-NMR has been previously reported^{33, 34, 37, 38, 40} and our new ultra-high field data agree well with these previous reports. However, this work is the

first ^{33}S SS-NMR report of $\beta\text{-MgSO}_4$ (Figure 32), SrSO_4 (Figure 24), ZnSO_4 (Figure 25), $\text{Al}_2(\text{SO}_4)_3$ (Figure 28), $\text{Ga}_2(\text{SO}_4)_3$ (Figure 29), and $\text{In}_2(\text{SO}_4)_3$ (Figure 30) as well as being the first to report static ^{33}S SS-NMR spectra for most of these sulfates. The calculated isotropic shielding constants shown in Table 7 are given in absolute scale, and can not be directly compared to the experimental isotropic chemical shifts, δ_{iso} , referenced to of CS_2 ($\delta_{iso} = 0$ ppm). As noted earlier, the absolute chemical shielding can be converted to a chemical shift scale if the absolute shielding of the reference is known. In practice, however, it is quite difficult to determine the absolute shielding⁸⁰ and similar to the previous case of ^{25}Mg SS-NMR, a comparison between calculated chemical shielding and experimental chemical shift can be made for a number of compounds. Then, this relationship can be used to relate the chemical shifts and absolute shielding. The value for the calculated shielding can be further converted to a relative chemical shift as shown in Table 7. This relationship between the absolute chemical shielding and chemical shift is shown in the next section.

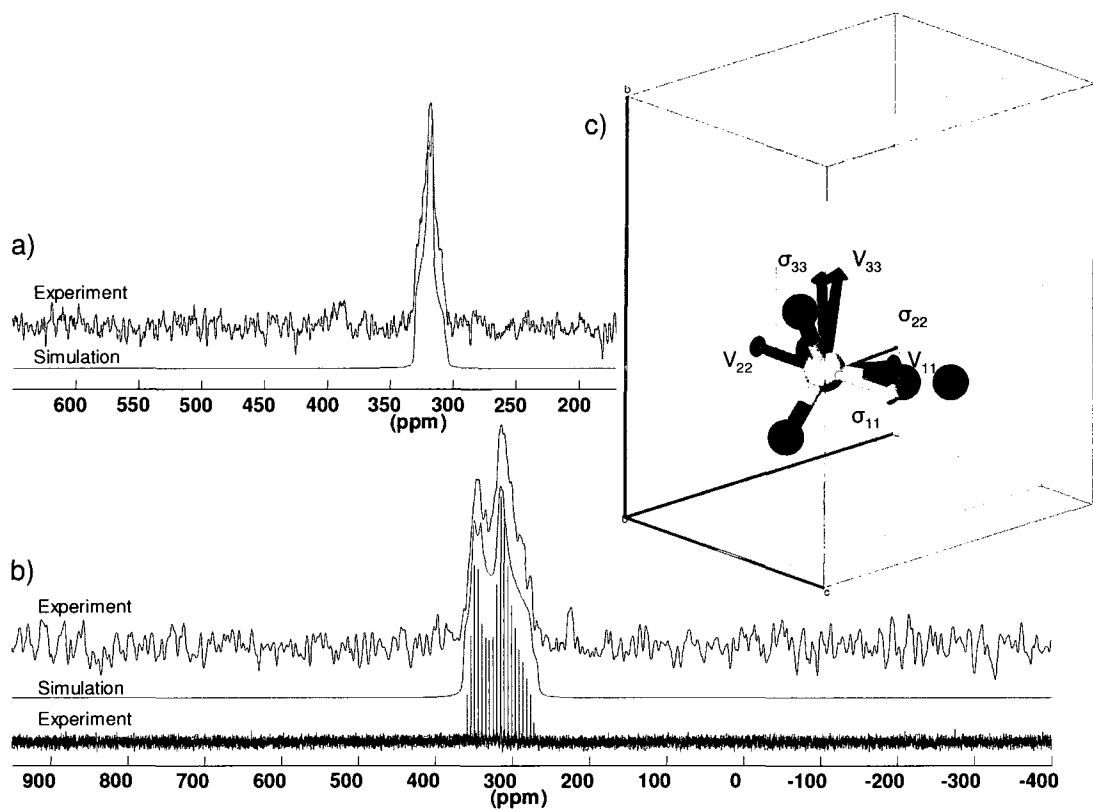


Figure 24 – ^{33}S SS-NMR spectra (experimental and simulated) for SrSO_4 . a) 5 kHz MAS Bloch Decay. b) Static QCPMG (lower) and Hahn Echo (upper). c) Representative portion of the unit cell showing the calculated orientations for the principal components of the EFG and CSA tensors. Sulfur, oxygen, and alkali earth metal are shown in yellow, red, and green respectively. The mirror plane present through sulfur is shown in yellow.

Table 7 – Experimental and calculated ^{33}S NMR parameters for all compounds studied.

Compound	NMR Parameters							$\{\alpha, \beta, \gamma\}$ (°)
	$\delta_{iso}/\sigma_{iso}$ [$\delta_{iso}^{calc,b}$] (ppm)	C_Q (MHz)	η_Q^a	$\Delta\sigma_{aniso}^c$ (ppm)	η_{CSA}^d			
Li_2SO_4	331.4 \pm 0.5	0.914 \pm 0.050	0.91 \pm 0.05	18.6 \pm 5.0	0.6 \pm 0.2		{120, 25, 25}	
CASTEP ('64) ⁴³	79.53 [354.6]	0.915	0.71	15.5	0.50		{225, 40, 210}	
CASTEP ('76) ⁴⁴	105.84 [328.3]	1.023	0.66	16.4	0.79		{170, 10, 270}	
Na_2SO_4	340.1 \pm 1.0	0.655 \pm 0.050	0.0 \pm 0.1	15.9 \pm 2.0	0.07 \pm 0.20		{90, 90, 0}	
CASTEP ('64) ⁴³	81.66 [352.4]	-0.495	0.73	4.3	0.12		{270, 90, 180}	
CASTEP ('75) ⁴⁶	93.51 [340.6]	-0.697	0.26	2.9	0.79		{270, 90, 90}	
K_2SO_4	336.1 \pm 0.5	0.997 \pm 0.050	0.44 \pm 0.10	-	-		-	
CASTEP ('95) ⁴⁸	103.92 [330.2]	0.924	0.35	20.9	0.27		{90, 0, 180}	
CASTEP ('95) ⁴⁸ [Geo-opt]	92.39 [341.7]	0.788	0.53	17.8	0.45		{90, 0, 0}	
Rb_2SO_4	336.4 \pm 1.0	0.860 \pm 0.050	0.4 \pm 0.1	16.7 \pm 5.0	0.4 \pm 0.3		{40, 0, 30}	
CASTEP ('74) ⁵²	105.40 [328.7]	0.578	0.88	13.2	0.33		{120, 90, 270}	
CASTEP ('74) ⁵² [Geo-opt]	92.99 [341.1]	0.865	0.44	21.5	0.25		{90, 0, 0}	
CASTEP ('10-1) ⁵³	104.64 [329.5]	0.873	0.25	20.3	0.14		{0, 10, 0}	
CASTEP ('10-1) ⁵³ [Geo-opt]	93.06 [341.0]	0.853	0.30	21.0	0.25		{270, 0, 180}	
CASTEP ('10-2) ⁵³	105.44 [328.7]	0.777	0.44	19.6	0.31		{270, 0, 180}	
CASTEP ('10-2) ⁵³ [Geo-opt]	92.61 [341.5]	0.874	0.36	21.1	0.25		{270, 0, 180}	
Cs_2SO_4	335.9 \pm 1.0	0.813 \pm 0.050	0.4 \pm 0.1	10.6 \pm 2.0	0.4 \pm 0.2		{140, 0, 5}	
CASTEP ('64) ⁴³	93.59 [340.5]	0.434	0.45	-10.9	0.89		{270, 75, 0}	
CASTEP ('64) ⁴³ [Geo-opt]	95.60 [338.5]	0.718	0.46	21.0	0.17		{90, 0, 180}	
CASTEP ('10) ⁵⁵	107.30 [326.8]	0.842	0.30	21.5	0.16		{270, 0, 180}	
CASTEP ('10) ⁵⁵ [Geo-opt]	94.36 [339.7]	0.745	0.49	20.8	0.19		{270, 0, 180}	
$(\text{NH}_4)_2\text{SO}_4$	334.0 \pm 0.4	0.525 \pm 0.050	0.70 \pm 0.2	-21.0 \pm 1.0	0.0 \pm 0.2		{0, 30, 20}	
CASTEP ('64) ⁴³	83.57 [350.5]	-1.914	0.53	-42.4	0.90		{90, 90, 170}	
CASTEP ('66) ⁵⁷	109.16 [324.9]	-0.569	0.25	10.9	0.84		{0, 85, 0}	
CASTEP ('10) ⁵⁸	109.82 [324.3]	-0.510	0.64	10.7	0.23		{90, 85, 0}	
α - MgSO_4	313.1 \pm 2.0	2.136 \pm 0.050	0.91 \pm 0.05	-51.5 \pm 5.0	1.0 \pm 0.2		{90, 90, 0}	
CASTEP ('07) ⁶⁰	125.33 [308.8]	-1.770	0.81	48.2	0.95		{90, 90, 180}	
CASTEP ('07) ⁶⁰ [Geo-opt]	118.81 [315.3]	-1.846	0.88	49.9	0.97		{90, 90, 180}	
β - MgSO_4	316.8 \pm 2.0	2.003 \pm 0.050	0.11 \pm 0.10	-37.6 \pm 5.0	0.0 \pm 0.2		{90, 175, 10}	
CASTEP ('07) ⁶⁰	126.88 [307.2]	-1.144	0.19	-34.3	0.04		{180, 90, 270}	
CASTEP ('07) ⁶¹	120.89 [313.2]	-1.839	0.33	-40.2	0.14		{180, 90, 185}	
CASTEP ('07) ⁶¹ [Geo-opt]	115.38 [318.7]	-1.886	0.25	-42.4	0.18		{180, 90, 185}	

NMR Parameters

Compound	$\delta_{iso}/\sigma_{iso}$ [δ_{iso}^{calc}] ^b (ppm)	C_Q (MHz)	η_Q^a	$\Delta\sigma_{aniso}^c$ (ppm)	η_{CSA}^d	$\{\alpha, \beta, \gamma\}$ (°)
CaSO ₄	326.2 ± 0.5	0.863 ± 0.050	0.49 ± 0.10	16.3 ± 4.0	0.9 ± 0.3	{90, 0, 0}
CASTEP ('64) ⁴³	101.40 [332.7]	1.175	0.07	20.8	0.83	{90, 0, 0}
CASTEP ('75) ⁴⁵	110.44 [323.7]	0.925	0.03	20.7	0.81	{90, 0, 0}
SrSO ₄	330.4 ± 1.0	1.359 ± 0.050	0.78 ± 0.10	23.7 ± 5.0	0.8 ± 0.4	{0, 10, 160}
CASTEP ('98) ⁴⁷	106.66 [327.4]	1.032	0.97	34.5	0.79	{0, 15, 90}
CASTEP ('98) ⁴⁷ [Geo-opt]	98.89 [335.2]	1.121	0.95	35.8	0.79	{0, 10, 90}
BaSO ₄	330.4 ± 2.0	1.780 ± 0.050	0.69 ± 0.05	27.9 ± 5.0	1.0 ± 0.5	{0, 10, 10}
CASTEP ('64) ⁴³	92.95 [341.2]	-0.747	0.13	38.0	0.86	{90, 35, 270}
CASTEP ('67) ⁴⁹	97.01 [337.1]	2.988	0.98	56.6	0.64	{0, 20, 90}
CASTEP ('77) ⁵⁰	107.29 [326.8]	1.807	0.57	39.9	0.90	{0, 30, 90}
CASTEP ('77) ⁵⁰ [Geo-opt]	99.82 [334.3]	1.409	0.70	41.3	0.75	{0, 3, 90}
CASTEP ('78) ⁵¹	105.54 [328.6]	1.385	0.94	41.4	0.75	{0, 10, 90}
CASTEP ('98) ⁴⁷	107.61 [326.5]	1.980	0.85	46.0	0.72	{0, 5, 90}
CASTEP ('98) ⁴⁷ [Geo-opt]	99.10 [335.0]	1.559	0.79	44.7	0.75	{0, 4, 90}
ZnSO ₄	316.9 ± 0.5	2.027 ± 0.050	0.55 ± 0.05	-56.3 ± 10.0	0.2 ± 0.5	{0, 10, 70}
CASTEP ('88) ⁵⁴	123.34 [310.8]	-1.929	0.91	-47.4	0.30	{0, 15, 90}
CASTEP ('88) ⁵⁴ [Geo-opt]	117.86 [316.2]	-1.917	0.91	-47.5	0.22	{270, 75, 180}
Al ₂ (SO ₄) ₃	280.7 ± 2.0	2.301 ± 0.050	0.55 ± 0.05	47.7 ± 10.0	0.4 ± 0.3	{150, 50, 40}
CASTEP ('93) ⁵⁶	160.36 [273.7]	-2.713	0.51	28.1	0.38	{300, 40, 20}
CASTEP ('93) ⁵⁶ [Geo-opt]	156.37 [277.7]	-2.680	0.53	27.4	0.38	{300, 40, 20}
Ga ₂ (SO ₄) ₃	291.8 ± 1.0	1.871 ± 0.050	0.69 ± 0.10	22.5 ± 5.0	0.2 ± 0.5	{20, 45, 140}
CASTEP ('95) ⁵⁹	157.95 [276.2]	-2.248	0.72	32.0	0.27	{225, 40, 330}
CASTEP ('95) ⁵⁹ [Geo-opt]	143.46 [290.6]	-1.928	0.64	30.2	0.35	{225, 35, 130}
In ₂ (SO ₄) ₃	307.7 ± 0.5	1.301 ± 0.050	0.73 ± 0.08	22.2 ± 5.0	0.7 ± 0.3	{65, 45, 140}
CASTEP ('95) ⁵⁹	143.23 [290.9]	-1.312	0.83	23.5	0.55	{40, 30, 140}
CASTEP ('95) ⁵⁹ [Geo-opt]	126.55 [307.6]	-1.320	0.90	24.0	0.66	{140, 30, 230}

^a η_Q defined as: $|V_{11} - V_{22}|/V_{33}$. ^b δ_{iso}^{calc} obtained as $\delta_{iso} = -(\sigma_{iso} - \sigma_{ref})$ with $\sigma_{ref} = 434.1$ ppm from the intercept in Figure 36

^c Chemical shielding anisotropy $\Delta\sigma_{aniso}$ from CASTEP is defined as $\Delta\sigma_{aniso} = \sigma_{33} - (\sigma_{11} + \sigma_{22})/2$. ^d Asymmetry parameter η_{CSA} in CASTEP is defined as $\eta = (\sigma_{22} - \sigma_{11})/(\sigma_{33} - \sigma_{iso})$. Principle components of the symmetric shielding tensor ordered as: $|\sigma_{33}| \geq |\sigma_{11} - \sigma_{iso}| \geq |\sigma_{22} - \sigma_{iso}|$.

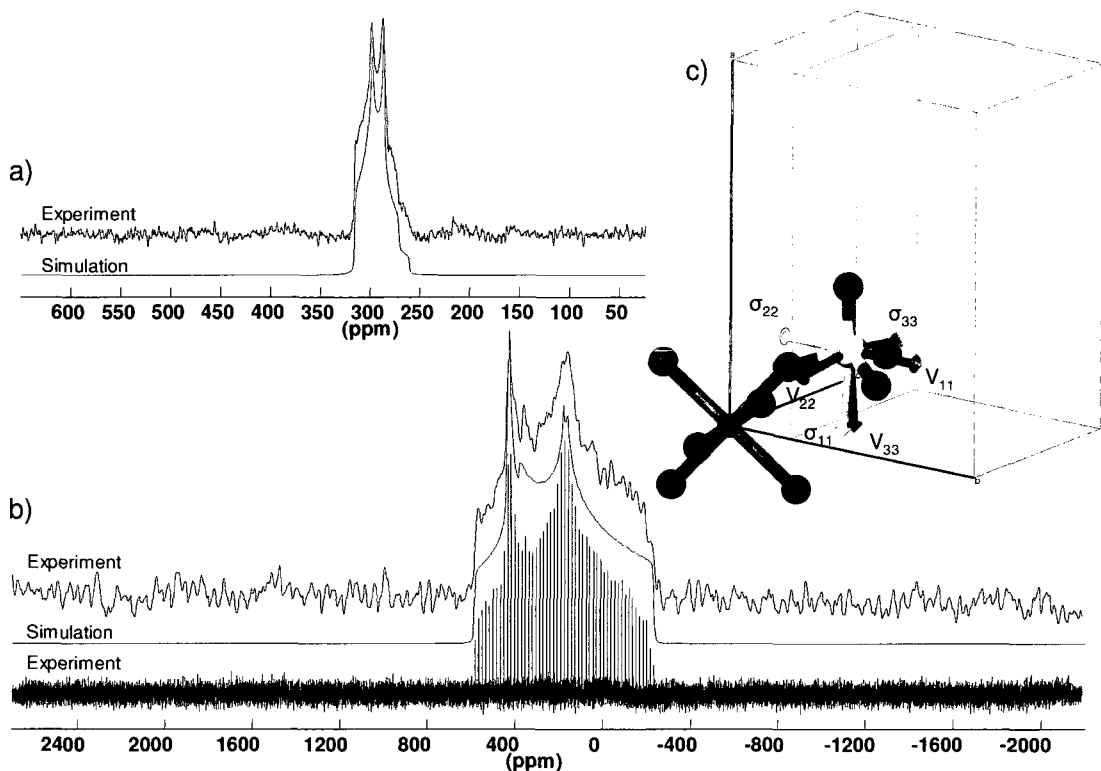


Figure 25 – ^{33}S SS-NMR spectra (experimental and simulated) for ZnSO_4 . a) 5.8 kHz RAPT-MAS Bloch Decay. b) Static QCPMG (lower) and Hahn Echo (upper). c) Representative portion of the unit cell showing the calculated orientations for the principal components of the EFG and CSA tensors. Sulfur, oxygen, and zinc are shown in yellow, red, and purple respectively. The mirror plane present through sulfur is shown in yellow.

Given the close to tetrahedral environment of the SO_4 groups in these sulfates one might not expect the quadrupolar interaction to be very big. And, looking at Figures 24 – 34, 37, and 38 or Table 7 the quadrupolar coupling interaction is not particularly strong and C_Q values are not larger than 3 MHz for the sulfates studied. The existence of an observable quadrupolar coupling interaction as well gives additional proof that the SO_4 groups are indeed not perfectly tetrahedral.¹⁷³ Unlike the Mg-containing compounds studied previously, the quadrupolar interaction does not necessarily dominate the ^{33}S spectra of the sulfates, and the effects from the CSA interaction must be considered.

Indeed, the CSA interaction is quite visible in the stationary spectra of some studied compounds, as shown in Table 7. This combination of comparable quadrupolar interactions and the CSA makes the analysis of the corresponding tensors quite interesting. Although it is difficult to measure absolute orientations of these tensors with respect to crystal structure, it is possible to examine the relative orientations between the EFG and CSA tensors, as given by the Euler angles α , β , and γ ⁸³ which rotates the EFG principle axis system into the CSA principle axis system. Experimentally determined Euler angles are given in Table 7. The calculation method used in this work does produce absolute tensor orientations and these are discussed in a later section. It should be noted that to extract reliable parameters from the experimental ³³S SS-NMR spectra of these sulfates the MAS spectrum was first analyzed via typical analytical fitting methods (see Experimental Details section) to extract the isotropic chemical shift, δ_{iso} , and quadrupolar interaction parameters, C_Q and η_Q . Then, the static spectrum obtained at 21.1 T was analyzed to extract the CSA parameters, $\Delta\sigma_{aniso}$ and η_{CSA} , as well as the Euler angles α , β , and γ . Finally, if lower field spectra were obtained a comparison between these spectra and high field spectra was done to ensure proper parameter determination.

4.3 Structural Correlation of the Shielding Interaction

Looking at Table 7 it is interesting to note that the chemical shift range of the anhydrous sulfates is quite small (~50 ppm) where the known chemical shift range of ³³S is around 1000 ppm.¹⁸² Therefore, to extend the range of the shielding-shift relationship for this study, the isotropic chemical shifts of a few well known cubic sulfides³⁵ along

with subsequent first principles calculations were added to get an accurate determination of the calculation-experiment relation for ^{33}S as a whole. The experimental and calculated data for these sulfides can be seen in Table 8.

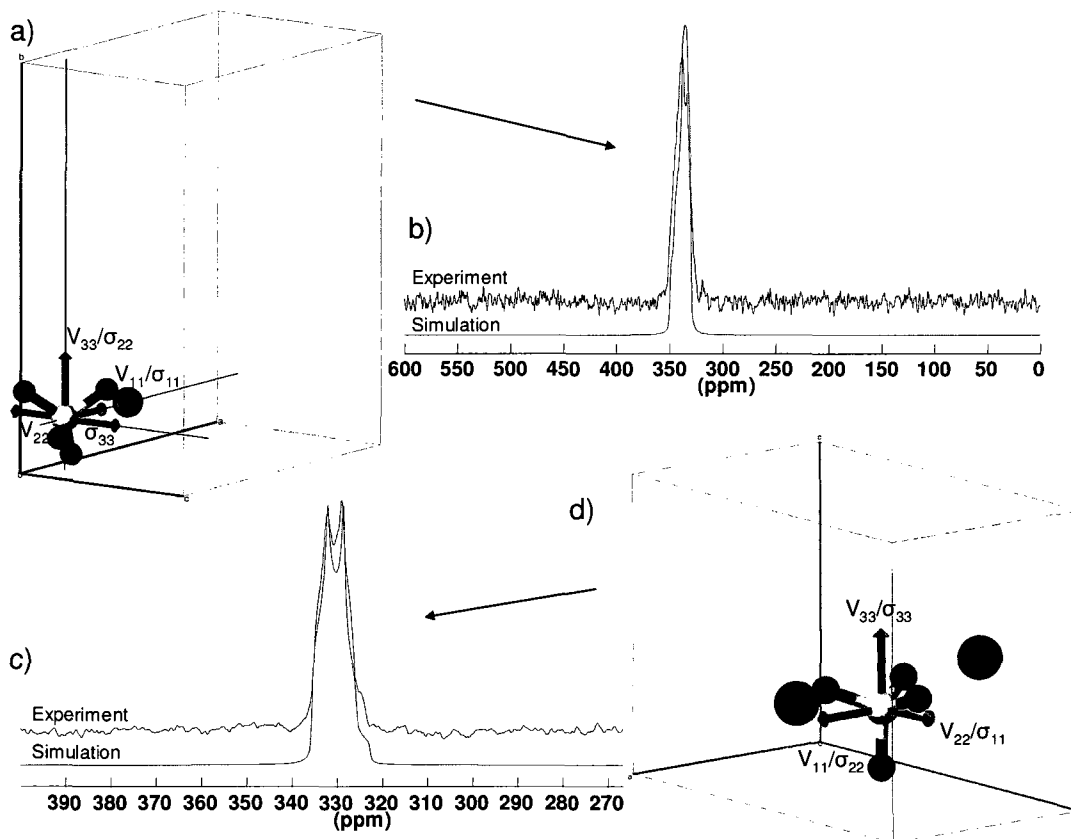


Figure 26 – a) Representative portion of the Na_2SO_4 unit cell showing the calculated orientations for the principal components of the EFG and CSA tensors. The black lines are proper C2 rotation axes present through sulfur. b) Static Hahn Echo ^{33}S SS-NMR spectrum (experimental and simulated) of Na_2SO_4 . c) 5 kHz MAS Bloch Decay ^{33}S SS-NMR spectrum (experimental and simulated) of K_2SO_4 . d) Representative portion of the K_2SO_4 unit cell showing the calculated orientations for the principal components of the EFG and CSA tensors. Sulfur, oxygen, and alkali metal are shown in yellow, red, and purple respectively. The mirror plane present through sulfur is shown in yellow.

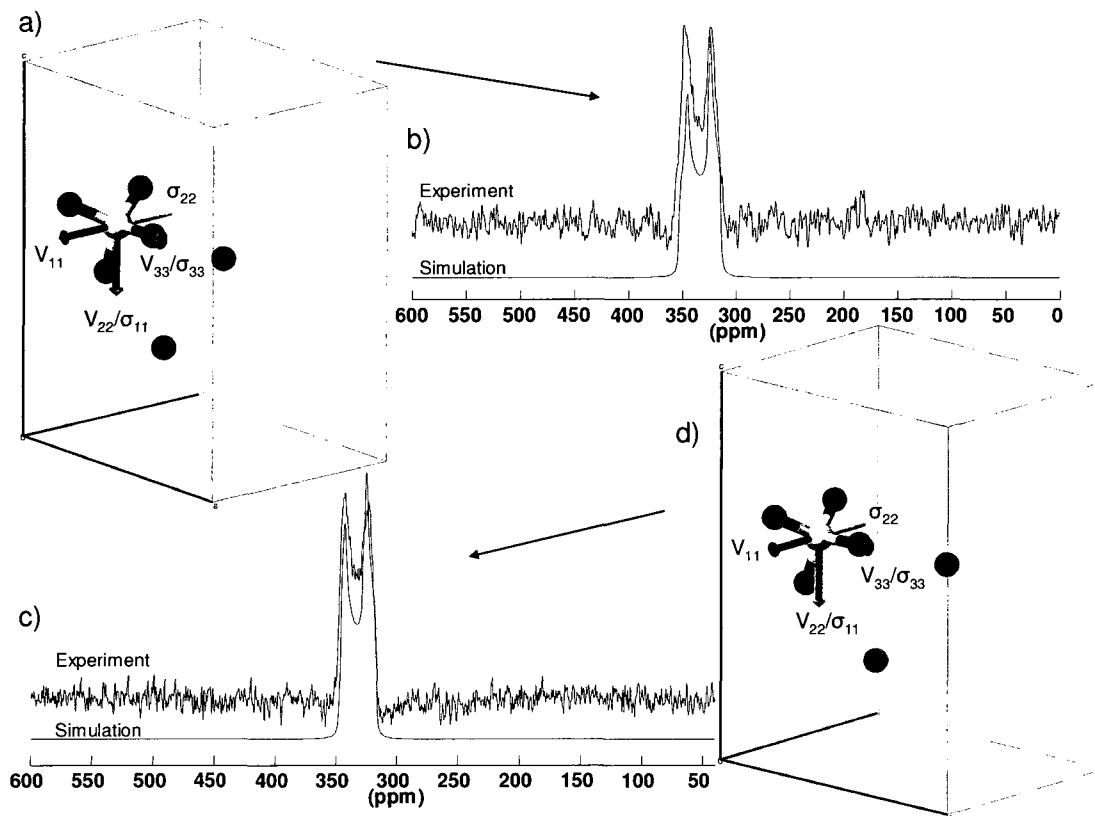


Figure 27 – a) Representative portion of the Rb_2SO_4 unit cell showing the calculated orientations for the principal components of the EFG and CSA tensors. Sulfur, oxygen, and alkali metal are shown in yellow, red, and purple respectively. The mirror plane present through sulfur is shown in yellow. b) Static Hahn Echo ^{33}S SS-NMR spectrum (experimental and simulated) of Rb_2SO_4 . c) Static Hahn Echo ^{33}S SS-NMR spectrum (experimental and simulated) of Cs_2SO_4 . d) Similar to a) but for Cs_2SO_4 .

Looking at the experimental results of the shielding interaction several interesting trends can be seen. Firstly, the signals of the alkali metal anhydrous sulfates are the least shielded with δ_{iso} ranging from about 330 ppm to 340 ppm. The alkali earth metal and dicationic sulfates have a δ_{iso} range from about 310 ppm to 330 ppm. The Group 13 cation sulfates, $\text{Al}_2(\text{SO}_4)_3$, $\text{Ga}_2(\text{SO}_4)_3$, and $\text{In}_2(\text{SO}_4)_3$ (Figures 28-30), however, have the most shielded ^{33}S environments with δ_{iso} from about 310 ppm to 280 ppm. One can further look at the isotropic chemical shift trend of ^{33}S in sulfates with cations from the same Group. Even though the shift range is quite small, one can still see a visible trend.

For example, looking first at the Group 13 sulfates it can be seen that $\text{Al}_2(\text{SO}_4)_3$ has the most shielded ^{33}S site ($\delta_{iso} = 281.7$ ppm) and $\text{In}_2(\text{SO}_4)_3$ has the least shielded ^{33}S site ($\delta_{iso} = 307.7$ ppm). Although less pronounced, this trend is also visible with alkali and alkali earth metal sulfates. For example, both α and β - MgSO_4 have more shielded ^{33}S sites ($\delta_{iso} = 313.1$ ppm and 316.8 ppm respectively), yet BaSO_4 has the most deshielded ^{33}S site (330.4 ppm) (Figure 38). The trend is somewhat difficult to analyze for the alkali metal sulfates within experimental error given the small shift range, but it is interesting to note that Li_2SO_4 has the most shielded ^{33}S site ($\delta_{iso} = 331.4$ ppm). There are some interesting cases that do not necessarily fit into a particular subgroup. ZnSO_4 (Figure 25), for example, is not an alkali earth metal sulfate, yet the isotropic chemical shift for ^{33}S is similar to that of MgSO_4 (Figures 31, 32). If one examines, though, the ionic radius of Zn^{2+} , it can be seen that it is very similar to that of Mg^{2+} .¹⁸³ These differences and similarities in ionic radius of the cation may possibly explain the differences in isotropic chemical shift of ^{33}S in these sulfates. The relationship is certainly not expected to be linear, however, an increase in ionic radius of cation of the same valence, in general, seems to cause a decrease in isotropic chemical shielding. As well, if one examines $(\text{NH}_4)_2\text{SO}_4$ (Figure 34) one can see that the ^{33}S isotropic chemical shift is in between that of Li_2SO_4 and Rb_2SO_4 (Figures 27, 33 and Table 7). And, it has been shown that when treated as a single univalent cation, the ionic radius of NH_4^+ is in between that of Li^+ and Rb^+ .^{183, 184} Thus, this compound also seems to follow this trend. It is interesting, however, to note that Na_2SO_4 does not follow this trend and exhibits the least shielded sulfur site of all the alkali metal sulfates (Figure 26). This shows that merely using differences in ionic radius to make assumptions about the isotropic chemical shift of ^{33}S is not sufficient.

However, at the very least, one can make an assumption about the oxidation state of a given cation on the basis of the isotropic chemical shift for ^{33}S in anhydrous sulfates.

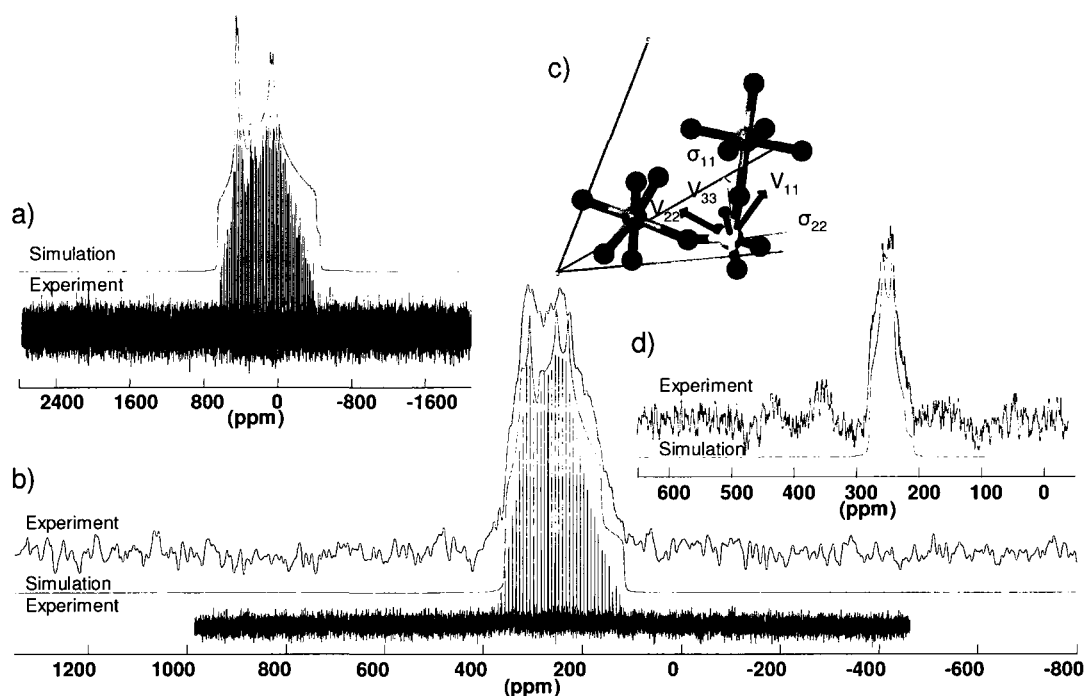


Figure 28 – ^{33}S SS-NMR spectra (experimental and simulated) of $\text{Al}_2(\text{SO}_4)_3$. a) Static QCPMG taken at 9.4 T ($\nu_0(^{33}\text{S}) = 30.7$ MHz). b) Static QCPMG (lower) and Hahn Echo (upper) taken at 21.1 T ($\nu_0(^{33}\text{S}) = 69.1$ MHz). c) Representative portion of the unit cell showing the calculated orientations for the principal components of the EFG and CSA tensors. Sulfur, oxygen, and aluminum are shown in yellow, red, and brown respectively. d) 5.8 kHz RAPT-MAS Bloch Decay.

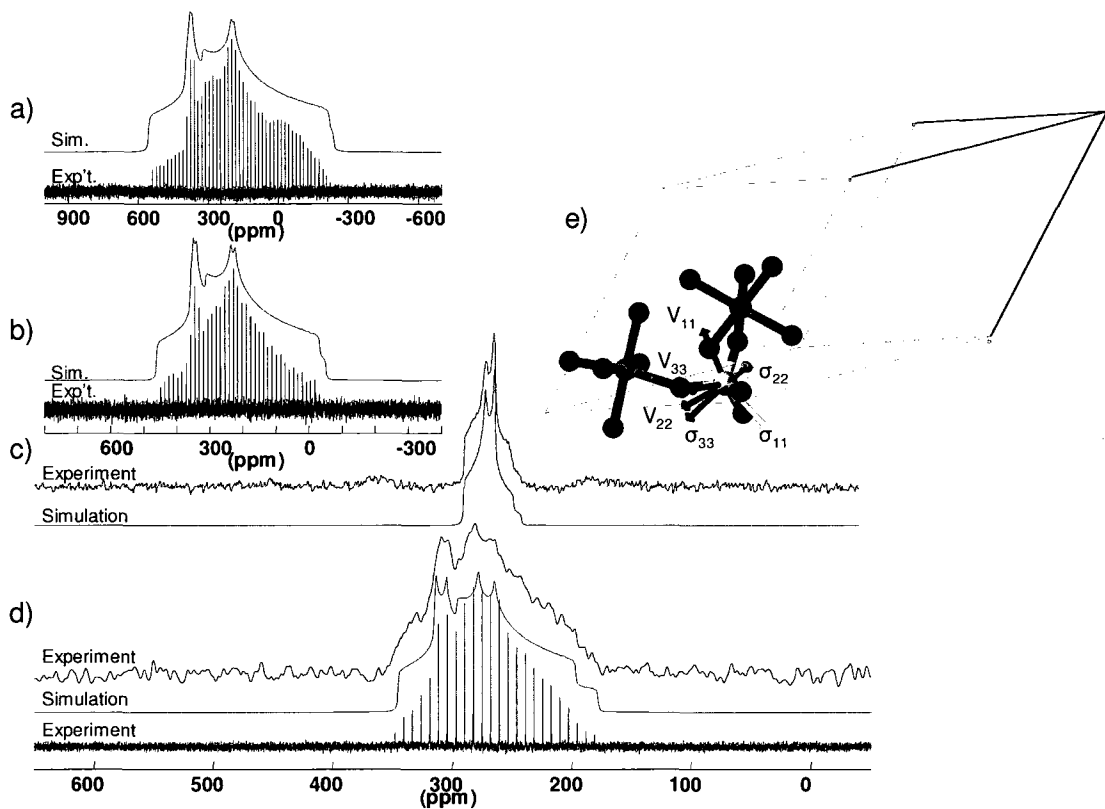


Figure 29 – ^{33}S SS-NMR spectra (experimental and simulated) of $\text{Ga}_2(\text{SO}_4)_3$. a) Static QCPMG taken at 9.4 T ($\nu_0(^{33}\text{S}) = 30.7$ MHz). b) Static QCPMG taken at 11.7 T ($\nu_0(^{33}\text{S}) = 38.4$ MHz). c) 5.8 kHz RAPT-MAS Bloch Decay. d) Static QCPMG (lower) and Hahn Echo (upper) taken at 21.1 T ($\nu_0(^{33}\text{S}) = 69.1$ MHz). e) Representative portion of the unit cell showing the calculated orientations for the principal components of the EFG and CSA tensors. Sulfur, oxygen, and gallium are shown in yellow, red, and brown respectively.

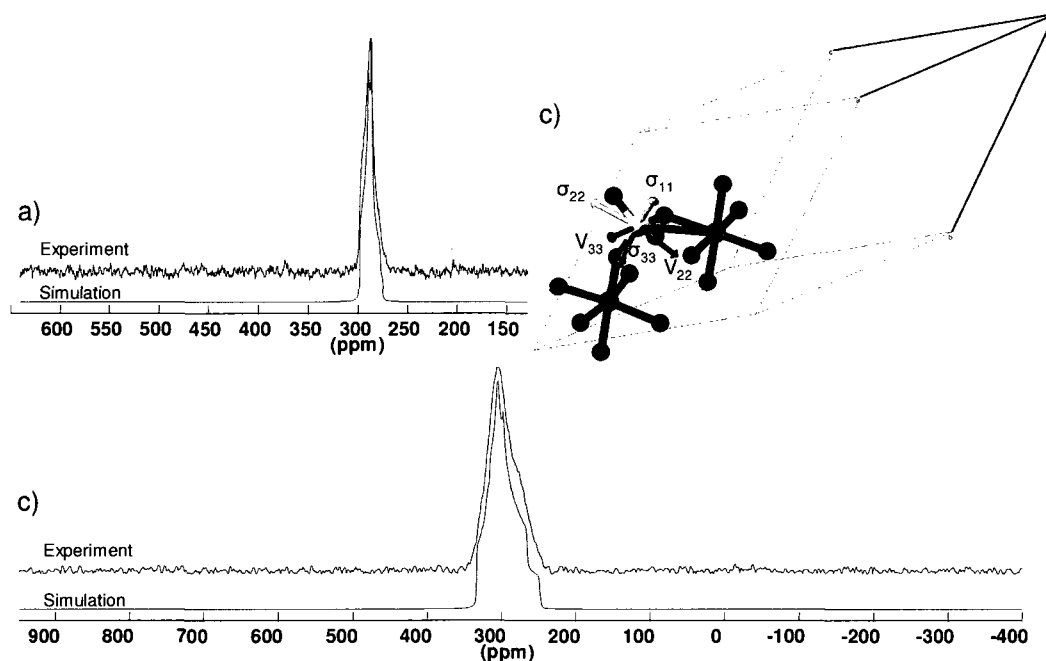


Figure 30 – ^{33}S SS-NMR spectra (experimental and simulated) of $\text{In}_2(\text{SO}_4)_3$. a) 5.8 kHz RAPT-MAS Bloch Decay. b) Static Hahn Echo. c) Representative portion of the unit cell showing the calculated orientations for the principal components of the EFG and CSA tensors. Sulfur, oxygen, and indium are shown in yellow, red, and brown respectively.

From Table 7 it can be seen that, unlike in the case of ^{25}Mg , the anisotropic part of the shielding interaction is not negligible and contributes measurably to the static spectra. The contribution from the CSA interaction is not extremely large, but of the same order as the quadrupolar interaction and, as such, cannot be ignored. Unlike the clearly visible trends in the isotropic chemical shift, it is difficult to ascertain any possible trends within the anisotropic part of the shielding interaction. The one potentially interesting observation made from the chemical shielding anisotropy parameter for all the sulfates was that the $\Delta\sigma_{aniso}$ for the alkali metal sulfates was smaller than for the other sulfates studied. Although this effect is slight, it is visible from Table 7 and Figures 26, 27 and 33 that the effect of CSA on the NMR spectrum of the alkali metal sulfates is smaller with $\Delta\sigma_{aniso} = 10.6 \pm 2.0$ ppm for Cs_2SO_4 being the smallest recorded shielding anisotropy

(Table 7 and Figure 27). Although, this is where the possible trend stops, as the largest value of shielding anisotropy comes from ^{33}S in ZnSO_4 with $\Delta\sigma_{aniso} = -56.3 \pm 10.0$ ppm, a divalent cation sulfate, and the other anisotropy values for the other sulfates are very similar in magnitude, within experimental error. It is also interesting to examine the effect that symmetry at the sulfur site might have on the anisotropic part of the shielding interaction. Interestingly, due to the low degree of symmetry at the sulfur site in the majority of these compounds (Table 6), the three principal components of the shielding interaction should be independent,¹⁷² thereby not restricting $\eta_{CSA} = 0$. However, Na_2SO_4 with D_2 symmetry at the sulfur site should indeed have what one might think of as an axially symmetric shielding tensor with $\eta_{CSA} = 0$ as dictated by symmetry. And, within experimental error, this is what is experimentally observed for ^{33}S in Na_2SO_4 (Figure 26). There are a few other compounds, such as $(\text{NH}_4)_2\text{SO}_4$, and $\beta\text{-MgSO}_4$, which have an axially symmetric shielding tensor for ^{33}S , however, this is not a symmetry-dictated restriction.

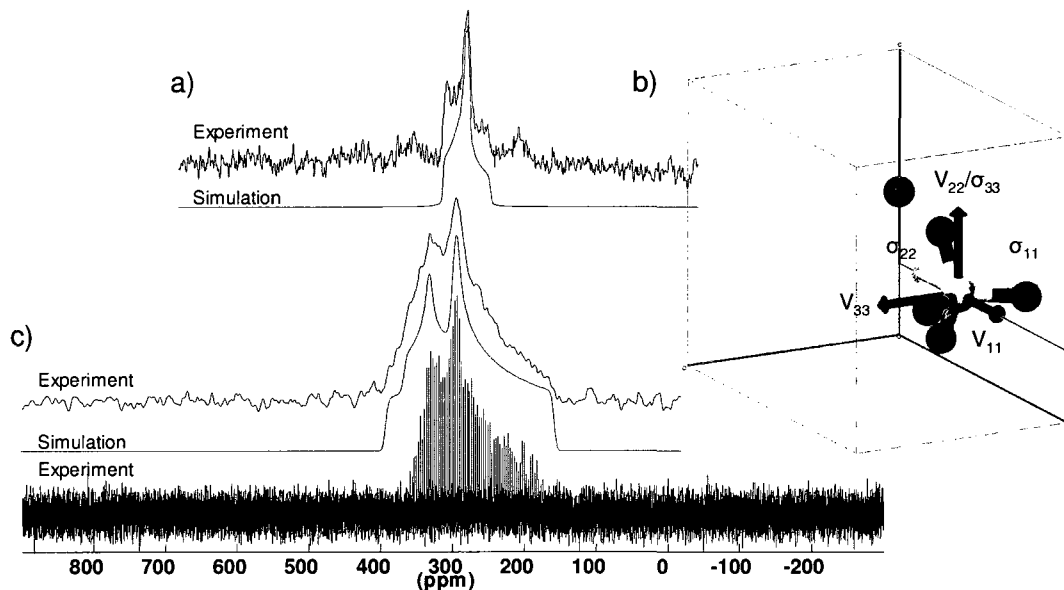


Figure 31 – ^{33}S SS-NMR spectra (experimental and simulated) of $\alpha\text{-MgSO}_4$. a) 5 kHz MAS Bloch Decay. b) Representative portion of the unit cell showing the calculated orientations for the principal components of the EFG and CSA tensors. Sulfur, oxygen, and alkali earth metal are shown in yellow, red, and green respectively. The two mirror planes present through sulfur are shown in yellow. The black line at the intersection of the planes is the proper C2 rotation axis through sulfur. c) Static QCPMG (lower) and Hahn Echo (upper).

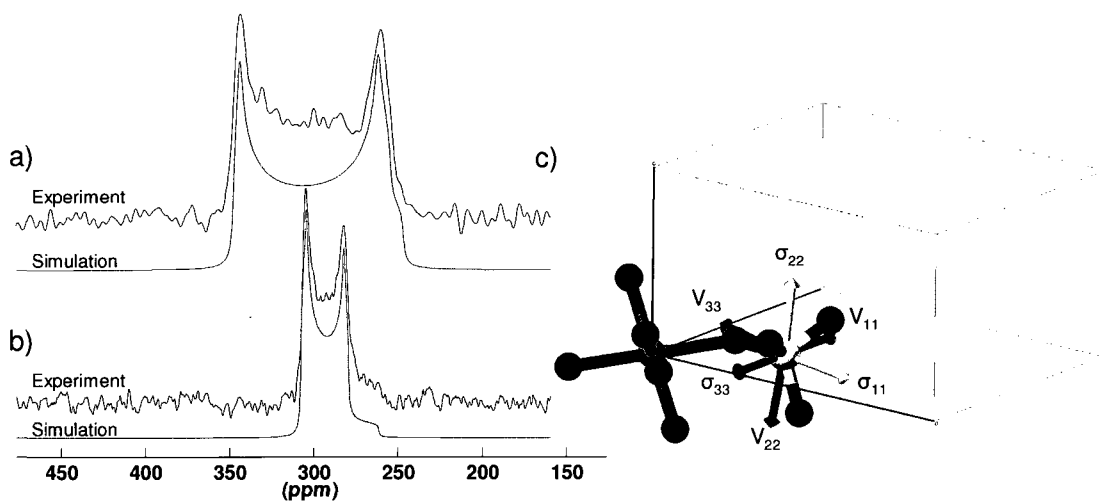


Figure 32 – ^{33}S SS-NMR spectra (experimental and simulated) of $\beta\text{-MgSO}_4$. a) Static Hahn Echo. b) 5 kHz MAS Bloch Decay. c) Representative portion of the unit cell showing the calculated orientations for the principal components of the EFG and CSA tensors. Sulfur, oxygen, and alkali earth metal are shown in yellow, red, and green respectively. The mirror plane present through sulfur is shown in yellow.

The agreement between calculated and experimental parameters for the anisotropic part of the shielding interaction is fair, on the whole. As seen in Table 7, the calculated anisotropy, $\Delta\sigma_{aniso}$ and asymmetry parameter, η_{CSA} , are within the same order of magnitude as the experimental values. However, the experimental error is too large to make any definite conclusions about the accuracy of calculated anisotropy in the studied sulfates. Some seemingly large disagreements may be merely due to the fact that the calculated and measured quantities are, on the whole, quite small. So, minute changes in the predicted values for the principal components of the shielding interaction will produce seemingly large disagreements in the resulting $\Delta\sigma_{aniso}$ and η_{CSA} .

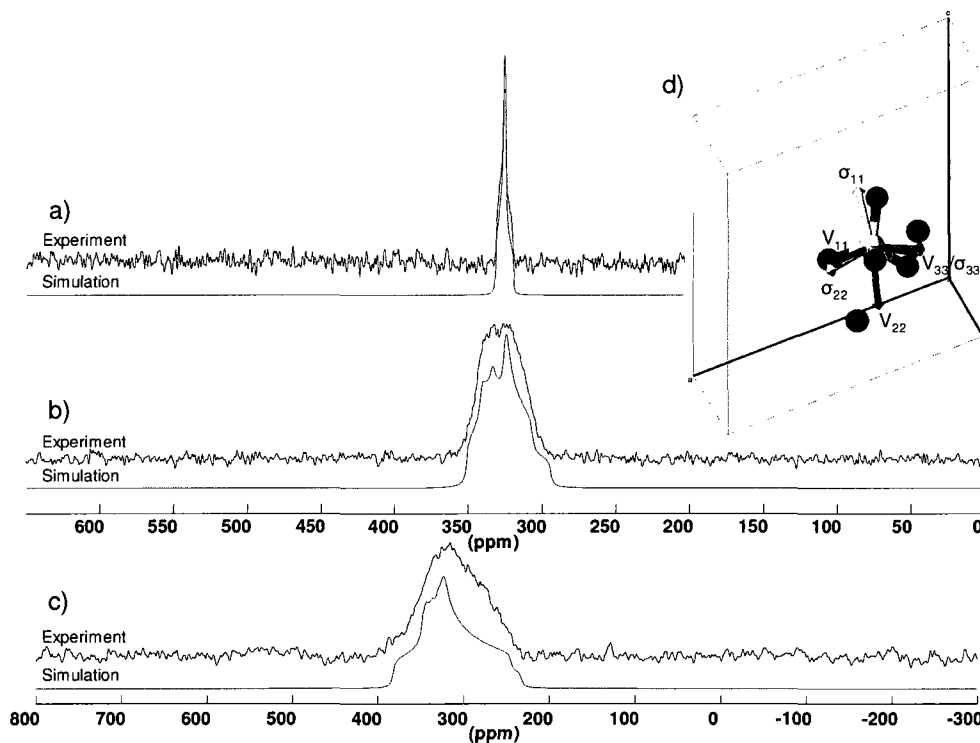


Figure 33 – ^{33}S SS-NMR spectra (experimental and simulated) of Li_2SO_4 . a) 5 kHz MAS Bloch Decay taken at 21.1 T ($\nu_0(^{33}\text{S}) = 69.1$ MHz). b) Static Hahn Echo taken at 21.1 T ($\nu_0(^{33}\text{S}) = 69.1$ MHz). c) Static Hahn Echo taken at 11.7 T ($\nu_0(^{33}\text{S}) = 38.4$ MHz). d) Representative portion of the unit cell showing the calculated orientations for the principal components of the EFG and CSA tensors. Sulfur, oxygen, and alkali metal are shown in yellow, red, and purple respectively.

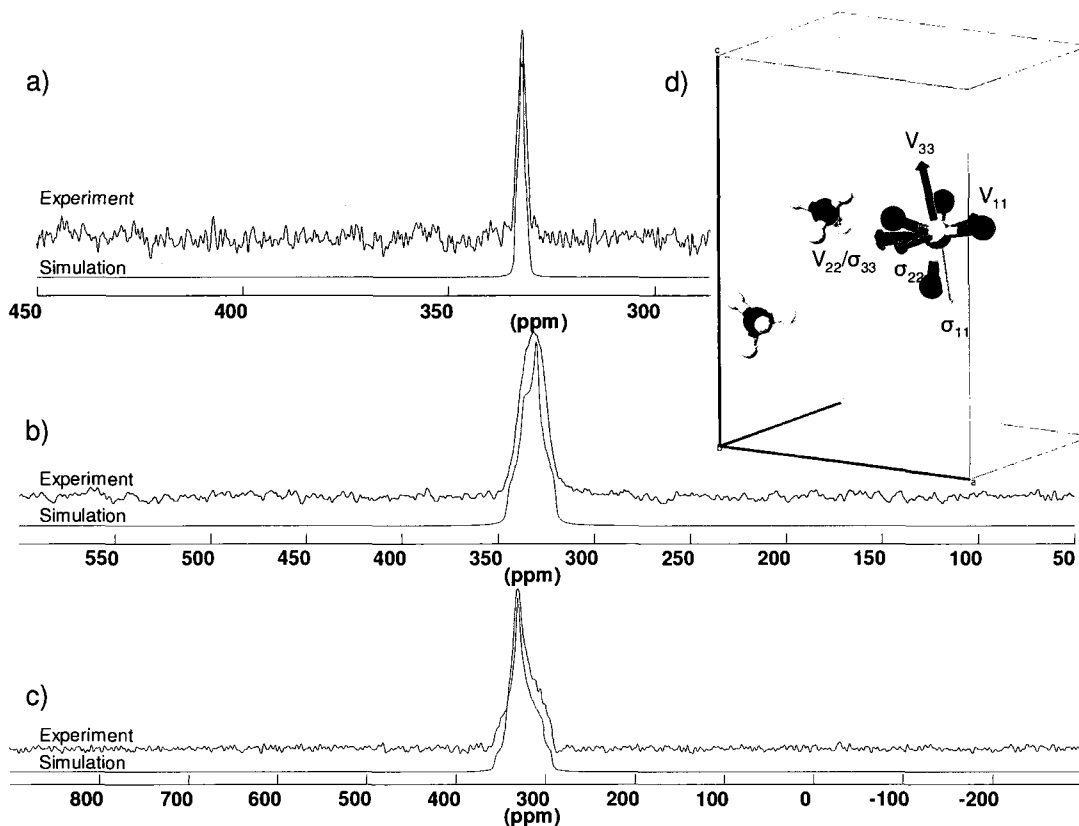


Figure 34 – ^{33}S SS-NMR spectra (experimental and simulated) of $(\text{NH}_4)_2\text{SO}_4$. a) 5 kHz MAS Bloch Decay taken at 21.1 T ($\nu_0(^{33}\text{S}) = 69.1$ MHz). b) Static Hahn Echo taken at 21.1 T ($\nu_0(^{33}\text{S}) = 69.1$ MHz). c) Static Hahn Echo taken at 9.4 T ($\nu_0(^{33}\text{S}) = 30.7$ MHz). d) Representative portion of the unit cell showing the calculated orientations for the principal components of the EFG and CSA tensors. Sulfur, oxygen, nitrogen and hydrogen are shown in yellow, red, blue and white respectively. The mirror plane present through sulfur is shown in yellow.

The correlation of the calculated isotropic shielding, σ_{iso} , and isotropic chemical shift, δ_{iso} , however, is quite distinct. One of the main goals of this ^{33}S study is to evaluate the accuracy of the multiple reported crystal structures of a given anhydrous sulfate through the first principles calculations. As just noted, the anisotropic components of the shielding interaction proved not to be very reliable parameters for picking out crystal structures by comparing calculated and experimental values given the large degree of variability. The isotropic chemical shift, on the other hand, can be determined with

greater accuracy, and by comparing them to the calculated shielding, it may be useful for evaluating structural variations. Figure 35 shows the correlation between the experimental isotropic chemical shift and the calculated isotropic chemical shielding for the studied anhydrous sulfates. One can see that for a given sulfate, there are multiple calculated absolute shielding values. These values are obtained from the variety of known structures for each sulfate. If the calculations are accurate, the calculated absolute shielding versus experimental chemical shift should yield a linear 1:1 correlation. Since the chemical shift range for the anhydrous sulfates is generally quite narrow, it is difficult to evaluate which structure is the most accurate from isotropic shielding data alone. So, by using calculated and experimental quadrupolar parameters (next section), other nuclei, and calculated/experimental ^{33}S SS-NMR data for some well known sulfide materials (Table 8) a more reliable chemical shift versus shielding relationship was developed (Figure 36). The sulfides were chosen because they exist in a purely cubic form resulting in absence of the CSA and quadrupolar interaction producing very accurate isotropic chemical shifts for these compounds.

Table 8 – Experimental and calculated ^{33}S NMR parameters for sulfides used in shielding correlation (Figure 36).^{33, 35}

Compound	Experimental δ_{iso} (ppm)	Calculated σ_{iso} [$\delta_{\text{iso}}^{\text{calc}}$] (ppm)
Li_2S	-343.9	803.57 [-369.5]
Na_2S	-339.5	780.46 [-346.4]
CaS	-29.1	354.84 [79.3]
SrS	43.5	328.97 [105.1]
CdS	-284	727.26 [-293.2]
PbS	-292.4	788.50 [-354.4]

The final relationship between calculated isotropic chemical shielding and isotropic chemical shift are shown Figure 35 (only sulfates shown) and Figure 36 (sulfates and

sulfides included). It is easy to see that some of the structures used in the calculations produced results that deviate from the 1:1 correlation well in excess of the experimental errors (Figure 35, red points). These structures were rendered as less accurate and were not included in the final fit. The line of best fit resulting from the data in Figure 36 gives a relationship of $\sigma_{iso} = -1.012 (\pm 0.028) \cdot \delta_{iso} + 434.1 (\pm 8.6)$ with a regression factor of 0.986. This relationship, with deviations smaller than 4%, again, shows the reliability of CASTEP calculated shielding constants.

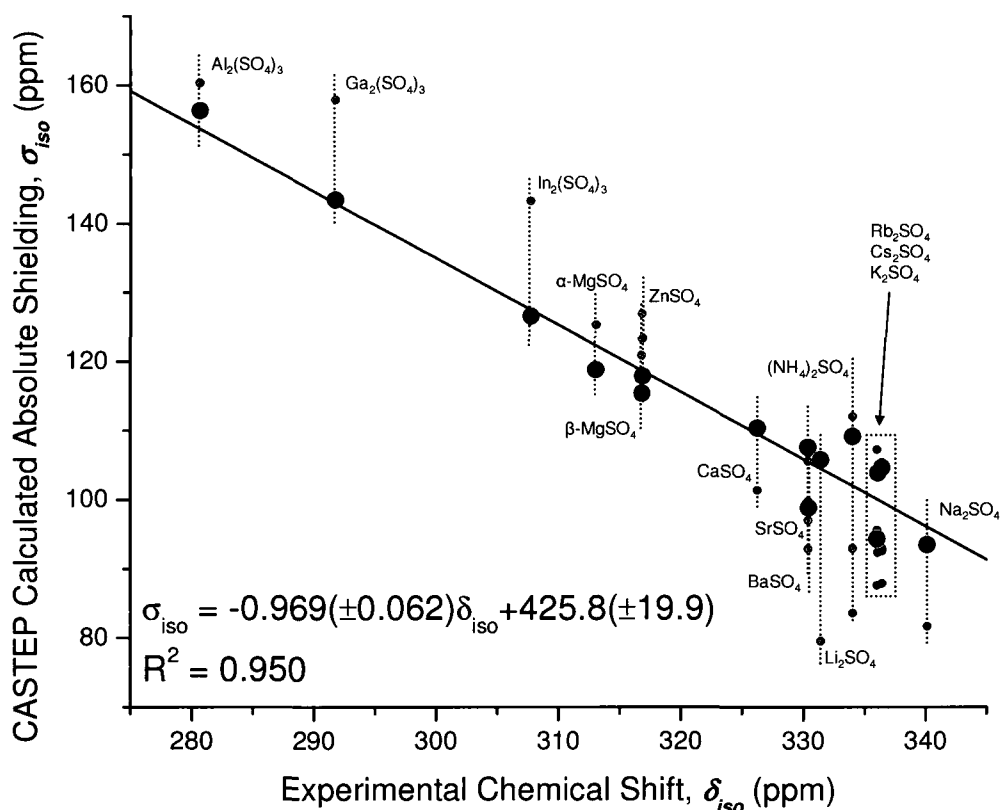


Figure 35 - Correlation between ^{33}S experimentally determined chemical shift and calculated absolute shielding as determined by CASTEP for all sulfates compounds studied. Line of best fit is shown merely to reflect the excellent agreement and almost 1:1 correlation. See Figure 36 for full shielding-shift correlation. The red points represent calculations for structures that produced the largest disagreement with experiment. (see Table 7).

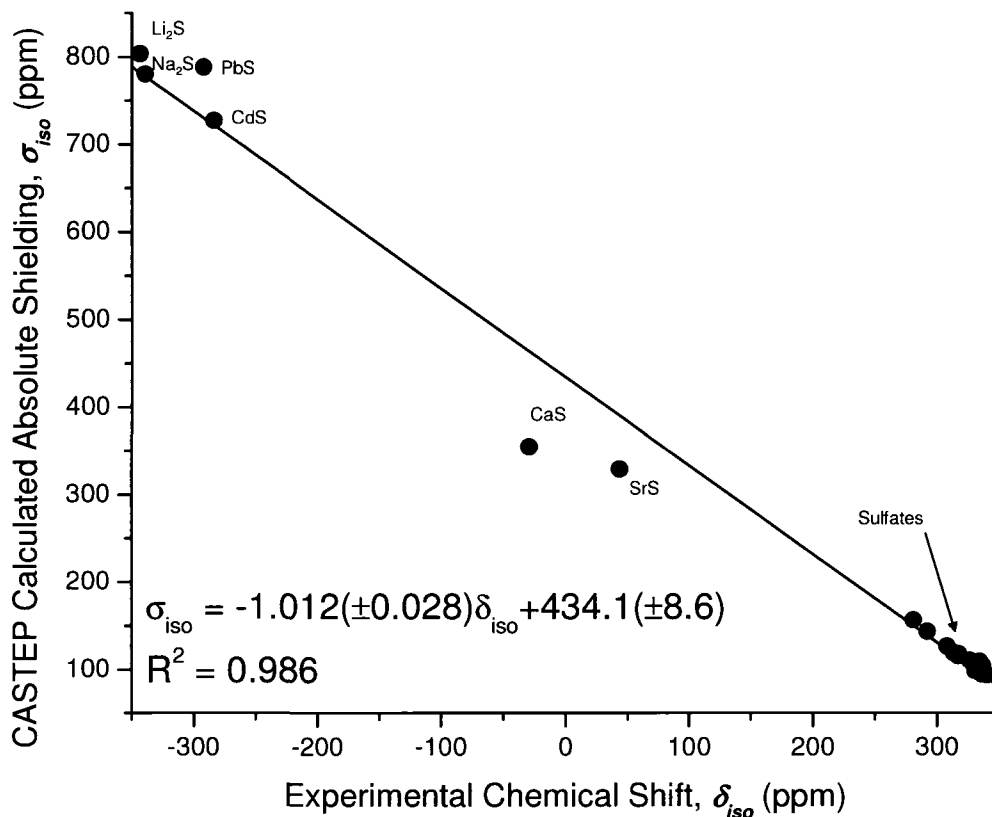


Figure 36 – Full shielding correlation between ³³S experimentally determined chemical shift and calculated absolute shielding as determined by CASTEP for all sulfate and sulfide compounds. Line of best fit is shown.

4.4 Structural Correlation of the Quadrupolar Interaction

The trend for the quadrupolar interaction in the studied sulfates is not as obvious as in the case of the shielding. It can generally be said that for anhydrous sulfates, the quadrupolar coupling constant, C_Q , ranges between ~ 0.5 MHz to ~ 2.5 MHz for all sulfates, and none of them show a $C_Q = 0$ MHz. More specifically though, in terms of type of cation, it can be said that the univalent cation alkali metal sulfates have a smaller quadrupolar interaction with $C_Q < 1$ MHz. However, there is no distinct division between

sulfates of divalent and trivalent cations and, in fact, CaSO_4 has a C_Q value similar to that of the alkali metal sulfates ($C_Q = 0.863$ MHz) (Figure 37). Even within the groups of alkali and alkali earth metals there does not appear to be an overall trend in ^{33}S C_Q 's at the sulfur site. Interestingly enough, the smaller and harder cations (Mg and Zn) produce the largest C_Q 's for ^{33}S . The sulfates of trivalent Group 13 metals, however, do show a slight trend in the quadrupolar interaction, where $\text{Al}_2(\text{SO}_4)_3$ shows the largest $C_Q = 2.286$ MHz and $\text{In}_2(\text{SO}_4)_3$ shows the smallest $C_Q = 1.301$ MHz among the Group 13 sulfates. This may be partially explained by noting that Al^{3+} is smaller and harder than In^{3+} resulting in larger electric field gradients felt at the sulfur site. This explanation is only qualitative, nevertheless it is still visible that the nature of the cation greatly influences the EFG at the sulfur centre in all these sulfate materials.

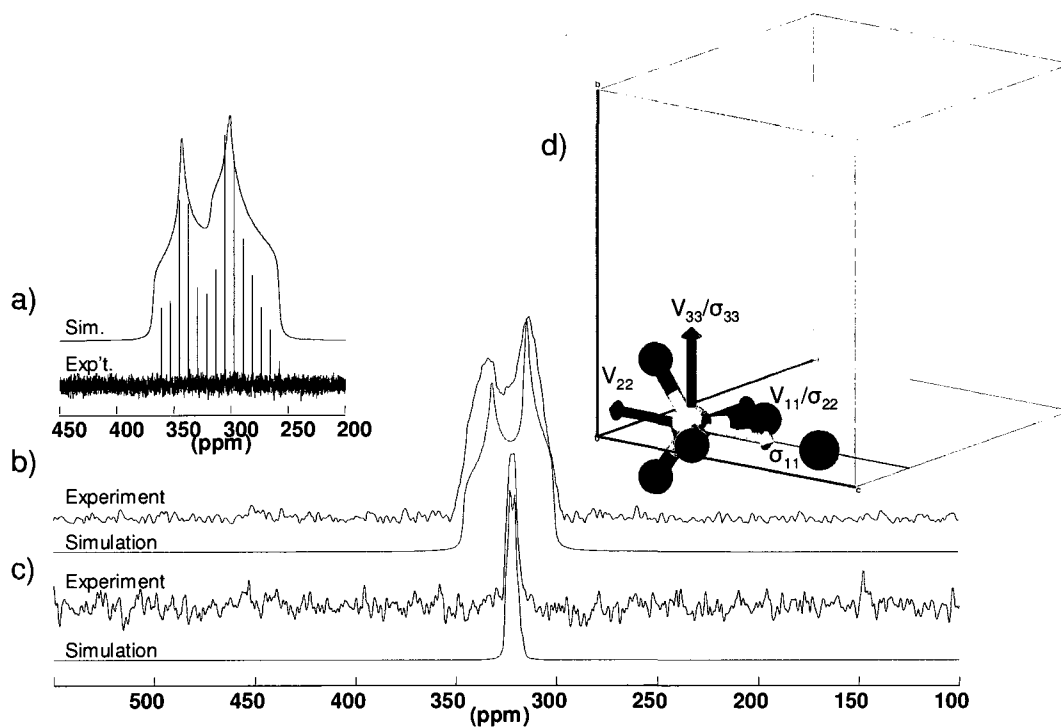


Figure 37 – ^{33}S SS-NMR spectra (experimental and simulated) of CaSO_4 . a) Static QCPMG taken at 11.7 T ($\nu_0(^{33}\text{S}) = 38.4$ MHz). b) Static Hahn Echo taken at 21.1 T ($\nu_0(^{33}\text{S}) = 69.1$ MHz). c) 5 kHz MAS Bloch Decay taken at 21.1 T ($\nu_0(^{33}\text{S}) = 69.1$ MHz). d) Representative portion of the unit cell showing the calculated orientations for the principal components of the EFG and CSA tensors. Sulfur, oxygen, and alkali earth metal are shown in yellow, red, and green respectively. The two mirror planes present through sulfur are shown in yellow. The black line at the intersection of the planes is the proper C2 rotation axis through sulfur.

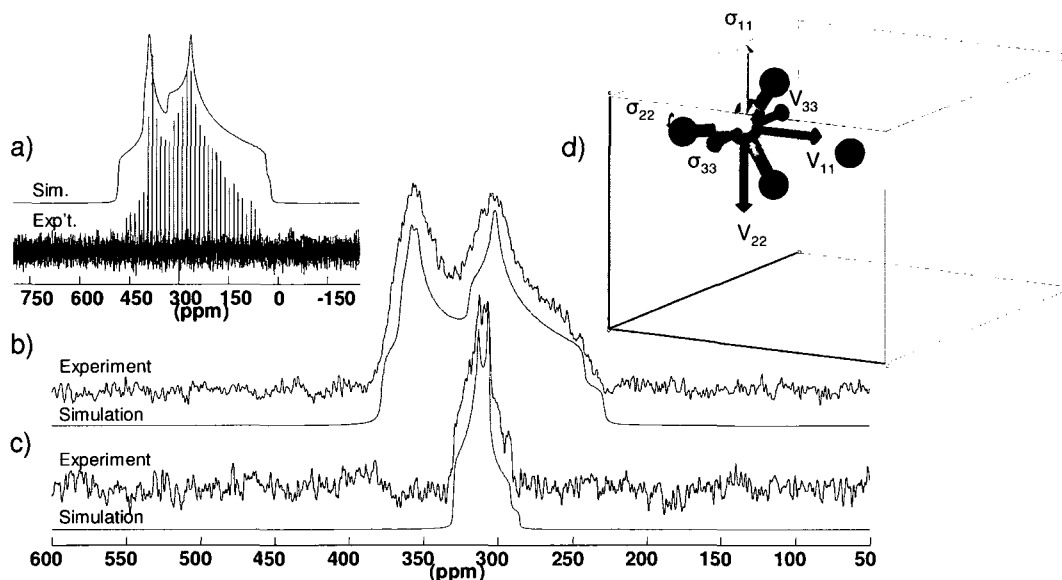


Figure 38 – ^{33}S SS-NMR spectra (experimental and simulated) of BaSO_4 . a) Static QCPMG taken at 11.7 T ($\nu_0(^{33}\text{S}) = 38.4$ MHz). b) Static Hahn Echo taken at 21.1 T ($\nu_0(^{33}\text{S}) = 69.1$ MHz). c) 5 kHz MAS Bloch Decay at 21.1 T ($\nu_0(^{33}\text{S}) = 69.1$ MHz). d) Representative portion of the unit cell showing the calculated orientations for the principal components of the EFG and CSA tensors. Sulfur, oxygen, and barium are shown in yellow, red, and green respectively. The mirror plane present through sulfur is shown in yellow.

It is also interesting that the experimentally determined quadrupolar asymmetry parameter, η_Q , for all sulfates, in general, was not representative of either an axially symmetric EFG tensor with $\eta_Q = 0.0$ or completely asymmetric with $\eta_Q = 1.0$ (Table 7). This is an indication for the relatively low symmetry present at the sulfur site in these sulfate materials. Only Na_2SO_4 , with a D_2 point group at the sulfur site showed a perfectly axially symmetric EFG tensor (Figure 26). This is also reflected in the calculated quadrupolar asymmetry parameter, where an axially symmetric tensor was not predicted for any of the compounds studied. However, in general, for all the sulfates studied, the agreement between calculated and experimental η_Q was not statistically accurate, however, this is not surprising given the definition of the asymmetry parameter.

Similar to the isotropic chemical shielding, the calculated quadrupolar coupling constants were, in general, in good agreement with the experimentally obtained data. As such, the correlation between the calculated C_Q and the experimentally determined C_Q could be used as another parameter for making structural assessments of these sulfates materials. The correlation between calculated C_Q and experimental C_Q is again 1:1, and in this case the values can be compared directly, unlike the isotropic shielding/chemical shift. Figure 39 shows the correlation between experimental C_Q and calculated C_Q for all the sulfates studied. The red points indicate the same structures as in Figure 35 that do not reproduce accurately calculated parameters. The correlation between experiment and calculation was found to be $C_Q^{calc} = 1.002 (\pm 0.029) \cdot C_Q$ with a regression factor of 0.930. Again, the very small deviation from unity of the correlation line slope for the calculated C_Q shows the excellent reliability of CASTEP calculated NMR parameters.

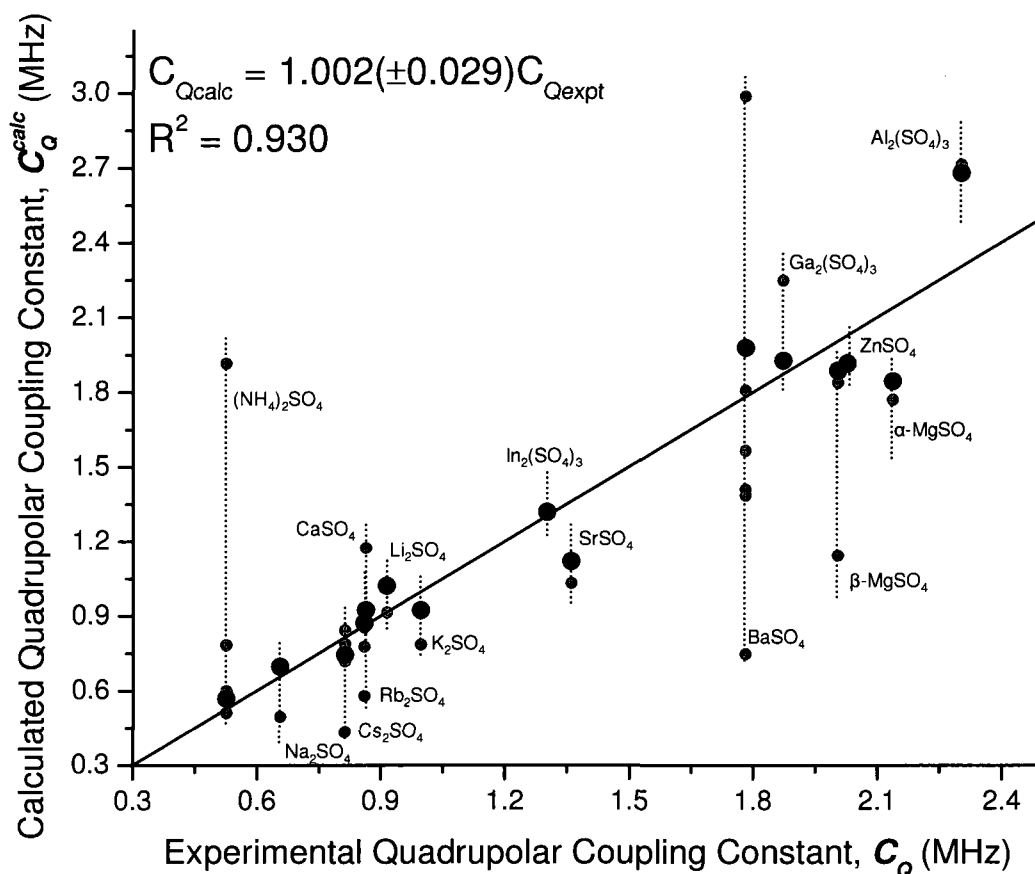


Figure 39 - Correlation between ^{33}S experimentally determined quadrupolar coupling constant, C_Q , and the calculated quadrupolar coupling constant, C_Q^{calc} , as determined by CASTEP for all sulfate compounds studied. Line of best fit is shown.

4.5 Structural Assessment via Solid State NMR and First Principles Calculations

To start the structural assessment of the sulfates, the correlation between calculated isotropic shielding and experimental isotropic shift is observed for all sulfates and the sulfides (similar to Figure 36) to get a rough estimate of the absolute shielding value for a chemical shift of zero (or the y-intercept). Then, a 1:1 correlation with the

given y-intercept is overlaid onto the shielding/shift data for the sulfates studied. From this estimate, the structures producing the best agreement between calculated and experimental results were chosen producing the relation shown in Figure 36. However, given the relatively limited chemical shift range for these sulfates, using calculated shielding data alone was not always sufficient to make accurate structural assessments. Using additional parameters should improve accuracy and exclude the possibility of random coincidence. The calculated and experimental quadrupolar coupling constant was also used as an evaluation parameter. The use of C_Q is particularly convenient, since the calculations and the experiment can be compared directly. The combination of isotropic shielding and quadrupolar coupling constant, in most cases, was sufficient to make a structural assessment. It should be noted that some structures of the same material produced parameters that did not deviate from each other within experimental error. For these cases the most recently available structure was chosen for the various fits.

Consequently, from Figures 35, 36 and 39 and Table 7, a single reported crystal structure for each sulfate was chosen to produce the fit relationships for isotropic chemical shift/shielding and the quadrupolar coupling constants. Not unexpectedly, the most accurate calculated NMR parameters came from the most recently reported structure in all cases. This generally makes sense for several reasons. One reason being that the experimental X-ray reflection data collected for some of the older structures was taken at temperatures lower than room temperature. This has the effect of reducing noise in the patterns collected, but ultimately will not necessarily reflect the overall structure observed at room temperature. This, of course, is important as all NMR experiments are

performed at room temperature. The other reason being simply technological improvements and more attention to detail in pattern acquisition and structure refinement can produce higher quality, more accurate structures. The experimental and calculated parameters for the structures used for the fits in Figures 36 and 39 can be seen in Table 7. There was one particularly interesting case where both reported structures were published in the same year. This occurred for β -MgSO₄ where both structures were reported in 2007.^{60, 61} One structure reported was obtained through single-crystal X-ray diffraction, whereas the other was obtained through a neutron powder diffraction study. The structure determined through single crystal X-ray diffraction provided more accurate calculated NMR parameters than the neutron diffraction study. This is not entirely surprising since typically single crystal experiments produce more accurate determination of coordinates, although neutron diffraction provides better resolved data for protons. Another interesting case in this study was the results obtained for BaSO₄. In this case there were 5 previously reported crystal structures that produced quite a variety of calculated NMR parameters. Most of the structures produced calculated ³³S NMR parameters that were in noticeable disagreement with the experimental values. However, the 1977⁵⁰ and 1998⁴⁷ SC X-ray structures produced the best agreement with the experimental ³³S NMR. Upon closer examination of the reported crystal data^{47, 50} (as well as the .cif data in Appendix B used for calculation) it can be seen that the 1998 structure reported had a higher degree of resolution and statistical agreement factors in the structure refinement overall. Thus, the ³³S calculated NMR parameters obtained from the 1998 structure were selected to represent BaSO₄ in the NMR parameter fits. The other compounds studied were fairly straightforward in selecting the structure that produced the best agreement with the

experiment (Figures 35 and 39) as, in general, the older reported structures produced easily detectable disagreement with the experiment. It should also be noted that the calculations produced from the crystal structure selected for the ^{33}S fits also produced good agreement of calculated parameters for the other NMR active nuclei in the compounds. Specifically, the calculations for ^{23}Na in Na_2SO_4 , ^{39}K in K_2SO_4 , ^{87}Rb in Rb_2SO_4 , ^{133}Cs in Cs_2SO_4 , ^{25}Mg in $\alpha\text{-MgSO}_4$ and $\beta\text{-MgSO}_4$, ^{87}Sr in SrSO_4 , and $^{69}\text{Ga}/^{71}\text{Ga}$ in $\text{Ga}_2(\text{SO}_4)_3$ match well with previously reported NMR parameters for these nuclei.^{28, 185-190}

As mentioned previously, the first-principles CASTEP calculations produce absolute orientations of the shielding and electric field gradient tensors at a given nucleus in a compound. So, these tensors can be examined for ^{33}S and, although are only estimates, can give additional insight into the structure (i.e. site symmetry) affecting the tensors' orientation. Some examples of calculated tensor orientations for the studied compounds can be found in Figures 24-34, 37 and 38.

All sulfur sites are in a non-perfect tetrahedral environment of oxygen atoms, and the symmetry operations present at the sulfur site vary (Table 6). This leads to interesting effects with respect to calculated tensor orientations. When looking at these calculated tensors in more detail, it is easier to examine the sulfates on the basis of symmetry at the sulfur site. Sulfur in Na_2SO_4 , for example, has point group D_2 while the sulfates $\alpha\text{-MgSO}_4$ and CaSO_4 have sulfur with C_{2v} point group symmetry. Figures 26, 31 and 37 show the calculated EFG and CSA tensor orientations along with the relevant symmetry

operations at the sulfur site. For Na_2SO_4 it can be seen that the calculated tensor elements lie along the proper C2 rotation axes with V_{11}/σ_{11} and V_{33}/σ_{22} being coincident. With this symmetry one would expect coincident or perpendicular CSA and EFG tensors. As such, the experimental Euler angles for Na_2SO_4 are $\{90, 90, 0\}$. As well, even though the highest degree of symmetry is a 2-fold rotation, D_2 symmetry only requires two independent components of the symmetric part of shielding tensor, which implies axial symmetry.¹⁷² This is exactly what is observed for both the CSA and EFG tensor. α - MgSO_4 and CaSO_4 are quite similar in terms of calculated tensor orientations. As can be seen in Figures 31 and 37 the components of the tensors are restricted by the symmetry elements at the sulfur site, such that the principal component of the EFG tensor, V_{33} , is perpendicular to the two-fold axis, yet in one of the mirror planes. As well, the largest component of the shielding tensor, σ_{33} , lies perpendicular to the C2 axis and within a mirror plane. The calculated angle between V_{33} and σ_{33} (β) is 90° for α - MgSO_4 and 0° for CaSO_4 , which is reflected in the determined NMR parameters shown in Figures 31 and 37 and Table 7.

Another group of compounds studied that have the same point group symmetry at the sulfur site are K_2SO_4 , Rb_2SO_4 , Cs_2SO_4 , $(\text{NH}_4)_2\text{SO}_4$, β - MgSO_4 , SrSO_4 , BaSO_4 , and ZnSO_4 with point group C_s at the sulfur site. Since all these sites formally only have a reflection plane at the sulfur site, it is expected that several principal tensor components should lie within the plane. And, as one might expect, the calculated tensors for all these compounds show (Figures 24-27, 32, 34 and 38) the principal component of the EFG tensor, V_{33} , and the largest component of the shielding tensor, σ_{33} , lying in the reflection

plane. Examining Table 7 one can see that the calculated and experimental relative orientations between the EFG and CSA tensor vary among all of these compounds. This is not unexpected given the relatively low symmetry at the sulfur centre. One aspect, though, that these compounds do have in common is that the calculated V_{33} value always points along a pseudo- C_3 rotation axis or along a S-O bond (Figures 24-27, 32, 34 and 38). If this were a real C_3 rotation axis, however, one would expect the CSA and EFG tensor to be axially symmetric experimentally. By looking at Table 7, it can be seen that none of these compound have an axially symmetric EFG. $(\text{NH}_4)_2\text{SO}_4$ and $\beta\text{-MgSO}_4$ have an axially symmetric shielding tensor, however, the electric field gradient tensor for these compounds is not axially symmetric, which would mean that the axially symmetric nature of the CSA tensor is not due to a pseudo- C_3 rotation axis.

The last group of compounds studied has no formal symmetry operations at the sulfur site, which results in a C_1 point group at the sulfur centre. These are Li_2SO_4 , $\text{Al}_2(\text{SO}_4)_3$, $\text{Ga}_2(\text{SO}_4)_3$, and $\text{In}_2(\text{SO}_4)_3$. These compounds are, in fact, the only ones studied that do not form an orthorhombic unit cell and ultimately do not have any formal symmetry at the sulfur sites (Figures 28-30 and 33). Li_2SO_4 is seemingly the oddity in the group as it forms a monoclinic cell unlike the other orthorhombic alkali metal sulfates. The calculated absolute tensor orientations for Li_2SO_4 are not oriented towards any particular direction, however, the calculated V_{33} and σ_{33} would seem to be almost coincident ($\beta \approx 0^\circ$). Though, looking at the experimental results one can see that this is not the case and β is closer to $\sim 50^\circ$. This shows the potential accuracy for calculated parameters when there are no symmetry restrictions in the system thus restricting relative

assignments. The case is very similar for the Group 13 anhydrous sulfates. Given that there is no formal symmetry at the sulfur centre, the calculated and experimental tensor orientations do not logically tend toward any particular absolute or relative configuration. This is reflected in the calculated and experimentally determined parameters in Table 7 where the Euler angles are seemingly sporadic. However, despite the fact that the orientation of the calculated tensors is somewhat difficult to relate to the molecular structure, the magnitudes of the various tensor components and thus the observable NMR parameters were predicted quite well.

5. Conclusions and Future Work

With the availability of ultra-high fields the acquisition of reliable spectra in a reasonable amount of time for low- γ nuclei, such as ^{25}Mg and ^{33}S , has become possible and relatively straightforward. As such, the range of accessible quadrupolar coupling constants has been increased dramatically. Additionally, with further improvements on theoretical computational methods, the first principles plane-wave pseudopotential approach for calculating spectroscopic properties offers much promise for rapid and accurate calculations. In particular, the GIPAW method implemented within the CASTEP package has proven successful for use on nuclei such as ^{25}Mg and ^{33}S .

In particular, the ^{25}Mg SS-NMR performed in this work has increased the range of chemical shifts expected for ^{25}Mg in Mg-containing compounds to over 200 ppm. It was found that tetrahedrally coordinated Mg sites are the most deshielded and it is possible to

resolve multiple crystallographically unique sites when present in the structure. Chemical shift anisotropy has also been demonstrated in a number of cases. Although at higher magnetic fields this anisotropy can further complicate spectra, it was still found that the quadrupolar interaction was the dominating interaction for the majority of these Mg-containing compounds. ^{25}Mg has shown a strong sensitivity to local environment and so can be a very useful tool for structural studies. Quadrupolar and shielding interaction data from quantum mechanical calculations for ^{25}Mg have proven to be good value in interpretation of experimental results. This work has demonstrated the very broad range of Mg-containing materials now accessible to solid-state ^{25}Mg NMR at ultra-high magnetic fields. It can be expected that the knowledge gained herein can possibly be extended into organic, metal-organic and geochemical studies.

^{33}S SS-NMR studies performed in this work have shown that the determination of all pertinent NMR interaction parameters is possible at ultra-high fields. The NMR parameters determined for the anhydrous sulfates studied have shown that the quadrupolar interaction and the chemical shielding anisotropy are in relatively equal strengths, unlike the results for ^{25}Mg NMR parameters. Again, results from first principles calculations have proven to be quite useful in interpretation of the experimental results. In conjunction with multiple experimentally determined parameters, the calculations aided in performing structural assessments on sulfates where multiple reported crystal structures are present in the literature. Further analysis of the calculated quadrupolar and shielding interaction parameters has proven use in examining fine structural details and sulfur site-symmetry in these materials. From here it can be

anticipated that this type of analysis can be extended to a variety of sulfur-containing materials including organics and organo-metallics.

Given the inherent temperature sensitivity of the various NMR interactions, it can be expected that studies on temperature effects would greatly improve upon the knowledge gained in this work. Since calculations were essentially performed at 0 K, examining the effects that temperature may have on the calculations done herein would provide a better understanding of how the NMR interactions might behave under a more realistic setting. As well, obtaining experimental NMR spectra at lower temperatures might improve the signal to noise and thus reduce the experimental error of the determined NMR parameters. These are some possible future directions for the continuing investigation of the structural and NMR interaction relationships of these interesting nuclei.

6. References

1. NMR Crystallography. 1st ed.; Harris, R. K.; Wasylshen, R. E.; Duer, M., Eds. John Wiley & Sons Ltd.: West Sussex, UK, 2009.
2. In *CRC Handbook of Chemistry and Physics*, 87 ed.; Lide, E. D., Ed. CRC Press: Boca Raton, Florida, 2006.
3. Anders, E.; Ebihara, M., *Geochim. Cosmochim. Acta* **1982**, *46* (11), 2363-2380.
4. Hmiel, S. P.; Snavely, M. D.; Florer, J. B.; Maguire, M. E.; Miller, C. G., *J. Bacteriol.* **1989**, *171* (9), 4742-4751.
5. Maguire, M. E.; Cowan, J. A., *BioMetals* **2002**, *15* (3), 203-210.
6. Shaul, O., *BioMetals* **2002**, *15* (3), 307-321.
7. Pyykkö, P., *Molecular Physics: An International Journal at the Interface Between Chemistry and Physics* **2008**, *106* (16), 1965 - 1974.
8. Derighetti, B.; Hafner, S.; Marxer, H.; Rager, H., *Phys. Lett. A* **1978**, *66* (2), 150-152.
9. MacKenzie, K. J. D.; Meinhold, R. H., *Am. Mineral.* **1997**, *82*, 479-482.
10. MacKenzie, K. J. D.; Meinhold, R. H., *Am. Mineral.* **1994**, *79*, 43-50.
11. Fiske, P. S.; Stebbins, J. F., *Am. Mineral.* **1994**, *79*, 848-861.
12. MacKenzie, K. J. D.; Meinhold, R. H., *Am. Mineral.* **1994**, *79*, 250-260.
13. Bastow, T. J.; Celotto, S., *Solid State Nucl. Magn. Reson.* **2009**, *35* (4), 217-222.
14. Bastow, T. J.; Smith, M. E., *J. Phys.: Condens. Mat.* **1995**, *7* (25), 4929.
15. MacKenzie, K. J. D.; Meinhold, R. H., *J. Mater. Chem.* **1994**, *4*, 1595-1602.
16. O'Dell, L. A.; Savin, S. L. P.; Chadwick, A. V.; Smith, M. E., *Faraday Disc.* **2007**, *134*, 83-102.

17. Kim, Y.-I.; Cadars, S.; Shayib, R.; Proffen, T.; Feigerle, C. S.; Chmelka, B. F.; Seshadri, R., *Phys. Rev. B* **2008**, 78 (19), 195205.
18. Dupree, R.; Smith, M. E., *J. Chem. Soc. Chem. Comm.* **1988**, 1483-1485.
19. Bastow, T. J., *J. Phys.: Condens. Mat.* **1991**, 3 (6), 753.
20. Bastow, T. J.; Celotto, S., *Solid State Comm.* **1999**, 110 (5), 271-273.
21. Freitas, J. C. C.; Wong, A.; Smith, M. E., *Magn. Reson. Chem.* **2009**, 47 (1), 9-15.
22. Grant, C. V.; Frydman, V.; Frydman, L., *J. Am. Chem. Soc.* **2000**, 122 (47), 11743-11744.
23. Hung, I.; Schurko, R. W., *Solid State Nucl. Magn. Reson.* **2003**, 24 (2-3), 78-93.
24. Sham, S.; Wu, G., *Inorg. Chem.* **2000**, 39 (1), 4-5.
25. Widdifield, C. M.; Bryce, D. L., *Phys. Chem. Chem. Phys.* **2009**, 11, 7120-7122.
26. Wong, A.; Ida, R.; Mo, X.; Gan, Z.; Poh, J.; Wu, G., *J. Phys. Chem. A* **2006**, 110 (33), 10084-10090.
27. Wu, G.; Wong, A.; Wang, S., *Can. J. Chem.* **2003**, 81 (4), 275-283.
28. Pallister, P. J.; Moudrakovski, I. L.; Ripmeester, J. A., *Phys. Chem. Chem. Phys.* **2009**, 11 (48), 11487-11500.
29. Schmidt, M.; Siebert, W., The Chemistry of Sulfur. In *Comprehensive Inorganic Chemistry*, Pergamon Press: Oxford, England, 1975; Vol. 2.
30. Industrial Applications of Batteries: From Cars to Aerospace and Energy Storage. Broussely, M.; Pistoia, G., Eds. Elsevier Science: 2007.
31. Concrete Technology: New Trends, Industrial Applications Proceedings of the International Workshop. Aguado, A.; Gettu, R.; Shah, S. P., Eds. E & FN Spon: London, England, 1995; Vol. 26.

32. Natural Products in the New Millennium: Prospects and Industrial Application. In *Proceedings of the Phytochemical Society of Europe*, Rauter, A. P.; Palma, F. B.; Justino, J.; Araujo, M. E.; Pina dos Santos, S., Eds. Springer: 2003.
33. Eckert, H.; Yesinowski, J. P., *J. Am. Chem. Soc.* **1986**, *108*, 2140.
34. Daunch, W. A.; Rinaldi, P. L., *J. Magn. Reson. A* **1996**, *123*, 219.
35. Wagler, T. A.; Daunch, W. A.; Rinaldi, P. L.; Palmer, A. R., *J. Magn. Reson.* **2003**, *161*, 191.
36. Couch, S.; Howes, A. P.; Kohn, S. C.; Smith, M. E., *Solid State Nucl. Magn. Reson.* **2004**, *26*, 203.
37. d'Espinose de Lacaillerie, J.-B.; Barberon, F.; Bresson, B.; Fonollosa, P.; Zanni, H.; Fedorov, V. E.; Naumov, N. G.; Gan, Z., *Cement and Concrete Res.* **2006**, *36* (9), 1781-1783.
38. Hansen, M. R.; Brorson, M.; Bildsøe, H.; Skibsted, J.; Jakobsen, H., *J. Magn. Reson.* **2008**, *190*, 316.
39. Jakobsen, H.; Hove, A. R.; Bildsøe, H.; Skibsted, J., *J. Magn. Reson.* **2006**, *180*, 170.
40. Wagler, T. A.; Daunch, W. A.; Panzner, M.; Youngs, W. J.; Rinaldi, P. L., *J. Magn. Reson.* **2004**, *170* (2), 336-344.
41. Sutrisno, A.; Terskikh, V. V.; Huang, Y., *Chem. Comm.* **2009**, 186.
42. Moudrakovski, I.; Lang, S.; Patchkovskii, S.; Ripmeester, J., *J. Phys. Chem. A* **2010**, *114* (1), 309-316.
43. Wyckoff, R. W. G., *Crystal Structures*. 2 ed.; John Wiley & Sons: New York, 1964.

44. Nord, A. G., *Acta Cryst. B* **1976**, *32* (3), 982-983.
45. Hawthorne, F. C.; Ferguson, R. B., *Can. Mineral.* **1975**, *13* (3), 289-292.
46. Hawthorne, F. C.; Ferguson, R. B., *Can. Mineral.* **1975**, *13* (2), 181-187.
47. Jacobsen, S. D.; Smyth, J. R.; Swope, J.; Downs, R. T., *Can. Mineral.* **1998**, *36* (4), 1053-1060.
48. Ojima, K.; Nishihata, Y.; Sawada, A., *Acta Cryst. B* **1995**, *51*, 287-293.
49. Colville, A. A.; Staudhammer, K., *Am. Mineral.* **1967**, *52*, 1877-1880.
50. Hill, R. J., *Can. Mineral.* **1977**, *15* (4), 522-526.
51. Miyake, M.; Minato, I.; Morikawa, H.; Iwai, S., *Am. Mineral.* **1978**, *63*, 506-510.
52. Nord, A. G., *Acta Cryst. B* **1974**, *30*, 1640-1641.
53. Enright, G., Room Temperature Rubidium Sulfate. National Research Council: Ottawa, 2010. Unpublished results.
54. Wildner, M.; Giester, G., *Mineral. and Petrol.* **1988**, *39* (3), 201-209.
55. Enright, G., Room Temperature Cesium Sulfate. National Research Council: Ottawa, 2010. Unpublished results.
56. Dahmen, T.; Gruehn, R., *Z. für Krist.* **1993**, *204*, 57-65.
57. Schlemper, E. O.; Hamilton, W. C., *J. Chem. Phys.* **1966**, *44* (12), 4498-4509.
58. Enright, G., Room Temperature Ammonium Sulfate. National Research Council: Ottawa, 2010. Unpublished results.
59. Krause, M.; Gruehn, R., *Z. für Krist.* **1995**, *210* (6), 427-431.
60. Fortes, A. D.; Wood, I. G.; Vocadlo, L.; Brand, H. E. A.; Knight, K. S., *J. Appl. Cryst.* **2007**, *40*, 761-770.
61. Weil, M., *Acta Cryst. E* **2007**, *63*, i172.

62. Levitt, M. H., *Spin Dynamics: Basics of Nuclear Magnetic Resonance*. John Wiley & Sons Ltd.: West Sussex, 2008.
63. Bloch, F.; Hansen, W. W.; Packard, M., *Phys. Rev.* **1946**, *69* (3-4), 127.
64. Purcell, E. M.; Torrey, H. C.; Pound, R. V., *Phys. Rev.* **1946**, *69* (1-2), 37.
65. Ramsey, N. F., *Phys. Rev.* **1950**, *78* (6), 699.
66. Ramsey, N. F., *Phys. Rev.* **1950**, *77* (4), 567.
67. Ramsey, N. F., *Phys. Rev.* **1951**, *83* (3), 540.
68. Ramsey, N. F., *Phys. Rev.* **1952**, *86* (2), 243.
69. Pople, J. A., *Proc. Royal Soc. London. Series A. Math. and Phys. Sci.* **1957**, *239* (1219), 541-549.
70. Pople, J. A., *Disc. Faraday Soc.* **1962**, *34*, 7-14.
71. Anet, F. A. L.; O'Leary, D. J., *Concepts in Magn. Reson.* **1991**, *3* (4), 193-214.
72. Hansen, A. E.; Bouman, T. D., *J. Chem. Phys.* **1989**, *91* (6), 3552-3560.
73. Wi, S.; Frydman, L., *J. Chem. Phys.* **2002**, *116* (4), 1551-1561.
74. Mason, J., *Solid State Nucl. Magn. Reson.* **1993**, *2* (5), 285-288.
75. Haeberlen, U., *Advances in Magnetic Resonance*. Suppl. 1 ed.; Academic Press: New York, 1976.
76. Mehring, M., *Principles of High Resolution NMR in Solids*. 2nd ed.; Springer-Verlag: Berlin, 1983.
77. Stebbins, J. F.; Smyth, J. R.; Panero, W. R.; Frost, D. J., *Am. Mineral.* **2009**, *94* (7), 905-915.
78. Andrew, E. R.; Bradbury, A.; Eades, R. G., *Nature* **1958**, *182* (4650), 1659-1659.
79. Lowe, I. J., *Phys. Rev. Lett.* **1959**, *2* (7), 285.

80. Jameson, C. J.; Jameson, A. K.; Burrell, P. M., *J. Chem. Phys.* **1980**, *73* (12), 6013-6020.
81. Ashbrook, S. E.; Duer, M. J., *Concepts in Magn. Reson. A* **2006**, *28A* (3), 183-248.
82. Abragam, A., The Principles of Nuclear Magnetism. In *The International Series of Monographs on Physics*, Birman, J.; Edwards, S. F.; Friend, R. H.; Smith, C. H.; Rees, M.; Sherrington, D.; Veneziano, G., Eds. Oxford University Press: Oxford, 1961; Vol. 32.
83. Duer, M., *Introduction to Solid-State NMR Spectroscopy*. 1st ed.; Blackwell Publishing Ltd.: Oxford, 2004.
84. Smith, M. E.; van Eck, E. R. H., *Prog. Nucl. Magn. Reson. Spec.* **1999**, *34* (2), 159-201.
85. Engelhardt, G.; Koller, H., *Magn. Reson. Chem.* **1991**, *29* (9), 941-945.
86. Kentgens, A. P. M., *Geoderma* **1997**, *80* (3-4), 271-306.
87. Freude, D.; Haase, J., Quadrupole effects in solid-state nuclear magnetic resonance. In *NMR Basic Principles and Progress*, Diehl, P.; Fluck, E.; Günther, H.; Kasfeld, R.; Seelig, J., Eds. Springer-Verlag: Berlin, 1993; Vol. 29, p 1.
88. Gutowsky, H. S.; Pake, G. E., *J. Chem. Phys.* **1950**, *18* (2), 162-170.
89. Pake, G. E., *J. Chem. Phys.* **1948**, *16* (4), 327-336.
90. Laws, D. D.; Bitter, H.-M. L.; Jerschow, A., *Angew. Chem. Int. Ed.* **2002**, *41* (17), 3096-3129.
91. Carr, H. Y.; Purcell, E. M., *Phys. Rev.* **1954**, *94* (3), 630.
92. Meiboom, S.; Gill, D., *Rev. Sci. Inst.* **1958**, *29* (8), 688-691.

93. Bloom, M.; Stermin, E., *Biochem.* **1987**, *26* (8), 2101-2105.
94. Cheng, J. T.; Ellis, P. D., *J. Phys. Chem.* **1989**, *93*, 2549-2555.
95. Hahn, E. L., *Phys. Rev.* **1950**, *80* (4), 580.
96. Davis, J. H.; Jeffrey, K. R.; Bloom, M.; Valic, M. I.; Higgs, T. P., *Chem. Phys. Lett.* **1976**, *42* (2), 390-394.
97. Solomon, I., *Phys. Rev.* **1958**, *110* (1), 61.
98. Weisman, I. D.; Bennett, L. H., *Phys. Rev.* **1969**, *181* (3), 1341.
99. Larsen, F. H.; Jakobsen, H. J.; Ellis, P. D.; Nielsen, N. C., *J. Magn. Reson.* **1998**, *131* (1), 144-147.
100. Yao, Z.; Kwak, H.-T.; Sakellariou, D.; Emsley, L.; Grandinetti, P. J., *Chem. Phys. Lett.* **2000**, *327* (1-2), 85-90.
101. Kentgens, A. P. M.; Verhagen, R., *Chem. Phys. Lett.* **1999**, *300* (3-4), 435-443.
102. Siegel, R.; Nakashima, T. T.; Wasylshen, R. E., *Chem. Phys. Lett.* **2004**, *388* (4-6), 441-445.
103. Kupče, E.; Freeman, R., *J. Magn. Reson. A* **1995**, *115* (2), 273-276.
104. O'Dell, L. A.; Schurko, R. W., *Chem. Phys. Lett.* **2008**, *464* (1-3), 97-102.
105. Bloch, F., *Phys. Rev.* **1956**, *102* (1), 104.
106. Bloch, F., *Phys. Rev.* **1958**, *111* (3), 841.
107. Levitt, M. H., *Prog. Nucl. Magn. Reson. Spec.* **1986**, *18* (2), 61-122.
108. Shaka, A. J.; Keeler, J., *Prog. Nucl. Magn. Reson. Spec.* **1987**, *19* (1), 47-129.
109. Cheeseman, J. R.; Trucks, G. W.; Keith, T. A.; Frisch, M. J., *J. Chem. Phys.* **1996**, *104* (14), 5497-5509.
110. Ditchfield, R., *J. Chem. Phys.* **1972**, *56* (11), 5688-5691.

111. Keith, T. A.; Bader, R. F. W., *Chem. Phys. Lett.* **1992**, *194* (1-2), 1-8.
112. Tossell, J. A., *Phys. Chem. Mineral.* **1999**, *27* (1), 70-80.
113. Valerio, G.; Goursot, A., *J. Phys. Chem. B* **1999**, *103* (1), 51-58.
114. Valerio, G.; Goursot, A.; Vetrivel, R.; Malkina, O.; Malkin, V.; Salahub, D. R., *J. Am. Chem. Soc.* **1998**, *120* (44), 11426-11431.
115. Van de Walle, C. G.; Blöchl, P. E., *Phys. Rev. B* **1993**, *47* (8), 4244.
116. Mauri, F.; Louie, S. G., *Phys. Rev. Lett.* **1996**, *76* (22), 4246.
117. Mauri, F.; Pfrommer, B. G.; Louie, S. G., *Phys. Rev. Lett.* **1996**, *77* (26), 5300.
118. Pickard, C. J.; Mauri, F., *Phys. Rev. B* **2001**, *63* (24), 245101.
119. Segall, M. D.; et al., *J. Phys.: Condens. Mat.* **2002**, *14* (11), 2717.
120. Yates, J. R.; Pickard, C. J.; Mauri, F., *Phys. Rev. B* **2007**, *76* (2), 024401.
121. Clark, S. J.; Segall, M. D.; Pickard, C. J.; Hasnip, P. J.; Probert, M. I. J.; Refson, K.; Payne, M. C., *Z. für Krist.* **2005**, *220* (5-6-2005), 567-570.
122. Hamann, D. R.; Schlüter, M.; Chiang, C., *Phys. Rev. Lett.* **1979**, *43* (20), 1494.
123. Vanderbilt, D., *Phys. Rev. B* **1990**, *41* (11), 7892.
124. Profeta, M.; Mauri, F.; Pickard, C. J., *J. Am. Chem. Soc.* **2003**, *125* (2), 541-548.
125. Benoit, M.; Profeta, M.; Mauri, F.; Pickard, C. J.; Tuckerman, M. E., *J. Phys. Chem. B* **2005**, *109* (13), 6052-6060.
126. Harris, R. K.; Joyce, S. A.; Pickard, C. J.; Cadars, S.; Emsley, L., *Phys. Chem. Chem. Phys.* **2006**, *8* (1), 137-143.
127. Ashbrook, S. E.; Berry, A. J.; Frost, D. J.; Gregorovic, A.; Pickard, C. J.; Readman, J. E.; Wimperis, S., *J. Am. Chem. Soc.* **2007**, *129* (43), 13213-13224.

128. Gervais, C.; Bonhomme-Courty, L.; Mauri, F.; Babonneau, F.; Bonhomme, C., *Phys. Chem. Chem. Phys.* **2009**, *11* (32), 6953-6961.
129. Griffin, J. M.; Wimperis, S.; Berry, A. J.; Pickard, C. J.; Ashbrook, S. E., *J. Phys. Chem. C* **2009**, *113* (1), 465-471.
130. Salager, E.; Stein, R. S.; Pickard, C. J.; Elena, B.; Emsley, L., *Phys. Chem. Chem. Phys.* **2009**, *11* (15), 2610-2621.
131. Siew Hew Sam, D.; Soenen, V.; Volta, J. C., *J. Catal.* **1990**, *123* (2), 417-435.
132. Deichman, E. N., *Rus. J. Inorg. Chem.* **1961**, *6* (7), 855-859.
133. Larsen, F. H.; Jakobsen, H. J.; Ellis, P. D.; Nielsen, N. C., *J. Phys. Chem. A* **1997**, *101*, 8597.
134. Massiot, D.; Fayon, F.; Capron, M.; King, I.; Calvé, S. L.; Alonso, B.; Durand, J.-O.; Bujoli, B.; Gan, Z.; Hoatson, G., *Magn. Reson. Chem.* **2002**, *40* (1), 70-76.
135. Eichele, K.; Wasylishen, R. E. *WSOLIDS NMR Simulation Package*, 1.19.11; 2009.
136. Rohonczy, J. *Bruker BioSpin Solid Lineshape Analysis Tool*, 2.1; Rheinstetten, Germany, 2009.
137. Clark, S. J.; Segall, M. D.; Pickard, C. J.; Hasnip, P. J.; Probert, M. I. J.; Refson, K.; Payne, M. C., *Z. für Krist.* **2009**, *220* (5-6-2005), 567-570.
138. Perdew, J. P.; Burke, K.; Ernzerhof, M., *Phys. Rev. Lett.* **1996**, *77* (18), 3865.
139. Perdew, J. P.; Burke, K.; Ernzerhof, M., *Phys. Rev. Lett.* **1997**, *78* (7), 1396.
140. Pfrommer, B. G.; Côté, M.; Louie, S. G.; Cohen, M. L., *J. Comput. Phys.* **1997**, *131* (1), 233-240.
141. Adiga, S.; Aebi, D.; Bryce, D. L., *Can. J. Chem.* **2007**, *85*, 496-505.

142. Hazen, R. M., *Am. Mineral.* **1976**, *61*, 266-271.
143. Catti, M.; Ferraris, G.; Hull, S.; Pavese, A., *Phys. Chem. Mineral.* **1995**, *22* (3), 200-206.
144. Zalkin, A.; Ruben, H.; Templeton, D. H., *Acta Cryst.* **1964**, *17*, 235-240.
145. Baur, W. H., *Acta Cryst.* **1964**, *17*, 1361-1369.
146. Margulis, T.; Templeton, D. H., *Z. für Krist.* **1962**, *117*, 344-357.
147. Liu, B. N.; T., Z. X.; Cui, X. S.; Tang, J. G., *Sci. China B* **1990**, *33*, 1350-1356.
148. Agron, P. A.; Busing, W. R., *Acta Cryst. C* **1985**, *41*, 8-10.
149. Takagi, S.; Mathew, M.; Brown, W. E., *Am. Mineral.* **1986**, *71*, 1229-1233.
150. Bartl, H.; Catti, M.; Joswig, W.; Ferraris, G., *Tschermaks Mineralogische und Petrographische Mitteilungen* **1983**, *32*, 187-194.
151. Bakakin, V. V.; Klevtsova, R. F.; Gaponenko, L. A., *Kristallografiya* **1982**, *27*, 38-42.
152. Macavei, J.; Schulz, H., *Z. für Krist.* **1993**, *207*, 193-208.
153. Nielsen, U. G.; Jakobsen, H. J.; Skibsted, J.; Norby, P., *J. Chem. Soc. Dalton Trans.* **2001**, (21), 3214-3218.
154. Krishnamarchari, N.; Calvo, C., *Can. J. Chem.* **1971**, *49*, 1629-1637.
155. Wechsler, B. A.; Von Dreele, R. B., *Acta Cryst. B* **1989**, *45*, 542-549.
156. Markgraf, S. A.; Reeder, R. J., *Am. Mineral.* **1985**, *70*, 590-600.
157. Peterson, R. C.; Lager, G. A.; Hitterman, R. L., *Am. Mineral.* **1991**, *76*, 1455-1458.
158. Kusaka, K.; Hagiya, K.; Ohmasa, M.; Okano, Y.; Mukai, M.; Iishi, K.; Haga, N., *Phys. Chem. Mineral.* **2001**, *28* (3), 150-166.

159. Morosin, B., *Acta Cryst.* **1967**, 22, 316-320.
160. Irish, D. E.; Semmler, J.; Taylor, N. J.; Toogood, G. E., *Acta Cryst. C* **1991**, 47, 2322-2324.
161. Noritaki, T.; Aoki, M.; Towata, S.; Seno, Y.; Hirose, Y., *R&D Review from ToyotaCRDL* **2003**, 38 (2), 15.
162. Partin, D. E.; O'Keeffe, M., *J. Solid State Chem.* **1991**, 95 (1), 176-183.
163. Ratai, E.; Augustine, M. P.; Kauzlarich, S. M., *J. Phys. Chem. B* **2003**, 107 (46), 12573-12577.
164. Janczak, J.; Kubiak, R., *Polyhedron* **2001**, 20 (24-25), 2901-2909.
165. Harris, R. K.; Hodgkinson, P.; Pickard, C. J.; Yates, J. R.; Zorin, V., *Magn. Reson. Chem.* **2007**, 45 (S1), S174-S186.
166. Kolokolov, D. I.; Glaznev, I. S.; Aristov, Y. I.; Stepanov, A. G.; Jobic, H., *J. Phys. Chem. C* **2008**, 112 (33), 12853-12860.
167. Soda, G.; Chiba, T., *J. Chem. Phys.* **1969**, 50 (1), 439-455.
168. O'Dell, L. A.; Schurko, R. W., *Phys. Chem. Chem. Phys.* **2009**, 11 (32), 7069-7077.
169. Fiske, P. S.; Stebbins, J. F.; Farnan, I., *Phys. Chem. Mineral.* **1994**, 20 (8), 587-593.
170. Bastow, T. J., *Solid State Comm.* **1991**, 77 (7), 547-548.
171. Buckingham, A. D.; Malm, S. M., *Molecular Physics: An International Journal at the Interface Between Chemistry and Physics* **1971**, 22 (6), 1127 - 1130.
172. Robert, J. B.; Wiesenfeld, L., *Phys. Rep.* **1982**, 86 (7), 363-401.
173. Akitt, J. W.; McDonald, W. S., *J. Magn. Reson. (1969)* **1984**, 58 (3), 401-412.

174. Ferrari, A.; Braibanti, A.; Bigliardi, G., *Acta Cryst.* **1963**, *16* (8), 846-847.
175. Bryce, David L.; Bultz, Elijah B., *Chemistry - A European Journal* **2007**, *13* (17), 4786-4796.
176. Kroeker, S.; Stebbins, J. F., *Am. Mineral.* **2000**, *85*, 1459-1464.
177. Bastow, T. J., *Chem. Phys. Lett.* **2002**, *354* (1-2), 156-159.
178. Graf, D. L., *Am. Mineral.* **1961**, *46*, 1283-1316.
179. Ross, N. L., *Am. Mineral.* **1997**, *82*, 682-688.
180. Padro, D.; Howes, A. P.; Smith, M. E.; Dupree, R., *Solid State Nucl. Magn. Reson.* **2000**, *15* (4), 231-236.
181. Larsen, F. H.; Skibsted, J.; Jakobsen, H. J.; Nielsen, N. C., *J. Am. Chem. Soc.* **2000**, *122* (29), 7080-7086.
182. Musio, R., Applications of ^{33}S NMR Spectroscopy. In *Annual Reports on NMR Spectroscopy*, Graham, A. W., Ed. Academic Press: 2009; Vol. Volume 68, pp 1-88.
183. Shannon, R. D., *Acta Cryst. A* **1976**, *32*, 751-767.
184. Smirnov, L. S.; Natkaniec, I.; Bragin, S. I.; Shuvalov, L. A.; Sulyanov, S. N., *Phys. B: Condens. Mat.* **1997**, *234-236*, 66-67.
185. Ash, J. T.; Grandinetti, P. J., *Magn. Reson. Chem.* **2006**, *44* (9), 823-831.
186. Bowers, G. M.; Lipton, A. S.; Mueller, K. T., *Solid State Nucl. Magn. Reson.* **2006**, *29* (1-3), 95-103.
187. Koller, H.; Engelhardt, G.; Kentgens, A. P. M.; Sauer, J., *J. Phys. Chem.* **1994**, *98* (6), 1544-1551.
188. Moudrakovski, I. L.; Ripmeester, J. A., *J. Phys. Chem. B* **2007**, *111* (3), 491-495.

189. Skibsted, J.; Vosegaard, T.; Bildsøe, H.; Jakobsen, H. J., *J. Phys. Chem.* **1996**, *100* (36), 14872-14881.
190. Vosegaard, T.; Skibsted, J.; Bildsøe, H.; Jakobsen, H. J., *J. Magn. Reson. A* **1996**, *122* (2), 111-119.

7. Appendix

Appendix A - Additional ^{25}Mg SS-NMR Spectra

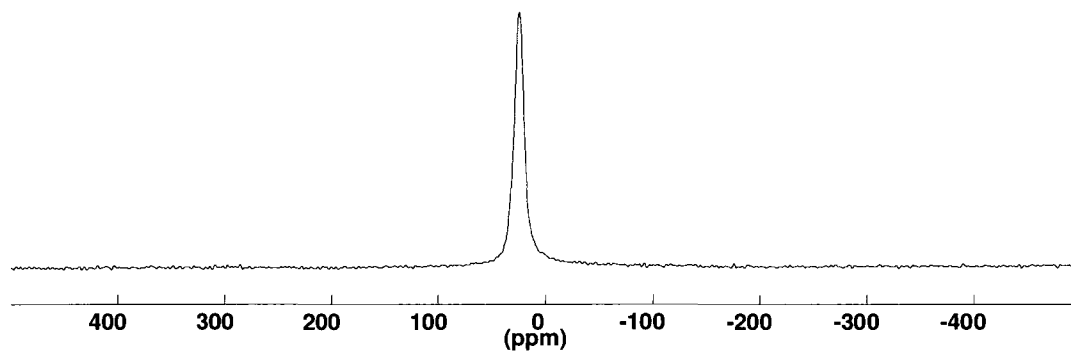


Figure A1 – Static Bloch Decay ^{25}Mg NMR spectrum of MgO.

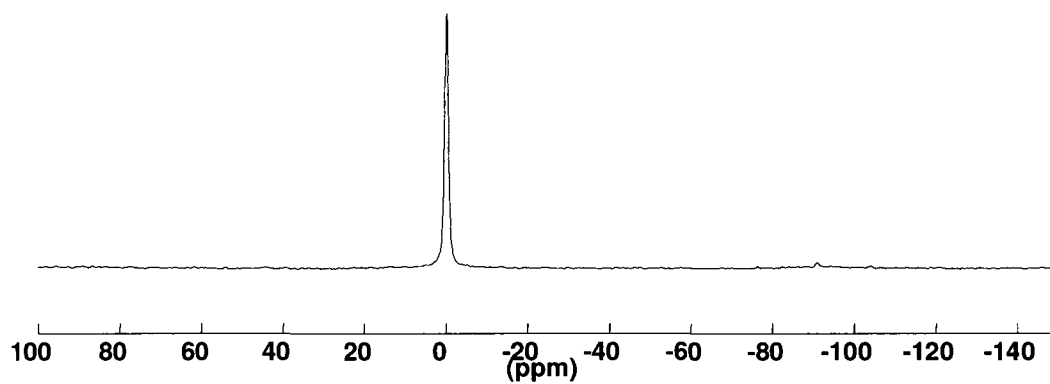


Figure A2 – 5 kHz MAS Bloch Decay ^{25}Mg NMR spectrum of $\text{MgCl}_2 \cdot 6\text{H}_2\text{O}$

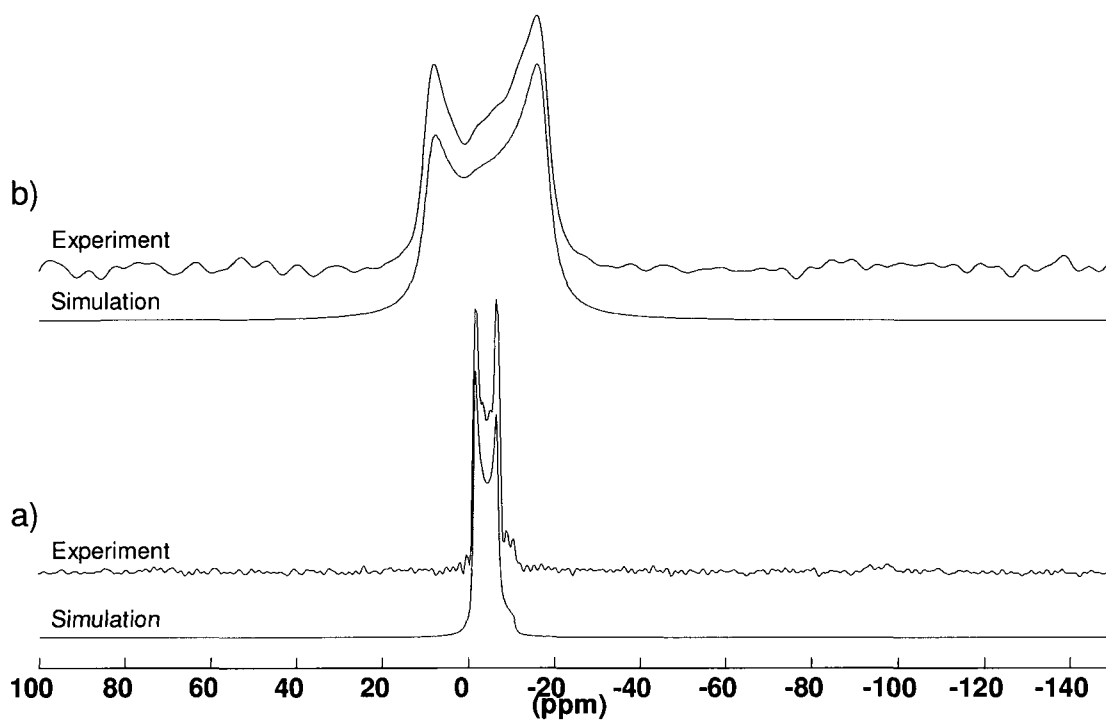


Figure A3 – a) 5 kHz MAS Bloch Decay ^{25}Mg NMR spectra (experimental and simulated) of $\text{Mg}(\text{NO}_3)_2 \cdot 6\text{H}_2\text{O}$. b) Static Hahn Echo ^{25}Mg NMR spectra (experimental and simulated) of $\text{Mg}(\text{NO}_3)_2 \cdot 6\text{H}_2\text{O}$.

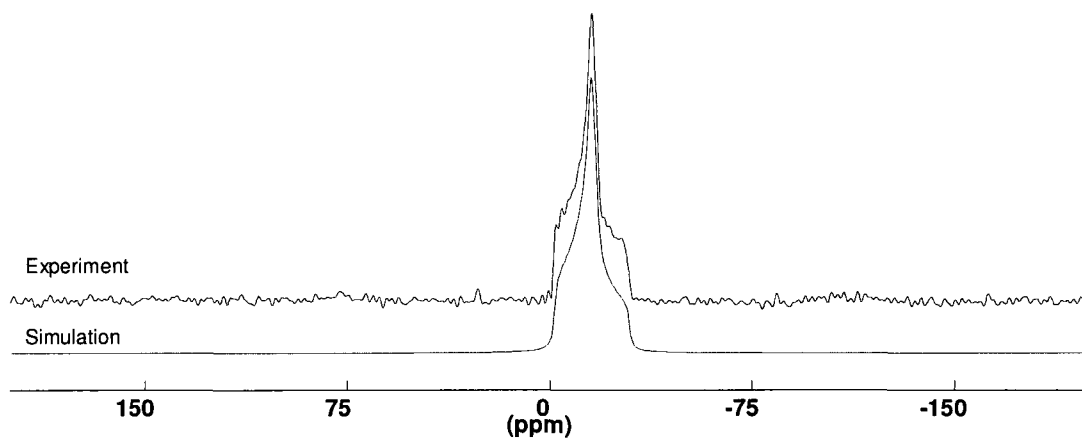


Figure A4 – 5 kHz MAS Bloch Decay ^{25}Mg NMR spectra (experimental and simulated) of MgWO_4 .

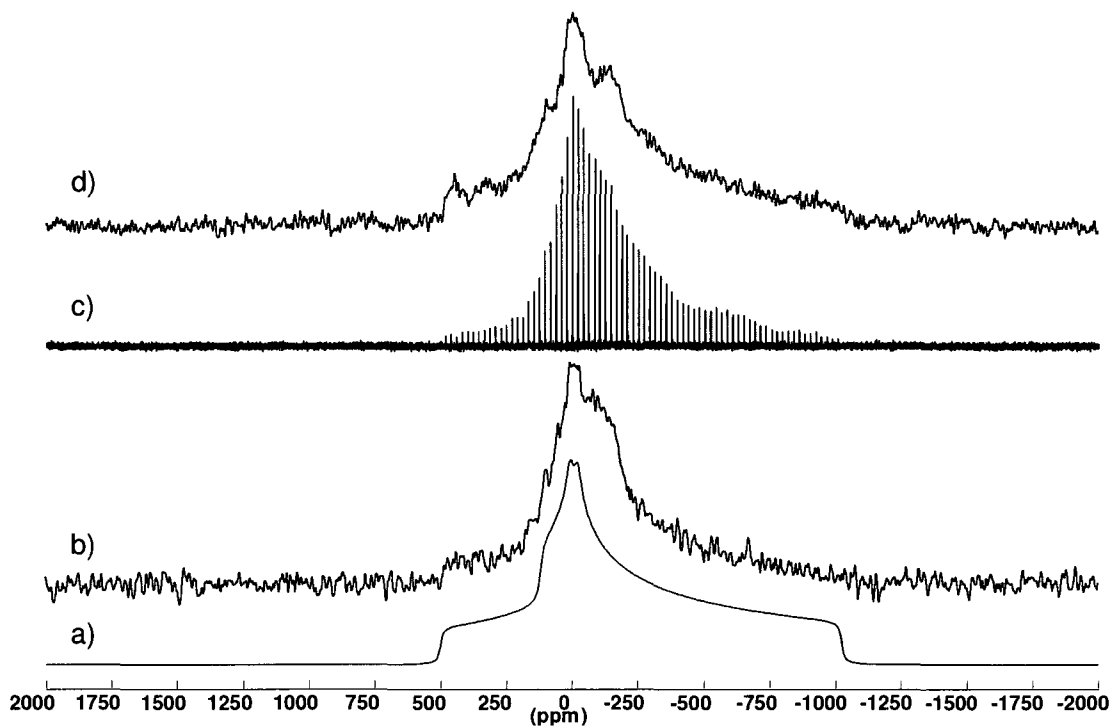


Figure A5 – ^{25}Mg SS-NMR spectra of $\text{Mg}(\text{VO}_3)_2$. a) Simulation of the single crystallographically unique site in $\text{Mg}(\text{VO}_3)_2$. b) Static full Hahn Echo. c) Static QCPMG. d) Static full Hahn Echo obtained in 3 pieces with stepped central excitation frequencies (O1) to observe edge singularities.

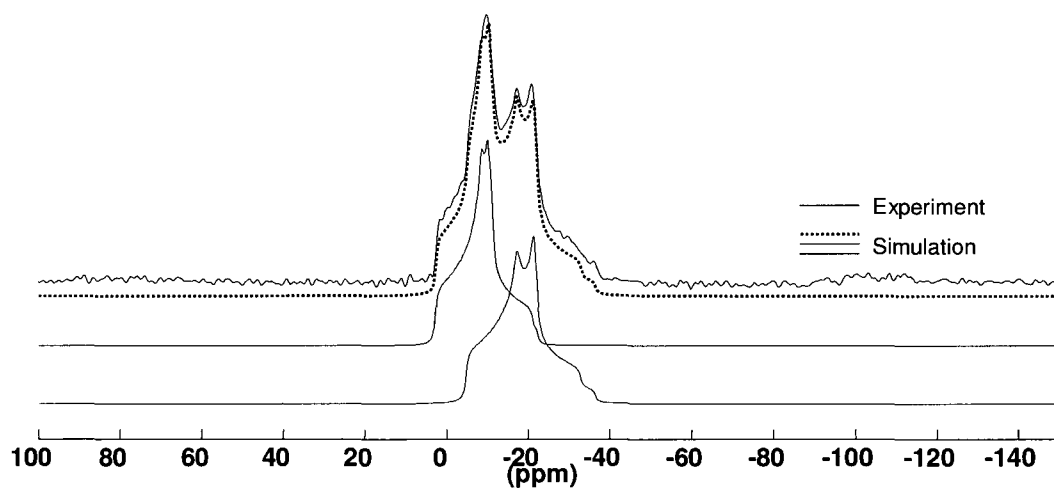


Figure A6 – 5 kHz MAS Bloch Decay ^{25}Mg NMR spectra (experimental and simulated) of $\alpha\text{-Mg}_2\text{V}_2\text{O}_7$.

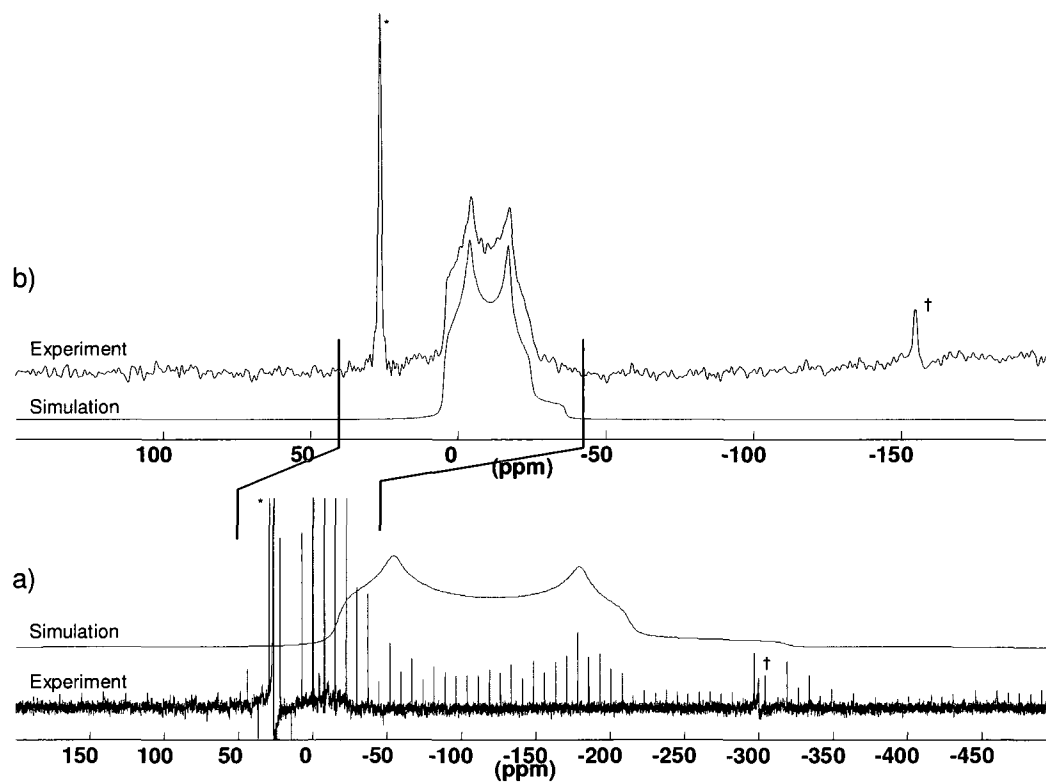


Figure A7 – $\text{Mg}_3(\text{VO}_4)_2$. a) 18 kHz MAS QCPMG ^{25}Mg spectra (experimental and simulated) of $\text{Mg}_3(\text{VO}_4)_2$ zoomed in on the low intensity site with the larger C_Q . b) 10 kHz MAS Bloch decay ^{25}Mg spectra (experimental and simulated) of $\text{Mg}_3(\text{VO}_4)_2$ showing the site with the smaller C_Q . The second site is too broad and weak to be seen at 10 kHz MAS Bloch Decay. *MgO; †MgO spinning sideband.

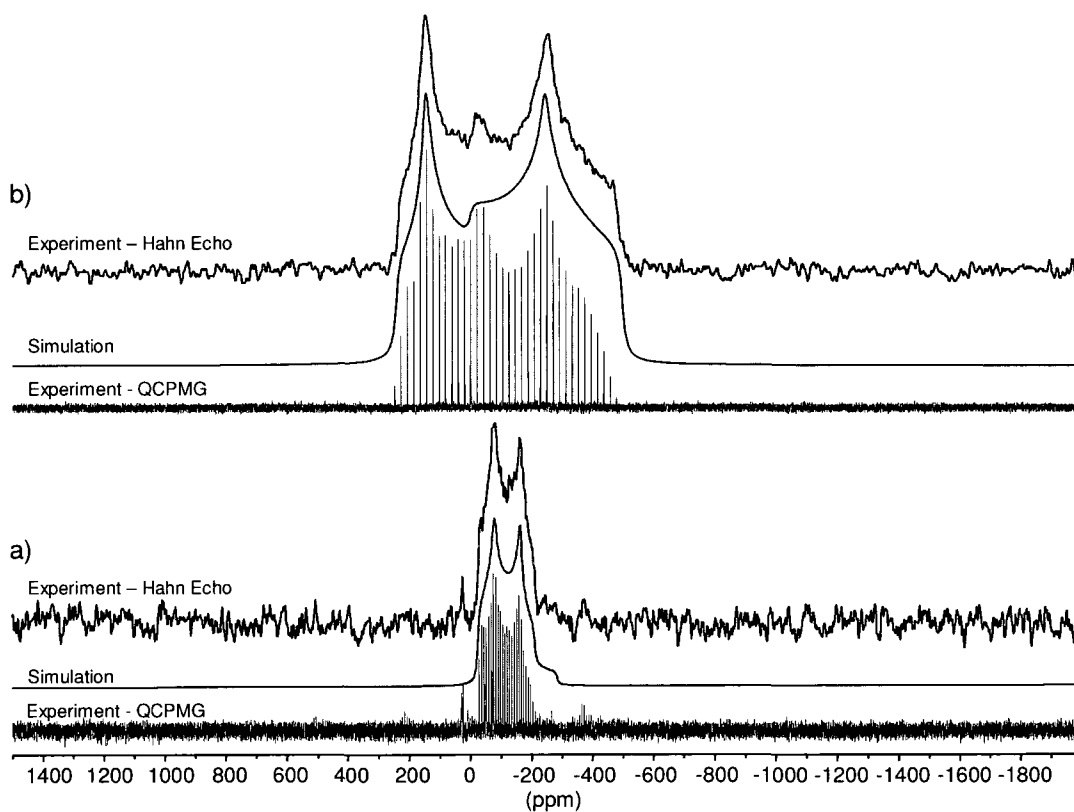


Figure A8 – $\alpha\text{-MgSO}_4$. a) 16 kHz MAS QCPMG, Hahn echo and simulated ^{25}Mg NMR spectra of $\alpha\text{-MgSO}_4$. b) Static QCPMG, Hahn echo and simulated ^{25}Mg NMR spectra of $\alpha\text{-MgSO}_4$.

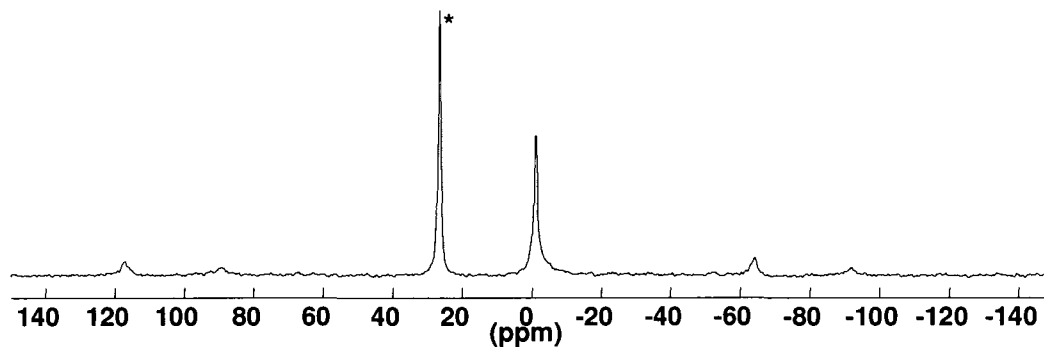


Figure A9 – 5 kHz MAS Bloch Decay ^{25}Mg NMR spectrum of MgS. *MgO.

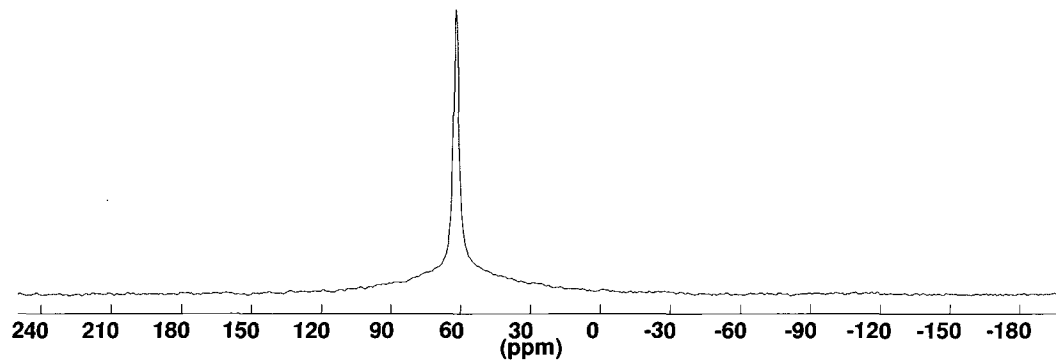


Figure A10 – Static Bloch Decay ^{25}Mg NMR spectrum of Mg_2Si .

Appendix B - Structural Details of All Compounds (.cif files)

Order of .cif files is occurs as in Tables 4 and 7.

MgO

```

data_MgO
_symmetry_space_group_name_H-M 'FM-3M'
_symmetry_Int_Tables_number 225
_symmetry_cell_setting cubic
_cell_length_a 4.2112
_cell_length_b 4.2112
_cell_length_c 4.2112
_cell_angle_alpha 90.0000
_cell_angle_beta 90.0000
_cell_angle_gamma 90.0000
loop_
_atom_site_label
_atom_site_type_symbol
_atom_site_fract_x
_atom_site_fract_y
_atom_site_fract_z
_atom_site_U_iso_or_equiv
_atom_site_adp_type
_atom_site_occupancy
Mg Mg 0.00000 0.00000 0.00000 0.00000 Uiso 1.00
O O 0.50000 0.50000 0.50000 0.00000 Uiso 1.00

```

Brucite, Mg(OH)₂

```

data_global
_chemical_name 'Brucite'
_chemical_formula_sum 'Mg O2 H2'
_cell_length_a 3.14979
_cell_length_b 3.14979
_cell_length_c 4.7702
_cell_angle_alpha 90
_cell_angle_beta 90
_cell_angle_gamma 120
_cell_volume 40.986
_symmetry_space_group_name_H-M 'P -3 m 1'
loop_
_atom_site_label
_atom_site_fract_x
_atom_site_fract_y
_atom_site_fract_z
_atom_site_U_iso_or_equiv
Mg 0.00000 0.00000 0.00000 0.00545

```

O 0.33333 0.66667 0.22030 0.00532
 H 0.33333 0.66667 0.41300 ?

MgSO₄·6H₂O

data_global
 _chemical_name 'Hexahydrate'
 _chemical_formula_sum 'Mg S O10 H12'
 _cell_length_a 10.110
 _cell_length_b 7.212
 _cell_length_c 24.41
 _cell_angle_alpha 90
 _cell_angle_beta 98.30
 _cell_angle_gamma 90
 _cell_volume 1761.172
 _symmetry_space_group_name_H-M 'C 1 2/c 1'
 loop_
 _atom_site_label
 _atom_site_fract_x
 _atom_site_fract_y
 _atom_site_fract_z
 _atom_site_Uiso_or_equiv
 Mg1 0.00000 0.00000 0.00000 ?
 Mg2 0.00000 0.94250 0.25000 ?
 S 0.86590 0.44900 0.12410 ?
 O1 0.77470 0.59860 0.13610 ?
 O2 0.98340 0.44420 0.16650 ?
 O3 0.90690 0.48540 0.06920 ?
 O4 0.79610 0.26880 0.12110 ?
 O5 0.58520 0.71250 0.04830 ?
 O6 0.53930 0.31620 0.06400 ?
 O7 0.31260 0.54640 0.02310 ?
 O8 0.88870 0.14860 0.28200 ?
 O9 0.88840 0.74050 0.28110 ?
 O10 0.85980 0.94350 0.17990 ?
 H1 0.64300 0.69800 0.07600 0.02406
 H2 0.53900 0.80600 0.04500 0.06586
 H3 0.49500 0.23200 0.06000 0.02406
 H4 0.61400 0.34000 0.09300 0.07219
 H5 0.30400 0.65000 0.05500 0.07092
 H6 0.27100 0.54400 0.01400 0.02406
 H7 0.84000 0.09200 0.31200 0.05446
 H8 0.93700 0.23500 0.29600 0.01646
 H9 0.94000 0.65100 0.29100 0.07472
 H10 0.82000 0.73300 0.27500 0.03926
 H11 0.84900 0.83100 0.16400 0.03293
 H12 0.84700 0.03300 0.16400 0.02533

MgSO₄·7H₂O

data_global
_chemical_name 'Epsomite'
_chemical_formula_sum 'Mg S O11 H14'
_cell_length_a 11.868
_cell_length_b 11.996
_cell_length_c 6.857
_cell_angle_alpha 90
_cell_angle_beta 90
_cell_angle_gamma 90
_cell_volume 976.221
_symmetry_space_group_name_H-M 'P 21 21 21'
loop_
_atom_site_label
_atom_site_fract_x
_atom_site_fract_y
_atom_site_fract_z
Mg 0.42290 0.10630 0.04030
S 0.72660 0.18390 0.49050
O1 0.68530 0.07500 0.42790
O2 0.85060 0.18680 0.48210
O3 0.68840 0.20630 0.69040
O4 0.68080 0.27160 0.36050
O11 0.26550 0.17460 0.00380
O12 0.47160 0.24780 0.19920
O13 0.46910 0.17580 0.77960
O14 0.58280 0.04630 0.07730
O15 0.37610 0.96200 0.88890
O16 0.36220 0.03420 0.29070
O17 0.49160 0.43770 0.93840
H1 0.24400 0.22900 0.10500
H2 0.23400 0.20600 0.88800
H3 0.43500 0.27000 0.33000
H4 0.53300 0.24600 0.26800
H5 0.41900 0.23400 0.66400
H6 0.54900 0.18800 0.75500
H7 0.63200 0.05500 0.21200
H8 0.60000 0.98300 0.02500
H9 0.35600 0.90600 0.96100
H10 0.42800 0.94600 0.76800
H11 0.28100 0.03300 0.32000
H12 0.38500 0.00800 0.41400
H13 0.43100 0.49200 0.97500
H14 0.46500 0.37000 0.00800

Mg(NH₄)₂(SO₄)₂·6H₂O

```

data_global
_chemical_name 'Boussingaultite'
_chemical_formula_sum 'Mg S2 O14 N2 H20'
_cell_length_a 9.324
_cell_length_b 12.597
_cell_length_c 6.211
_cell_angle_alpha 90
_cell_angle_beta 107.14
_cell_angle_gamma 90
_cell_volume 697.110
_symmetry_space_group_name_H-M 'P 1 21/a 1'
loop_
_atom_site_label
_atom_site_fract_x
_atom_site_fract_y
_atom_site_fract_z
_atom_site_Uiso_or_equiv
Mg 0.00000 0.00000 0.00000 ?
S 0.09530 -0.36050 0.25750 ?
O1 -0.04690 -0.41740 0.21160 ?
O2 0.21850 -0.43280 0.37180 ?
O3 0.11850 -0.32110 0.04560 ?
O4 0.09510 -0.27020 0.40890 ?
O5 0.16030 -0.10940 -0.03070 ?
O6 0.16850 0.10420 0.16560 ?
O7 -0.00170 -0.06870 0.29860 ?
N 0.13210 0.35090 0.36110 ?
H1 0.21000 0.10000 0.30000 0.05066
H2 0.02000 -0.13100 0.32000 0.05066
H3 0.26000 -0.09000 0.05000 0.05066
H4 0.06000 0.33300 0.21000 0.05066
H5 0.15000 -0.17800 -0.01000 0.05066
H6 0.21000 0.30500 0.40000 0.05066
H7 0.17000 0.42200 0.36000 0.05066
H8 0.40000 -0.43800 0.31000 0.05066
H9 0.23000 0.12000 0.10000 0.05066
H10 0.09000 0.34600 0.45000 0.05066

```

MgCl₂·6H₂O

```

data_global
_chemical_name 'Bischofite'
_chemical_formula_sum 'Mg Cl2 O6 H12'
_cell_length_a 9.8607
_cell_length_b 7.1071
_cell_length_c 6.0737

```

```

_cell_angle_alpha 90
_cell_angle_beta 93.758
_cell_angle_gamma 90
_cell_volume 424.736
_symmetry_space_group_name_H-M 'C 1 2/m 1'
loop_
_atom_site_label
_atom_site_fract_x
_atom_site_fract_y
_atom_site_fract_z
_atom_site_Uiso_or_equiv
Mg 0.00000 0.00000 0.00000 0.02533
Cl 0.31760 0.00000 0.61220 0.03546
O1 0.20190 0.00000 0.10950 0.04433
O2 -0.04290 0.20670 0.22330 0.04939
H1 0.23720 0.00000 0.25830 0.06333
H2 0.26930 0.00000 0.00830 0.08866
H3 0.02090 0.29970 0.27840 0.05699
H4 -0.11610 0.19840 0.31510 0.07472

```

Mg₃(PO₄)₂·8H₂O

```

data_global
_chemical_name 'Baricite'
_chemical_formula_sum 'Mg3 P2 O16'
_cell_length_a 10.034
_cell_length_b 13.407
_cell_length_c 4.657
_cell_angle_alpha 90
_cell_angle_beta 105.09
_cell_angle_gamma 90
_cell_volume 604.884
_symmetry_space_group_name_H-M 'C 1 2/m 1'
loop_
_atom_site_label
_atom_site_fract_x
_atom_site_fract_y
_atom_site_fract_z
Mg1 0.00000 0.00000 0.00000
Mg2 0.00000 0.39054 0.00000
P 0.31452 0.00000 0.38430
O1 0.15750 0.00000 0.37090
O2 0.39470 0.00000 0.71440
O3 0.34550 0.09560 0.23030
OW1 0.40130 0.38660 0.19160
OW2 0.10100 0.27870 0.28020
H1W -0.18164 -0.09776 0.03363

```

H1Y -0.10724 -0.08279 0.37874
 H2W 0.51774 -0.26277 1.22796
 H2Y 0.60463 -0.18519 1.46504

MgHPO₄·3H₂O

data_global
 _chemical_name 'Newberyite'
 _chemical_formula_sum 'P Mg O7 H7'
 _cell_length_a 10.203
 _cell_length_b 10.678
 _cell_length_c 10.015
 _cell_angle_alpha 90
 _cell_angle_beta 90
 _cell_angle_gamma 90
 _cell_volume 1091.111
 _symmetry_space_group_name_H-M 'P b c a'
 loop_
 _atom_site_label
 _atom_site_fract_x
 _atom_site_fract_y
 _atom_site_fract_z
 P -0.00910 0.13280 0.15360
 Mg 0.29720 0.24680 0.08620
 O1 -0.08810 0.19950 0.25750
 O2 -0.05170 0.16150 0.01000
 O3 0.13860 0.15330 0.16780
 O4 -0.03370 -0.01290 0.17810
 Ow1 0.16700 0.31310 -0.06160
 Ow2 0.24950 0.41310 0.18950
 Ow3 0.35400 0.09260 -0.03270
 H1 0.17790 0.31930 -0.15730
 H2 0.07990 0.27880 -0.04970
 H3 0.29130 0.49350 0.17660
 H4 0.16630 0.43060 0.23100
 H5 0.35220 0.10690 -0.12520
 H6 0.34610 0.00420 -0.02030
 H7 -0.00260 -0.07000 0.10520

Mg(NO₃)₂·6H₂O

data_global
 _chemical_name 'Lansfordite'
 _chemical_formula_sum 'Mg C O8 H10'
 _cell_length_a 6.190
 _cell_length_b 12.614
 _cell_length_c 6.56
 _cell_angle_alpha 90

```

_cell_angle_beta 93.72
_cell_angle_gamma 90
_cell_volume 512.3
_symmetry_space_group_name_H-M 'P 1 21/c 1'
loop_
_atom_site_label
_atom_site_fract_x
_atom_site_fract_y
_atom_site_fract_z
Mg 0.00000 0.00000 0.00000
O1 -.036 0.1614 -.0313
O2 0.3007 0.0249 0.1445
O3 0.1448 -.0028 -.2773
H11 0.068 0.2106 0.008
H12 -.178 0.1927 -.02
H21 0.364 -.0145 0.260
H22 0.396 0.0781 0.114
H31 0.192 0.0613 -.340
H32 0.195 -.0588 -.349
N 0.469 0.2976 0.0435
O4 0.536 0.2042 0.0149
O5 0.278 0.309 0.08
O6 0.597 0.374 0.0346

```

Forsterite, Mg₂SiO₄

```

data_forsterite
_symmetry_space_group_name_H-M 'PBNM'
_symmetry_Int_Tables_number 62
_symmetry_cell_setting orthorhombic
_cell_length_a 4.7690
_cell_length_b 10.2430
_cell_length_c 6.0030
_cell_angle_alpha 90.0000
_cell_angle_beta 90.0000
_cell_angle_gamma 90.0000
loop_
_atom_site_label
_atom_site_type_symbol
_atom_site_fract_x
_atom_site_fract_y
_atom_site_fract_z
_atom_site_U_iso_or_equiv
_atom_site_adp_type
_atom_site_occupancy
O3 O 0.27820 0.16370 0.03420 0.00000 Uiso 1.00
Mg1 Mg 0.00000 0.00000 0.00000 0.00000 Uiso 1.00

```

O2 O 0.76650 0.09160 0.25000 0.00000 Uiso 1.00
 O4 O 0.21910 0.44780 0.25000 0.00000 Uiso 1.00
 Mg2 Mg -0.00990 0.27750 0.25000 0.00000 Uiso 1.00
 Si6 Si 0.42700 0.09440 0.25000 0.00000 Uiso 1.00

MgMoO₄

_chemical_name_systematic 'Magnesium molybdate'
 _chemical_formula_structural 'Mg (Mo O4)'
 _cell_length_a 10.273(3)
 _cell_length_b 9.288(3)
 _cell_length_c 7.025(2)
 _cell_angle_alpha 90.
 _cell_angle_beta 106.96
 _cell_angle_gamma 90.
 _cell_volume 641.1404
 _cell_formula_units_Z 8
 _symmetry_space_group_name_H-M 'C 1 2/m 1'
 _symmetry_Int_Tables_number 12
 _refine_ls_R_factor_all 0.0532
 loop_
 _atom_site_label
 _atom_site_type_symbol
 _atom_site_symmetry_multiplicity
 _atom_site_Wyckoff_symbol
 _atom_site_fract_x
 _atom_site_fract_y
 _atom_site_fract_z
 _atom_site_B_iso_or_equiv
 _atom_site_occupancy
 Mo1 Mo6+ 4 h 0.5 0.251 0.5 0.27 1.
 Mo2 Mo6+ 4 i 0.7291 0.5 0.0957 0.42 1.
 Mg1 Mg2+ 4 g 0.5 0.1784(1) 0 0.36 1.
 Mg2 Mg2+ 4 i 0.7996(1) 0.5 0.6431(2) 0.3 1.
 O1 O2- 8 j 0.5415(2) 0.1533(2) 0.3040(3) 0.48 1.
 O2 O2- 8 j 0.3587(2) 0.3561(3) 0.3912(4) 1.08 1.
 O3 O2- 4 i 0.8587(2) 0.5 -.0391 0.51 1.
 O4 O2- 8 j 0.6337(3) 0.3448(3) 0.0283(4) 1.23 1.
 O5 O2- 4 i 0.2983(4) 0 0.3551(5) 1.47 1.

MgWO₄

data_global
 _chemical_name 'Ferberite'
 _chemical_formula_sum 'Mg W O4'
 _cell_length_a 4.696
 _cell_length_b 5.683
 _cell_length_c 4.945

```

_cell_angle_alpha 90
_cell_angle_beta 90.83
_cell_angle_gamma 90
_cell_volume 132.0
_symmetry_space_group_name_H-M 'P 1 2/c 1'
loop_
_atom_site_label
_atom_site_fract_x
_atom_site_fract_y
_atom_site_fract_z
W 0.00000 0.18190 0.25000
Mg 0.50000 0.6742 0.25000
O1 0.2160 0.1070 0.9370
O2 0.2560 0.37660 0.397000

```

α -Mg₂V₂O₇

```

data_global
_chemical_name 'Mg2V2O7'
_chemical_formula_sum 'Mg2 V2 O7'
_cell_length_a 6.599
_cell_length_b 8.406
_cell_length_c 9.472
_cell_angle_alpha 90
_cell_angle_beta 100.6085
_cell_angle_gamma 90
_cell_volume 516.443
_symmetry_space_group_name_H-M 'P 1 21/c 1'
loop_
_atom_site_label
_atom_site_fract_x
_atom_site_fract_y
_atom_site_fract_z
_atom_site_Uiso_or_equiv
Mg1 0.14810 0.12140 0.46350 0.01600
Mg2 0.31210 0.38950 0.68210 0.01600
V1 0.35910 0.75870 0.53100 0.01280
V2 0.19190 0.01990 0.81510 0.01150
O1 0.61080 0.12820 0.12240 0.01000
O2 0.43100 0.13070 0.40100 0.01000
O3 0.17130 0.36980 0.45920 0.01200
O4 0.25070 0.35800 0.18810 0.01200
O5 0.67730 0.37280 0.35100 0.01900
O6 0.02540 0.07690 0.24540 0.01400
O7 0.85030 0.37830 0.00280 0.01000

```

Mg(VO₃)₂

data_3D

_symmetry_space_group_name_H-M 'C2/M'

_symmetry_Int_Tables_number 12

_symmetry_cell_setting monoclinic

_cell_length_a 9.2790

_cell_length_b 3.5020

_cell_length_c 6.7310

_cell_angle_alpha 90.0000

_cell_angle_beta 111.7700

_cell_angle_gamma 90.0000

loop_

_atom_site_label

_atom_site_type_symbol

_atom_site_fract_x

_atom_site_fract_y

_atom_site_fract_z

_atom_site_U_iso_or_equiv

_atom_site_adp_type

_atom_site_occupancy

Mg1 Mg 0.00000 0.00000 0.00000 0.00000 Uiso 1.00

V1 V 0.30514 0.50000 0.34360 0.00000 Uiso 1.00

O1 O 0.15170 0.50000 0.11330 0.00000 Uiso 1.00

O2 O 0.46070 0.50000 0.27640 0.00000 Uiso 1.00

O3 O 0.19300 0.50000 0.56520 0.00000 Uiso 1.00

Mg₃(VO₄)₂

data_global

_chemical_name 'Mg₃(VO₄)₂'_chemical_formula_sum 'Mg₃ V₂ O₈'

_cell_length_a 6.053

_cell_length_b 11.442

_cell_length_c 8.33

_cell_angle_alpha 90

_cell_angle_beta 90

_cell_angle_gamma 90

_cell_volume 546.466

_symmetry_space_group_name_H-M 'C m c a'

loop_

_atom_site_label

_atom_site_fract_x

_atom_site_fract_y

_atom_site_fract_z

_atom_site_U_iso_or_equiv

Mg1 0.00000 0.00000 0.00000 0.00650

Mg2 0.25000 0.13350 0.25000 0.00630

V 0.00000 0.37978 0.12098 0.00470
 O1 0.00000 0.251360 0.22740 0.00800
 O2 0.00000 0.003750 0.24420 0.00700
 O3 0.27230 0.117910 0.99740 0.00700

Geikielite, MgTiO₃

data_global
 _chemical_name 'Geikielite'
 _chemical_formula_sum 'Mg Ti O3'
 _cell_length_a 5.05478
 _cell_length_b 5.05478
 _cell_length_c 13.8992
 _cell_angle_alpha 90
 _cell_angle_beta 90
 _cell_angle_gamma 120
 _cell_volume 307.557
 _symmetry_space_group_name_H-M 'R -3'
 loop_
 _atom_site_label
 _atom_site_fract_x
 _atom_site_fract_y
 _atom_site_fract_z
 Mg 0.00000 0.00000 0.35570
 Ti 0.00000 0.00000 0.14510
 O 0.31591 0.02146 0.24635

Magnesite, MgCO₃

data_global
 _chemical_name 'Magnesite'
 _chemical_formula_sum 'Mg C O3'
 _cell_length_a 4.6339
 _cell_length_b 4.6339
 _cell_length_c 15.0177
 _cell_angle_alpha 90
 _cell_angle_beta 90
 _cell_angle_gamma 120
 _cell_volume 279.272
 _symmetry_space_group_name_H-M 'R -3 c'
 loop_
 _atom_site_label
 _atom_site_fract_x
 _atom_site_fract_y
 _atom_site_fract_z
 _atom_site_Uiso_or_equiv
 Mg 0.00000 0.00000 0.00000 0.00507
 C 0.00000 0.00000 0.25000 0.00456

O 0.27800 0.00000 0.25000 0.00507

Spinel, MgAl₂O₄

data_global
 _chemical_name 'Spinel'
 _chemical_formula_sum '(Mg Al2) O4'
 _cell_length_a 8.08435
 _cell_length_b 8.08435
 _cell_length_c 8.08435
 _cell_angle_alpha 90
 _cell_angle_beta 90
 _cell_angle_gamma 90
 _cell_volume 528.367
 _symmetry_space_group_name_H-M 'F d 3 m'
 loop_
 _atom_site_label
 _atom_site_fract_x
 _atom_site_fract_y
 _atom_site_fract_z
 _atom_site_occupancy
 _atom_site_Uiso_or_equiv
 Mg 0.12500 0.12500 0.12500 1.0 0.00304
 Al 0.50000 0.50000 0.50000 1.000 0.00887
 O 0.26148 0.26148 0.26148 1.00000 0.00671

Åkermanite, Ca₂MgSi₂O₇

data_global
 _chemical_name 'Akermanite'
 _chemical_formula_sum 'Mg Ca2 Si2 O7'
 _cell_length_a 7.8348
 _cell_length_b 7.8348
 _cell_length_c 5.0087
 _cell_angle_alpha 90
 _cell_angle_beta 90
 _cell_angle_gamma 90
 _cell_volume 307.454
 _symmetry_space_group_name_H-M 'P -4 21 m'
 loop_
 _atom_site_label
 _atom_site_fract_x
 _atom_site_fract_y
 _atom_site_fract_z
 _atom_site_Uiso_or_equiv
 Mg 0.00000 0.00000 0.00000 0.00887
 Ca 0.33180 0.16820 0.50660 0.01748
 Si 0.13970 0.36030 0.93500 0.00773

O1 0.00000 0.50000 0.82000 0.02660
 O2 0.14020 0.35980 0.25510 0.01938
 O3 0.08250 0.18700 0.78830 0.02406

α -MgSO₄

data_global
 _chemical_formula_sum 'Mg SO4'
 _cell_length_a 5.174713
 _cell_length_b 7.875632
 _cell_length_c 6.495166
 _cell_angle_alpha 90
 _cell_angle_beta 90
 _cell_angle_gamma 90
 _cell_volume 264.705
 _symmetry_space_group_name_H-M 'Cmcm'
 loop_
 _atom_site_label
 _atom_site_fract_x
 _atom_site_fract_y
 _atom_site_fract_z
 Mg 0.0 0.0 0.0
 S 0 0.3508 0.25
 O1 0 0.24939 0.06357
 O2 0.23321 0.46184 0.25

Mg(HCOO)₂·2H₂O

data_Mg(HCOO)2x2H2O
 _symmetry_space_group_name_H-M 'P21/C'
 _symmetry_Int_Tables_number 14
 _symmetry_cell_setting monoclinic
 _cell_length_a 8.6400
 _cell_length_b 7.1490
 _cell_length_c 9.3820
 _cell_angle_alpha 90.0000
 _cell_angle_beta 98.0500
 _cell_angle_gamma 90.0000
 loop_
 _atom_site_label
 _atom_site_type_symbol
 _atom_site_fract_x
 _atom_site_fract_y
 _atom_site_fract_z
 _atom_site_U_iso_or_equiv
 _atom_site_adp_type
 _atom_site_occupancy
 C1 C 0.03160 0.22730 0.27140 0.00000 Uiso 1.00

C2	C	0.32680	0.61370	0.43630	0.00000	Uiso	1.00
O1	O	0.09430	0.11090	0.19730	0.00000	Uiso	1.00
O2	O	0.08440	0.27370	0.39850	0.00000	Uiso	1.00
O3	O	0.43690	0.72580	0.42410	0.00000	Uiso	1.00
O4	O	0.21000	0.64940	0.49920	0.00000	Uiso	1.00
O5	O	0.27940	0.47830	0.06460	0.00000	Uiso	1.00
O6	O	0.41370	0.10740	0.30210	0.00000	Uiso	1.00
H1	H	0.22830	0.41090	0.02250	0.00000	Uiso	1.00
H2	H	0.23400	0.59300	0.04860	0.00000	Uiso	1.00
H3	H	0.33130	0.48890	0.38980	0.00000	Uiso	1.00
H4	H	0.92520	0.29320	0.22610	0.00000	Uiso	1.00
H5	H	0.46560	0.15120	0.22970	0.00000	Uiso	1.00
H6	H	0.32520	0.09330	0.27210	0.00000	Uiso	1.00
Mg1	Mg	0.00000	0.00000	0.00000	0.00000	Uiso	1.00
Mg2	Mg	0.50000	0.50000	0.00000	0.00000	Uiso	1.00

Mg(AcAc)₂·2H₂O

data_global

_chemical_name 'diaquobis(acetylacetonato)magnesium(II)'

_chemical_formula_sum 'Mg2 (CH3COCH2COCH3)2 2H2O'

_cell_length_a 10.9836

_cell_length_b 5.3537

_cell_length_c 11.1761

_cell_angle_alpha 90

_cell_angle_beta 106.356

_cell_angle_gamma 90

_cell_volume 657.2

_symmetry_space_group_name_H-M 'P 1 21/c 1'

loop_

_atom_site_label

_atom_site_fract_x

_atom_site_fract_y

_atom_site_fract_z

Mg	0.0	0.0	0.0
O1	0.1417	0.2196	0.0957
O2	0.1170	-0.1591	-0.0898
O3	0.0541	-0.2869	0.1392
C1	0.3576	0.3371	0.2004
C2	0.2636	0.1738	0.1105
C3	0.3093	-0.0156	0.0478
C4	0.2368	-0.1678	-0.0463
C5	0.3026	-0.3648	-0.1032
H1	0.35	-0.03	0.67
H2	0.33	0.12	0.78
H3	0.44	0.2	0.72
H4	0.715	0.12	0.695

H5	0.750	-0.03	0.59
H6	0.61	0.140	0.575
H7	0.41	-0.02	0.080
H8	0.93	0.48	0.86
H9	0.94	0.24	0.78

Mg(OAc)₂·4H₂O

```

data_global
_chemical_name 'Magnesium acetate tetrahydrate'
_chemical_formula_sum 'Mg2 C4 O8 H14'
_cell_length_a 4.807
_cell_length_b 11.973
_cell_length_c 8.554
_cell_angle_alpha 90
_cell_angle_beta 95.36
_cell_angle_gamma 90
_cell_volume 490.2
_symmetry_space_group_name_H-M 'P 1 21/c 1'
loop_
_atom_site_label
_atom_site_fract_x
_atom_site_fract_y
_atom_site_fract_z
Mg 0.500 0.5000 0.0
O1 0.2312 0.4155 1.1413
O2 0.7494 0.5448 1.1983
O3 0.7293 0.3545 0.9833
O4 0.5676 0.75252 1.1625
C1 0.3561 0.7399 1.0675
C2 0.2010 0.8406 1.0035
H21 0.3300 0.3790 1.2080
H22 0.0800 0.3870 1.1010
H23 0.0700 0.4650 -0.2130
H31 0.2500 0.1200 0.3040
H32 -0.0100 0.8230 0.9950
H41 0.2300 0.9110 1.0670
H42 0.2800 0.8750 0.9490

```

MgS

```

data_MgS
_symmetry_space_group_name_H-M 'FM-3M'
_symmetry_Int_Tables_number 225
_symmetry_cell_setting cubic
_cell_length_a 5.2033
_cell_length_b 5.2033
_cell_length_c 5.2033

```

```

_cell_angle_alpha      90.0000
_cell_angle_beta      90.0000
_cell_angle_gamma     90.0000
loop_
_atom_site_label
_atom_site_type_symbol
_atom_site_fract_x
_atom_site_fract_y
_atom_site_fract_z
_atom_site_U_iso_or_equiv
_atom_site_adp_type
_atom_site_occupancy
MG  Mg  0.00000  0.00000  0.00000  0.00000  Uiso  1.00
S   S   0.50000  0.50000  0.50000  0.00000  Uiso  1.00

```

MgH₂

```

data_global
_chemical_formula_sum 'Mg H2'
_cell_length_a 4.5168
_cell_length_b 4.5168
_cell_length_c 3.0205
_cell_angle_alpha 90
_cell_angle_beta 90
_cell_angle_gamma 90
_cell_volume 61.07
_symmetry_space_group_name_H-M 'P42/mnm'
loop_
_atom_site_label
_atom_site_fract_x
_atom_site_fract_y
_atom_site_fract_z
Mg1  0.00000  0.00000  0.00000
H1  0.303  0.303  0.000

```

MgCl₂

```

data_global
_chemical_name 'Magnesium dichloride'
_cell_length_a 3.632
_cell_length_b 3.632
_cell_length_c 17.795
_cell_angle_alpha 90
_cell_angle_beta 90
_cell_angle_gamma 120
_cell_volume 201.1
_symmetry_space_group_name_H-M 'R -3 m'
loop_

```

```

_atom_site_label
_atom_site_fract_x
_atom_site_fract_y
_atom_site_fract_z
Mg 0.0 0.0 0.0
Cl 0.3333 0.66667 0.25510

```

Mg₃N₂

```

data_Mg3N2
_symmetry_space_group_name_H-M 'IA-3'
_symmetry_Int_Tables_number 206
_symmetry_cell_setting cubic
_cell_length_a 9.9528
_cell_length_b 9.9528
_cell_length_c 9.9528
_cell_angle_alpha 90.0000
_cell_angle_beta 90.0000
_cell_angle_gamma 90.0000
loop_
_atom_site_label
_atom_site_type_symbol
_atom_site_fract_x
_atom_site_fract_y
_atom_site_fract_z
_atom_site_U_iso_or_equiv
_atom_site_adp_type
_atom_site_occupancy
Mg1 Mg 0.38900 0.15200 0.38230 0.00000 Uiso 1.00
N1 N 0.25000 0.25000 0.25000 0.00000 Uiso 1.00
N2 N 0.96951 0.00000 0.25000 0.00000 Uiso 1.00

```

Mg₂Si

```

data_global
_chemical_name 'Magnesium Silicide'
_chemical_formula_sum 'Si Mg2'
_cell_length_a 6.3524
_cell_length_b 6.3524
_cell_length_c 6.3524
_cell_angle_alpha 90
_cell_angle_beta 90
_cell_angle_gamma 90
_cell_volume 256.33
_symmetry_space_group_name_H-M 'F m 3 m'
loop_
_atom_site_label
_atom_site_fract_x

```

```

_atom_site_fract_y
_atom_site_fract_z
Si 0.00000 0.00000 0.00000
Mg 0.25000 0.25000 0.25000

```

MgCP₂

```

data_global
_chemical_name 'Bischofite'
_chemical_formula_sum 'Mg C10H10'
_symmetry_space_group_name_H-M 'P21/C'
_symmetry_Int_Tables_number 14
_symmetry_cell_setting monoclinic
_cell_length_a 5.9680
_cell_length_b 8.0730
_cell_length_c 10.9230
_cell_angle_alpha 90.0000
_cell_angle_beta 121.3700
_cell_angle_gamma 90.0000
loop_
_atom_site_label
_atom_site_type_symbol
_atom_site_fract_x
_atom_site_fract_y
_atom_site_fract_z
_atom_site_U_iso_or_equiv
_atom_site_adp_type
_atom_site_occupancy
C1 C 0.02700 0.22600 0.45600 0.00000 Uiso 1.00
C2 C 0.21300 0.30700 0.44100 0.00000 Uiso 1.00
C3 C 0.07500 0.40800 0.32500 0.00000 Uiso 1.00
C4 C -0.18500 0.39400 0.26900 0.00000 Uiso 1.00
C5 C -0.22600 0.27800 0.35100 0.00000 Uiso 1.00
H1 H 0.10300 0.17600 0.53100 0.00000 Uiso 1.00
H2 H 0.43900 0.28500 0.52000 0.00000 Uiso 1.00
H3 H 0.16700 0.46200 0.30300 0.00000 Uiso 1.00
H4 H -0.37400 0.43500 0.16700 0.00000 Uiso 1.00
H5 H -0.42000 0.24200 0.31400 0.00000 Uiso 1.00
Mg1 Mg 0.00000 0.00000 0.00000 0.00000 Uiso 1.00

```

Mg-phthalocyanine

```

data_mgpc260
_chemical_name_common 'Magnesium Phthalocyanine'
_chemical_formula_moiety 'C32H16N8Mg'
_chemical_formula_sum 'C32 H16 Mg N8'
_chemical_formula_weight 536.84
_symmetry_cell_setting 'monoclinic'

```

```

_symmetry_space_group_name_H-M 'P 21/c'
_cell_length_a      14.417(3)
_cell_length_b      4.9130(10)
_cell_length_c      19.002(4)
_cell_angle_alpha   90.00
_cell_angle_beta    119.85(3)
_cell_angle_gamma   90.00
_cell_volume        1167.4(4)
_cell_formula_units_Z  2
loop_
_atom_site_label
_atom_site_type_symbol
_atom_site_fract_x
_atom_site_fract_y
_atom_site_fract_z
_atom_site_U_iso_or_equiv
_atom_site_adp_type
_atom_site_occupancy
_atom_site_symmetry_multiplicity
_atom_site_calc_flag
_atom_site_refinement_flags
_atom_site_disorder_assembly
_atom_site_disorder_group
Mg Mg -0.0(2) -0.0(4) 0.00(15) 0.0479(6) Uani 1 1 d P . .
N1 N 0.25331(11) 0.0238(3) 0.16218(8) 0.0305(4) Uani 1 1 d . . .
N2 N 0.07557(12) 0.2217(3) 0.09935(9) 0.0347(4) Uani 1 1 d . . .
N3 N -0.06941(12) 0.5272(3) 0.07652(9) 0.0344(4) Uani 1 1 d . . .
N4 N -0.13378(11) 0.2058(3) -0.03526(9) 0.0341(4) Uani 1 1 d . . .
C1 C 0.18033(15) 0.1953(4) 0.16025(11) 0.0314(5) Uani 1 1 d . . .
C2 C 0.20230(14) 0.3938(4) 0.22375(11) 0.0293(4) Uani 1 1 d . . .
C3 C 0.29198(15) 0.4473(4) 0.29842(11) 0.0375(5) Uani 1 1 d . . .
H3 H 0.3550 0.3500 0.3158 0.045 Uiso 1 1 calc R . .
C4 C 0.28485(16) 0.6485(4) 0.34601(11) 0.0403(5) Uani 1 1 d . . .
H4 H 0.3439 0.6879 0.3963 0.048 Uiso 1 1 calc R . .
C5 C 0.19076(16) 0.7926(4) 0.31977(11) 0.0413(5) Uani 1 1 d . . .
H5 H 0.1883 0.9278 0.3530 0.050 Uiso 1 1 calc R . .
C6 C 0.10040(15) 0.7424(4) 0.24578(11) 0.0366(5) Uani 1 1 d . . .
H6 H 0.0375 0.8397 0.2290 0.044 Uiso 1 1 calc R . .
C7 C 0.10757(14) 0.5414(4) 0.19781(11) 0.0305(5) Uani 1 1 d . . .
C8 C 0.03008(15) 0.4311(4) 0.11967(11) 0.0323(5) Uani 1 1 d . . .
C9 C -0.14515(14) 0.4156(4) 0.00694(11) 0.0309(5) Uani 1 1 d . . .
C10 C -0.25585(14) 0.5070(4) -0.03407(11) 0.0301(4) Uani 1 1 d . . .
C11 C -0.30929(15) 0.7032(4) -0.01601(12) 0.0363(5) Uani 1 1 d . . .
H11 H -0.2731 0.8117 0.0299 0.044 Uiso 1 1 calc R . .
C12 C -0.41753(15) 0.7345(4) -0.06767(12) 0.0422(5) Uani 1 1 d . . .
H12 H -0.4549 0.8649 -0.0563 0.051 Uiso 1 1 calc R . .

```

C13 C -0.47160(16) 0.5733(4) -0.13667(13) 0.0467(6) Uani 1 1 d . . .
 H13 H -0.5447 0.5977 -0.1707 0.056 Uiso 1 1 calc R . .
 C14 C -0.41836(15) 0.3773(4) -0.15544(12) 0.0404(5) Uani 1 1 d . . .
 H14 H -0.4548 0.2709 -0.2018 0.048 Uiso 1 1 calc R . .
 C15 C -0.31006(15) 0.3433(4) -0.10375(11) 0.0315(5) Uani 1 1 d . . .
 C16 C -0.23077(14) 0.1581(4) -0.10329(11) 0.0301(4) Uani 1 1 d . . .

Li₂SO₄ [1]

data_LiSO4_Wyckoff
 _symmetry_space_group_name_H-M 'P21/A'
 _symmetry_Int_Tables_number 14
 _symmetry_cell_setting monoclinic
 _cell_length_a 8.2500
 _cell_length_b 4.9500
 _cell_length_c 8.4400
 _cell_angle_alpha 90.0000
 _cell_angle_beta 107.9
 _cell_angle_gamma 90.0000
 loop_
 _atom_site_label
 _atom_site_type_symbol
 _atom_site_fract_x
 _atom_site_fract_y
 _atom_site_fract_z
 _atom_site_U_iso_or_equiv
 _atom_site_adp_type
 _atom_site_occupancy
 S S 0.31900 0.06100 0.25000 0.00000 Uiso 1.00
 O1 O 0.49200 -0.04200 0.25000 0.00000 Uiso 1.00
 O2 O 0.18600 -0.04200 0.09900 0.00000 Uiso 1.00
 O3 O 0.28000 -0.04200 0.40100 0.00000 Uiso 1.00
 O4 O 0.31900 0.36700 0.25000 0.00000 Uiso 1.00
 Li1 Li 0.20500 0.58200 0.37500 0.00000 Uiso 1.00
 Li2 Li 0.45500 0.58200 0.12500 0.00000 Uiso 1.00

Li₂SO₄ [2]

data_global
 _chemical_name 'anhydrous Lithium sulfate'
 _chemical_formula_sum 'Li2 S O4 '
 _cell_length_a 8.239
 _cell_length_b 4.9540
 _cell_length_c 8.474
 _cell_angle_alpha 90
 _cell_angle_beta 107.98
 _cell_angle_gamma 90
 _cell_volume 328.9

_symmetry_space_group_name_H-M 'P 2 1/a'

loop_

_atom_site_label
 _atom_site_fract_x
 _atom_site_fract_y
 _atom_site_fract_z
 Li1 0.1986 0.5693 0.3806
 Li2 0.4356 0.5755 0.1287
 S 0.3110 0.0640 0.2516
 O1 0.4636 -0.0644 0.2299
 O2 0.1636 0.0058 0.1053
 O3 0.2747 -0.0507 0.3981
 O4 0.3389 0.3572 0.2739

Na₂SO₄ [1]

data_Na2SO4

_symmetry_space_group_name_H-M 'FDDD'
 _symmetry_Int_Tables_number 70
 _symmetry_cell_setting orthorhombic
 _cell_length_a 5.8630
 _cell_length_b 12.3040
 _cell_length_c 9.8210
 _cell_angle_alpha 90.0000
 _cell_angle_beta 90.0000
 _cell_angle_gamma 90.0000

loop_

_atom_site_label
 _atom_site_type_symbol
 _atom_site_fract_x
 _atom_site_fract_y
 _atom_site_fract_z
 _atom_site_U_iso_or_equiv
 _atom_site_adp_type
 _atom_site_occupancy
 O O -0.02200 0.05600 0.21400 0.00000 Uiso 1.00
 S S 0.12500 0.12500 0.12500 0.00000 Uiso 1.00
 NA Na 0.12500 0.12500 0.43600 0.00000 Uiso 1.00

Na₂SO₄ [2]

data_global

_chemical_name_mineral 'Thenardite'
 _chemical_formula_sum 'Na2 S O4'
 _cell_length_a 9.829
 _cell_length_b 12.302
 _cell_length_c 5.868

```

_cell_angle_alpha 90
_cell_angle_beta 90
_cell_angle_gamma 90
_cell_volume 709.537
_exptl_crystal_density_diffn 2.659
_symmetry_space_group_name_H-M 'F d d d'
loop_
_atom_site_label
_atom_site_fract_x
_atom_site_fract_y
_atom_site_fract_z
Na 0.44160 0.12500 0.12500
S 0.12500 0.12500 0.12500
O 0.21380 0.05720 0.97930

```

K₂SO₄

```

data_oh0048a
_chemical_formula_sum 'K2 O3 S1'
_chemical_formula_weight 158
_symmetry_cell_setting orthorhombic
_symmetry_space_group_name_H-M 'P m c n'
_symmetry_space_group_name_Hall 'P 2n -2a'
_cell_length_a 5.7704(3)
_cell_length_b 10.0712(9)
_cell_length_c 7.4776(4)
_cell_angle_alpha 90.
_cell_angle_beta 90.
_cell_angle_gamma 90.
_cell_volume 434.56(5)
_cell_formula_units_Z 4
loop_
_atom_site_label
_atom_site_fract_x
_atom_site_fract_y
_atom_site_fract_z
_atom_site_U_iso_or_equiv
K(1) 0.25 0.08935(6) 0.17398(7) 0.01769(10)
K(2) 0.25 0.79550(5) 0.48915(7) 0.01554(9)
S 0.25 0.41985(5) 0.23295(7) 0.00993(9)
O(1) 0.25 0.4162(3) 0.0368(3) 0.0263(5)
O(2) 0.25 0.5585(2) 0.2976(3) 0.0195(4)
O(3) 0.0412(3) 0.3522(2) 0.3017(2) 0.0222(3)

```

Rb₂SO₄ [1]

```

data_global
  _chemical_name_mineral 'Rubidium Sulfate'
  _chemical_formula_sum 'Rb S O4'
  _cell_length_a 7.8128
  _cell_length_b 10.4255
  _cell_length_c 5.9694
  _cell_angle_alpha 90
  _cell_angle_beta 90
  _cell_angle_gamma 90
  _cell_volume 607.363
  _exptl_crystal_density_diffn 3.647
  _symmetry_space_group_name_H-M 'P n a m'
loop_
  _atom_site_label
  _atom_site_fract_x
  _atom_site_fract_y
  _atom_site_fract_z
Rb1 0.6750 0.4097 0.25000
Rb2 -0.01160 0.7030 0.25000
S1 0.2380 0.4191 0.25000
O1 0.0471 0.4137 0.25000
O2 0.2974 0.5532 0.25000
O3 0.3030 0.3540 0.0497

```

Rb₂SO₄ [2]

```

data_pnma
  _chemical_formula_sum 'O4 Rb2 S'
  _chemical_formula_weight 267.00
  _cell_length_a 7.8035(4)
  _cell_length_b 5.9725(3)
  _cell_length_c 10.4101(5)
  _cell_angle_alpha 90.00
  _cell_angle_beta 90.00
  _cell_angle_gamma 90.00
  _cell_volume 485.18(4)
  _cell_formula_units_Z 3
loop_
  _atom_site_label
  _atom_site_type_symbol
  _atom_site_fract_x
  _atom_site_fract_y
  _atom_site_fract_z
  _atom_site_U_iso_or_equiv
  _atom_site_adp_type
  _atom_site_occupancy

```

_atom_site_symmetry_multiplicity
 _atom_site_calc_flag
 _atom_site_refinement_flags
 _atom_site_disorder_assembly
 _atom_site_disorder_group
 Rb1 Rb 0.82444(5) 0.2500 0.59079(3) 0.01569(8) Uani 1 2 d SU . .
 Rb2 Rb 0.51209(4) 0.2500 0.29713(3) 0.01421(7) Uani 1 2 d SU . .
 S3 S 1.26253(10) 0.2500 0.58116(7) 0.00888(14) Uani 1 2 d SU . .
 O1 O 1.2028(4) 0.2500 0.4470(3) 0.0155(4) Uani 1 2 d SU . .
 O2 O 1.1958(3) 0.0478(4) 0.6464(2) 0.0195(3) Uani 1 1 d U . .
 O3 O 0.4507(4) 0.2500 0.5856(3) 0.0205(5) Uani 1 2 d SU . .

Rb₂SO₄ [3]

data_pnma-2
 _chemical_formula_sum 'O12 Rb6 S3'
 _chemical_formula_weight 801.00
 _cell_length_a 7.8133(2)
 _cell_length_b 5.9717(2)
 _cell_length_c 10.4269(3)
 _cell_angle_alpha 90.00
 _cell_angle_beta 90.00
 _cell_angle_gamma 90.00
 _cell_volume 486.51(2)
 _cell_formula_units_Z 1
 loop_
 _atom_site_label
 _atom_site_type_symbol
 _atom_site_fract_x
 _atom_site_fract_y
 _atom_site_fract_z
 _atom_site_U_iso_or_equiv
 _atom_site_adp_type
 _atom_site_occupancy
 _atom_site_symmetry_multiplicity
 _atom_site_calc_flag
 _atom_site_refinement_flags
 _atom_site_disorder_assembly
 _atom_site_disorder_group
 Rb1 Rb -0.17565(3) 0.2500 0.590813(19) 0.01811(6) Uani 1 2 d S . .
 Rb2 Rb 0.51207(2) 0.2500 0.297168(18) 0.01663(6) Uani 1 2 d S . .
 S3 S 0.26261(6) 0.2500 0.58132(4) 0.01135(9) Uani 1 2 d S . .
 O1 O 0.4506(2) 0.2500 0.58555(17) 0.0264(4) Uani 1 2 d S . .
 O2 O 0.2030(2) 0.2500 0.44688(14) 0.0201(3) Uani 1 2 d S . .
 O3 O 0.19634(16) 0.04824(19) 0.64611(11) 0.0222(2) Uani 1 1 d . . .

Cs₂SO₄ [1]

data_Cs2SO4

_symmetry_space_group_name_H-M 'PNMA'

_symmetry_Int_Tables_number 62

_symmetry_cell_setting orthorhombic

_cell_length_a 8.1980

_cell_length_b 6.2180

_cell_length_c 10.8840

_cell_angle_alpha 90.0000

_cell_angle_beta 90.0000

_cell_angle_gamma 90.0000

loop_

_atom_site_label

_atom_site_type_symbol

_atom_site_fract_x

_atom_site_fract_y

_atom_site_fract_z

_atom_site_U_iso_or_equiv

_atom_site_adp_type

_atom_site_occupancy

O1 O 0.31100 0.05300 0.35300 0.00000 Uiso 1.00

Cs2 Cs 0.68900 0.25000 0.41700 0.00000 Uiso 1.00

Cs3 Cs 0.00000 0.25000 -0.30800 0.00000 Uiso 1.00

S4 S 0.25000 0.25000 0.41700 0.00000 Uiso 1.00

O5 O 0.06700 0.25000 0.41700 0.00000 Uiso 1.00

O6 O 0.31100 0.25000 0.54500 0.00000 Uiso 1.00

Cs₂SO₄ [2]

data_pnma

_chemical_formula_sum 'Cs2 O4 S'

_chemical_formula_weight 361.88

_cell_length_a 8.2329(2)

_cell_length_b 6.2538(2)

_cell_length_c 10.9344(3)

_cell_angle_alpha 90.00

_cell_angle_beta 90.00

_cell_angle_gamma 90.00

_cell_volume 562.98(3)

_cell_formula_units_Z 4

loop_

_atom_site_label

_atom_site_type_symbol

_atom_site_fract_x

_atom_site_fract_y

_atom_site_fract_z

_atom_site_U_iso_or_equiv

```

_atom_site_adp_type
_atom_site_occupancy
_atom_site_symmetry_multiplicity
_atom_site_calc_flag
_atom_site_refinement_flags
_atom_site_disorder_assembly
_atom_site_disorder_group
Cs1 Cs 0.822921(16) 0.2500 0.590598(12) 0.02191(4) Uani 1 2 d S . .
Cs2 Cs 0.511159(15) 0.2500 0.298498(12) 0.02099(4) Uani 1 2 d S . .
S3 S 1.25918(6) 0.2500 0.58280(4) 0.01550(8) Uani 1 2 d S . .
O1 O 1.19587(15) 0.05750(19) 0.64486(11) 0.0267(2) Uani 1 1 d . . .
O2 O 1.2028(2) 0.2500 0.45447(14) 0.0244(3) Uani 1 2 d S . .
O3 O 0.4375(2) 0.2500 0.58728(17) 0.0318(4) Uani 1 2 d S . .

```

(NH₄)₂SO₄ [1]

data_NH4SO4_Wycoff

_symmetry_space_group_name_H-M 'PNMA'

_symmetry_Int_Tables_number 62

_symmetry_cell_setting orthorhombic

_cell_length_a 7.7820

_cell_length_b 5.9930

_cell_length_c 10.6360

_cell_angle_alpha 90.0000

_cell_angle_beta 90.0000

_cell_angle_gamma 90.0000

loop_

_atom_site_label

_atom_site_type_symbol

_atom_site_fract_x

_atom_site_fract_y

_atom_site_fract_z

_atom_site_U_iso_or_equiv

_atom_site_adp_type

_atom_site_occupancy

```

S S 0.25000 0.25000 0.41700 0.00000 Uiso 1.00
O1 O 0.05600 0.25000 0.41700 0.00000 Uiso 1.00
O2 O 0.31500 0.25000 0.54900 0.00000 Uiso 1.00
O3 O 0.31500 0.04500 0.35100 0.00000 Uiso 1.00
N1 N 0.68500 0.25000 0.41700 0.00000 Uiso 1.00
N2 N 0.00000 0.25000 -0.31100 0.00000 Uiso 1.00
H1 H 0.04400 0.25000 0.05900 0.00000 Uiso 1.00
H2 H 0.14700 0.25000 0.19300 0.00000 Uiso 1.00
H3 H 0.38000 0.25000 0.72000 0.00000 Uiso 1.00
H4 H 0.13800 0.25000 0.70000 0.00000 Uiso 1.00
H5 H 0.25800 0.11100 0.06300 0.00000 Uiso 1.00
H6 H 0.45700 0.11100 0.86100 0.00000 Uiso 1.00

```

(NH₄)₂SO₄ [2]

```

data_global
_chemical_formula_moiety 'N2 H8 S O4'
_chemical_formula_sum 'N2 H8 S O4'
_chemical_formula_weight 132
_symmetry_cell_setting orthorhombic
_cell_length_a 7.7820
_cell_length_b 10.6360
_cell_length_c 5.9930
_cell_angle_alpha 90.0000
_cell_angle_beta 90.0000
_cell_angle_gamma 90.0000
_cell_volume 496.0
_symmetry_space_group_name_H-M 'P N A M'
loop_
_atom_site_label
_atom_site_type_symbol
_atom_site_fract_x
_atom_site_fract_y
_atom_site_fract_z
_atom_site_U_iso_or_equiv
_atom_site_adp_type
_atom_site_occupancy
S S 0.24400 0.419000 0.2500 0.00000 Uiso 1.00
O1 O 0.06120 0.38870 0.2500 0.00000 Uiso 1.00
O2 O 0.27010 0.55590 0.2500 0.00000 Uiso 1.00
O3 O 0.32390 0.36650 0.04880 0.00000 Uiso 1.00
O4 O 0.32390 0.36650 0.45120 0.00000 Uiso 1.00
N1 N 0.68950 0.40250 0.25000 0.00000 Uiso 1.00
N2 N 0.96770 0.70500 0.25000 0.00000 Uiso 1.00
H1 H 0.81000 0.37200 0.25000 0.00000 Uiso 1.00
H2 H 0.60000 0.34300 0.25000 0.00000 Uiso 1.00
H3 H 0.67600 0.45700 0.12200 0.00000 Uiso 1.00
H4 H 0.67600 0.45700 0.37800 0.00000 Uiso 1.00
H5 H 1.06900 0.64900 0.25000 0.00000 Uiso 1.00
H6 H 0.99100 0.79200 0.25000 0.00000 Uiso 1.00
H7 H 0.89300 0.68200 0.12400 0.00000 Uiso 1.00
H8 H 0.89300 0.68200 0.37600 0.00000 Uiso 1.00

```

(NH₄)₂SO₄ [3]

```

data_pnma-nh4
_chemical_formula_sum 'H4 N O2 S'
_chemical_formula_weight 82.10
_cell_length_a 7.7804(2)
_cell_length_b 5.9876(2)
_cell_length_c 10.6323(3)

```

```

_cell_angle_alpha      90.00
_cell_angle_beta      90.00
_cell_angle_gamma     90.00
_cell_volume          495.32(3)
_cell_formula_units_Z  4
loop_
_atom_site_label
_atom_site_type_symbol
_atom_site_fract_x
_atom_site_fract_y
_atom_site_fract_z
_atom_site_U_iso_or_equiv
_atom_site_adp_type
_atom_site_occupancy
_atom_site_symmetry_multiplicity
_atom_site_calc_flag
_atom_site_refinement_flags
_atom_site_disorder_assembly
_atom_site_disorder_group
S1 S 0.75554(4) 0.2500 0.58075(3) 0.02069(10) Uani 1 2 d S . .
O1 O 0.67633(13) 0.04883(15) 0.63371(9) 0.0452(2) Uani 1 1 d . . .
O2 O 0.93809(17) 0.2500 0.61107(18) 0.0548(4) Uani 1 2 d S . .
O3 O 0.73028(19) 0.2500 0.44399(12) 0.0434(3) Uani 1 2 d S . .
N1 N 0.31028(18) 0.2500 0.59699(13) 0.0282(2) Uani 1 2 d S . .
N2 N 0.03204(19) 0.2500 0.29566(13) 0.0302(3) Uani 1 2 d S . .
H1 H 0.196(4) 0.2500 0.617(3) 0.069(9) Uiso 1 2 d S . .
H2 H -0.002(3) 0.2500 0.219(3) 0.053(7) Uiso 1 2 d S . .
H3 H -0.054(5) 0.2500 0.339(4) 0.086(11) Uiso 1 2 d S . .
H4 H 0.325(4) 0.144(5) 0.551(3) 0.104(9) Uiso 1 1 d . . .
H5 H 0.104(4) 0.149(5) 0.303(3) 0.113(10) Uiso 1 1 d . . .
H6 H 0.385(5) 0.2500 0.646(4) 0.101(13) Uiso 1 2 d S . .

```

 α -MgSO₄

see above

 β -MgSO₄ [1]

```

data_I
_chemical_formula_sum  'Mg O4 S'
_chemical_formula_weight  120.37
_symmetry_cell_setting  orthorhombic
_symmetry_space_group_name_H-M  'P n m a'
_symmetry_space_group_name_Hall  '-P 2ac 2n'
_cell_length_a  8.5787(8)
_cell_length_b  6.6953(6)
_cell_length_c  4.7438(5)
_cell_angle_alpha  90.00

```

```

_cell_angle_beta 90.00
_cell_angle_gamma 90.00
_cell_volume 272.47(5)
_cell_formula_units_Z 4
loop_
  _atom_site_type_symbol
  _atom_site_label
  _atom_site_fract_x
  _atom_site_fract_y
  _atom_site_fract_z
  _atom_site_U_iso_or_equiv
  _atom_site_adp_type
  _atom_site_calc_flag
  _atom_site_refinement_flags
  _atom_site_occupancy
  _atom_site_disorder_assembly
  _atom_site_disorder_group
Mg Mg 0.0000 0.0000 0.0000 0.01046(10) Uani d S 1 . .
S S 0.32046(3) 0.2500 0.02598(5) 0.00547(8) Uani d S 1 . .
O O1 0.37429(7) 0.06895(9) 0.16526(13) 0.01011(12) Uani d . 1 . .
O O2 0.14650(10) 0.2500 0.03881(18) 0.00824(14) Uani d S 1 . .
O O3 0.37517(10) 0.2500 0.73002(17) 0.00961(15) Uani d S 1 . .

```

β -MgSO₄ [2]

```

data_global
_chemical_formula_sum 'Mg SO4'
_cell_length_a 4.74598
_cell_length_b 8.58310
_cell_length_c 6.70933
_cell_angle_alpha 90
_cell_angle_beta 90
_cell_angle_gamma 90
_cell_volume 273.306
_symmetry_space_group_name_H-M 'Pbnm'
loop_
  _atom_site_label
  _atom_site_fract_x
  _atom_site_fract_y
  _atom_site_fract_z
Mg 0.0 0.0 0.0
S 0.478 0.1812 0.25
O1 0.77090 0.12651 0.25
O2 0.46410 0.35189 0.25
O3 0.33748 0.12661 0.06959

```

CaSO₄ [1]

data_CaSO4

_symmetry_space_group_name_H-M 'BBMM'

_symmetry_Int_Tables_number 63

_symmetry_cell_setting orthorhombic

_cell_length_a 6.2380

_cell_length_b 6.9910

_cell_length_c 6.9960

_cell_angle_alpha 90.0000

_cell_angle_beta 90.0000

_cell_angle_gamma 90.0000

loop_

_atom_site_label

_atom_site_type_symbol

_atom_site_fract_x

_atom_site_fract_y

_atom_site_fract_z

_atom_site_U_iso_or_equiv

_atom_site_adp_type

_atom_site_occupancy

Ca1 Ca 0.65400 0.25000 0.00000 0.00000 Uiso 1.00

S2 S 0.15500 0.25000 0.00000 0.00000 Uiso 1.00

O3 O 0.29800 0.08000 0.00000 0.00000 Uiso 1.00

O4 O 0.01500 0.25000 0.17100 0.00000 Uiso 1.00

CaSO₄ [2]

data_global

_chemical_name 'Anhydrite'

_chemical_formula_sum 'Ca S O4'

_cell_length_a 6.993

_cell_length_b 6.995

_cell_length_c 6.245

_cell_angle_alpha 90

_cell_angle_beta 90

_cell_angle_gamma 90

_cell_volume 305.481

_symmetry_space_group_name_H-M 'A m m a'

loop_

_atom_site_label

_atom_site_fract_x

_atom_site_fract_y

_atom_site_fract_z

Ca 0.75000 0.00000 0.34760

S 0.25000 0.00000 0.15556

O1 0.25000 0.16990 0.01620

O2 0.08190 0.00000 0.29750

SrSO₄

```

data_global
_chemical_name_mineral 'Celestine'
_chemical_formula_sum 'Sr S O4'
_cell_length_a 6.8671
_cell_length_b 8.3545
_cell_length_c 5.3458
_cell_angle_alpha 90
_cell_angle_beta 90
_cell_angle_gamma 90
_cell_volume 306.695
_exptl_crystal_density_diffn 3.978
_symmetry_space_group_name_H-M 'P b n m'
loop_
_atom_site_label
_atom_site_fract_x
_atom_site_fract_y
_atom_site_fract_z
Sr 0.15818 0.18395 0.25000
S 0.18505 0.43797 0.75000
O1 0.09230 0.59520 0.75000
O2 0.04180 0.30710 0.75000
O3 0.31070 0.42220 0.97440

```

BaSO₄ [1]

```

data_global
_chemical_name 'Barite'
_chemical_formula_sum 'Ba S O4'
_cell_length_a 8.8701
_cell_length_b 5.4534
_cell_length_c 7.1507
_cell_angle_alpha 90
_cell_angle_beta 90
_cell_angle_gamma 90
_cell_volume 345.9
_symmetry_space_group_name_H-M 'P n m a '
loop_
_atom_site_label
_atom_site_fract_x
_atom_site_fract_y
_atom_site_fract_z
Ba 0.1844 0.25 0.1587
S 0.064 0.25 0.69
O1 -0.092 0.25 0.612
O2 0.187 0.25 0.543
O3 0.079 0.034 0.813

```

BaSO₄ [2]

```

data_global
_chemical_name 'Baryte'
_chemical_formula_sum 'Ba S O4'
_cell_length_a 8.884
_cell_length_b 5.458
_cell_length_c 7.153
_cell_angle_alpha 90
_cell_angle_beta 90
_cell_angle_gamma 90
_cell_volume 346.841
_symmetry_space_group_name_H-M 'P n m a'
loop_
_atom_site_label
_atom_site_fract_x
_atom_site_fract_y
_atom_site_fract_z
_atom_site_Uiso_or_equiv
Ba 0.18460 0.25000 0.15810 0.00861
S 0.43700 0.75000 0.19140 0.00469
O1 0.58780 0.75000 0.10620 0.01976
O2 0.31920 0.75000 0.05150 0.02064
O3 0.41860 0.97020 0.31900 0.01077

```

BaSO₄ [3]

```

data_global
_chemical_name 'Baryte'
_chemical_formula_sum 'Ba S O4'
_cell_length_a 8.8842
_cell_length_b 5.4559
_cell_length_c 7.1569
_cell_angle_alpha 90
_cell_angle_beta 90
_cell_angle_gamma 90
_cell_volume 346.904
_symmetry_space_group_name_H-M 'P n m a'
loop_
_atom_site_label
_atom_site_fract_x
_atom_site_fract_y
_atom_site_fract_z
_atom_site_Uiso_or_equiv
Ba 0.18450 0.25000 0.15850
S 0.43730 0.75000 0.19130
O1 0.58900 0.75000 0.10660
O2 0.31830 0.75000 0.05180
O3 0.42040 0.97000 0.31160

```

```

loop_
  _atom_site_aniso_label
  _atom_site_aniso_U_11
  _atom_site_aniso_U_22
  _atom_site_aniso_U_33
  _atom_site_aniso_U_12
  _atom_site_aniso_U_13
  _atom_site_aniso_U_23
Ba 0.00920 0.01297 0.00986 0.00000 -0.00097 0.00000
S 0.01040 0.01312 0.00856 0.00000 0.00097 0.00000
O1 0.01160 0.02624 0.02880 0.00000 0.00483 0.00000
O2 0.02799 0.02971 0.01401 0.00000 -0.00548 0.00000
O3 0.01400 0.01463 0.01246 0.00368 -0.00097 -0.00218

```

BaSO₄ [4]

```

data_global
  _chemical_name 'Baryte'
  _chemical_formula_sum 'Ba S O4'
  _cell_length_a 7.157
  _cell_length_b 8.884
  _cell_length_c 5.457
  _cell_angle_alpha 90
  _cell_angle_beta 90
  _cell_angle_gamma 90
  _cell_volume 346.971
  _symmetry_space_group_name_H-M 'P b n m'

```

```

loop_
  _atom_site_label
  _atom_site_fract_x
  _atom_site_fract_y
  _atom_site_fract_z
Ba 0.15850 0.18450 0.25000
S 0.19110 0.43750 0.75000
O1 0.10600 0.58780 0.75000
O2 0.04940 0.31770 0.75000
O3 0.31140 0.41990 0.97020

```

BaSO₄ [5]

```

data_global
  _chemical_name 'Baryte'
  _chemical_formula_sum 'Ba S O4'
  _cell_length_a 7.1540
  _cell_length_b 8.8790
  _cell_length_c 5.4540
  _cell_angle_alpha 90
  _cell_angle_beta 90

```

```

_cell_angle_gamma 90
_cell_volume 346.440
_symmetry_space_group_name_H-M 'P b n m'
loop_
_atom_site_label
_atom_site_fract_x
_atom_site_fract_y
_atom_site_fract_z
Ba 0.15842 0.18453 0.25000
S 0.19082 0.43749 0.75000
O1 0.10720 0.58700 0.75000
O2 0.04980 0.31760 0.75000
O3 0.31180 0.41940 0.97040
loop_
_atom_site_aniso_label
_atom_site_aniso_U_11
_atom_site_aniso_U_22
_atom_site_aniso_U_33
_atom_site_aniso_U_12
_atom_site_aniso_U_13
_atom_site_aniso_U_23
Ba 0.01025 0.00843 0.01298 -0.00048 0.00000 0.00000
S 0.00910 0.00840 0.00930 0.00033 0.00000 0.00000
O1 0.02660 0.01310 0.02800 0.01050 0.00000 0.00000
O2 0.01170 0.02090 0.02020 -0.00670 0.00000 0.00000
O3 0.01490 0.01490 0.01030 -0.00200 -0.00280 0.00080

```

ZnSO₄

```

_chemical_name_mineral 'Zinkosite'
_chemical_formula_sum 'Zn S O4'
_cell_length_a 8.604
_cell_length_b 6.746
_cell_length_c 4.774
_cell_angle_alpha 90
_cell_angle_beta 90
_cell_angle_gamma 90
_cell_volume 277.095
_exptl_crystal_density_diffn 3.870
_symmetry_space_group_name_H-M 'P n m a'
loop_
_atom_site_label
_atom_site_fract_x
_atom_site_fract_y
_atom_site_fract_z
_atom_site_U_iso_or_equiv
Zn 0.00000 0.00000 0.00000 0.02450

```

S 0.18029 0.25000 0.46659 0.00920
 O1 0.12790 0.25000 0.76220 0.01470
 O2 0.35450 0.25000 0.45220 0.01260
 O3 0.12670 0.06890 0.32950 0.01440

Al₂(SO₄)₃

_chemical_formula_sum 'Al2 S3 O12'
 _cell_length_a 8.0246
 _cell_length_b 8.0246
 _cell_length_c 21.357
 _cell_angle_alpha 90
 _cell_angle_beta 90
 _cell_angle_gamma 120
 _cell_volume 1191.016
 _symmetry_space_group_name_H-M 'R -3'
 loop_
 _atom_site_label
 _atom_site_fract_x
 _atom_site_fract_y
 _atom_site_fract_z
 Al1 0.00000 0.00000 0.14360
 Al2 0.00000 0.00000 0.35190
 S 0.28900 0.28710 0.25050
 O1 0.18620 0.19920 0.19230
 O2 0.21740 0.14550 0.30170
 O3 0.49400 0.35470 0.24300
 O4 0.26020 0.44990 0.26450

Ga₂(SO₄)₃

_chemical_formula_sum 'Ga2 S3 O12'
 _cell_length_a 8.054
 _cell_length_b 8.054
 _cell_length_c 21.840
 _cell_angle_alpha 90
 _cell_angle_beta 90
 _cell_angle_gamma 120
 _cell_volume 1191.016
 _symmetry_space_group_name_H-M 'R -3'
 loop_
 _atom_site_label
 _atom_site_fract_x
 _atom_site_fract_y
 _atom_site_fract_z
 Ga1 0.00000 0.00000 0.14380
 Ga2 0.00000 0.00000 0.34957
 S 0.04199 0.66508 0.41603
 O1 0.13810 0.675 0.47395

O2 0.1070 0.584 0.36802
O3 0.0847 0.8594 0.40061
O4 0.8355 0.5401 0.42283

In₂(SO₄)₃

_chemical_formula_sum 'In2 S3 O12'
_cell_length_a 8.44
_cell_length_b 8.44
_cell_length_c 23.093
_cell_angle_alpha 90
_cell_angle_beta 90
_cell_angle_gamma 120
_cell_volume 1226.89
_symmetry_space_group_name_H-M 'R -3'
loop_
_atom_site_label
_atom_site_fract_x
_atom_site_fract_y
_atom_site_fract_z
In1 0.00000 0.00000 0.14457
In2 0.00000 0.00000 0.34888
S 0.62483 0.66499 0.41619
O1 0.5465 0.6743 0.4715
O2 0.4828 0.5828 0.3718
O3 0.7105 0.5518 0.42206
O4 0.7634 0.8517 0.4005